Major elemental analysis of asteroid 25143 Itokawa with X-ray fluorescence spectrometer onboard Hayabusa and its relation to meteorite-analogues

Takehiko ARAI

2007

Abstract

In this paper, the results of X-ray fluorescence observation of asteroid 25143 Itokawa with the X-ray fluorescence spectrometer onboard Hayabusa (XRS) are reported, and speculations for relationships between asteroids and meteorites, and origin and evolution of asteroids are discussed.

The Japanese Hayabusa spacecraft successfully carried out in situ observations of S(IV) asteroid 25143 Itokawa. The primary aim of the Hayabusa mission is to reveal relationships between asteroids and meteorites, including a fundamental question whether asteroids are parent body of meteorites or not. The XRS onboard Hayabusa observed X-ray fluorescence emission from uppermost surface materials of Itokawa, excited with solar X-rays, in order to determine the major elemental composition of Itokawa. This observation is the second *in situ* remote X-ray fluorescence spectrometry and the first detailed one with the advanced instruments in space. In this study, major elemental compositions such as Mg, Al, Si, S, Ca, and Fe on the surface materials of Itokawa are estimated, and they are related to the possible meteorite-analogues. Also, the origin and the evolution of Itokawa are discussed.

In this analysis, corrections were carefully carried out for the response function of the XRS as sensor characteristics. Also, temporal fluctuations of incident solar X-rays and variations of surface geometry of Itokawa were corrected. Since the failure of reaction wheels of Hayabusa caused not only decrease of observation duration but also degradation of energy resolution of sensor due to frequent thermal changes of CCDs, many observation data were undergone increasing instrumental noises. Thus, only small amounts of significant data, obtained in appropriate conditions, were analyzed.

The results of analysis indicate that major elemental composition of the surface materials of Itokawa resembles that of chondrite-analogues. In particular, the results indicate that the elemental mass ratios are following: (1) The elemental mass ratio of Fe/Si is larger than that of average composition of ordinary chondrites but the result by correction with mineral mixing effect indicates that the Fe/Si ratio is nearly equal to that of average ratio of ordinary chondrites. (2) The elemental mass ratio of Mg/Si is globally homogeneous in the surface of Itokawa. (3) Elemental mass ratios of Al/Si and S/Si may slightly vary at local areas, and the results by correction with mineral mixing effect indicate elemental mass ratio of S/Si is less than, or same as that of average compositions of ordinary chondrites, in terms of best-fit results. (4) Elemental mass ratios of Al/Si and Ca/Si appear to be larger than those of average compositions of ordinary chondrites.

The results of classification between Itokawa and meteorite-analogues for the elemental mass ratios of Mg/Si, Al/Si, S/Si, Ca/Si and Fe/Si indicate that IAB irons as metallic Fe-rich meteorites are ruled out in the candidates of meteorite-analogues of Itokawa, an S(IV) subtype asteroid of classification by Gaffey *et al.* (1993). This result supports that reason of reddened and darkened features in visible and near infrared reflectance spectrum is space weathering. Also, most probable candidates for Itokawa are ordinary L- or LL-chondrites, EL-chondrites, or primitive achondrites such as Brachinites, Acapulcoites or Winonaites when elemental mass ratios of Mg/Si vs. Fe/Si are compared between those of Itokawa and meteorite-analogues.

This result implies that major elemental composition of Itokawa is similar to that of primitive meteorites.

Regional distribution of the mass ratio of S/Si at the local areas implies that surface alteration might occur on Itokawa. However, the analysis shows that sulfur is not globally depleted and has regional distribution. Resurfacing at the surface of Itokawa due to seismic destruction by impacts and/or tidal destruction by planets encounter might cause such surface heterogeneity. If so only the surface material on Itokawa might be altered but the inner materials remain fresh. Partial melting events in the parent body of Itokawa can not be ruled out. Partial melting of rocks may cause a fraction of enrichment of Al and Ca. In that case, Itokawa may be composed of the portions that were affected by partial melting in the parent body.

The average density of Itokawa is very small that has been estimated by orbits of spacecraft. This result implies that the contracture of Itokawa is a rubble-pile. Addition, the results of elemental analysis by the XRS indicate that mass distribution of major elements on the surface is globally homogeneous. It implies that Itokawa was assembled by compositionally homogeneous rocks. Thus, Itokawa may be a portion of a substantial rubble-pile body.

The result of analysis of Itokawa indicates that elemental composition is most consistent with that of ordinary chondrites. If Itokawa is the parent body of ordinary chondrites, major elemental composition of many primitive bodies in S(IV) subtype asteroid are able to be estimated, which is a large progress in asteroid science and may be in science of the solar system.

Contents

Chapter 1

Backgrounds

In this chapter, a scientific rationale and primary goal of X-ray fluorescence observation for asteroid 25143 Itokawa are described, including the science of the solar system, asteroids and meteorites. The primary goal of this study is to determine the major elemental compositions of Itokawa and to relate it to meteorite-analogues. It is important progress to connect a missing link between asteroids and meteorites.

1.1 Science of small bodies and the solar system

Our solar system scientifically puzzles and interests us about its origin and evolution. In order to understand the science of the solar system, information for the objects of the solar system such as, planets, asteroids, comets, meteorites, interplanetary dusts, and plasmas are required. Fortunately, the physical and chemical profiles of the solar system can be pictured from analysis of meteorites fallen in to the Earth, and remotely obtained from planets and asteroids by ground based observation such as photometry, spectroscopy, and radio astronomy.

Meteorites have a lot of information in the solar system for chemical, mineral, petrologic, and isotopic aspects, and they teach us the conditions and evolution process of the early solar system, with analysis by the latest devices. In particular, primitive meteorites as a chondrite teach us the physical circumstances in the early solar system. Melting features of chondrules in chondrites are found, and they inform us that the giant melting and rapid cooling might have occurred in T-tauri stage in the early solar system due to a heat source called X-wind (*e.g.*, Sonett and Colburn, 1968; Shu *et al.*, 1996). Also heating process has been considered such as intrinsic heat source of ^{26}Al (*e.g.*, Urey, 1955). This information teaches us that heat metamorphism might have occurred in the parent body of meteorites in early time. Furthermore, differentiated meteorites such as achondrites teach us the evolution history of planets, asteroids and so on. Also, brecciated features in stony meteorites teach us the impact history as the evolution of the solar system.

Asteroids also have a lot of information of our solar system as do meteorites. In particular, asteroids teach us not only the composition of materials in the solar system but also these distributions by ground-based observation because their orbit can be calculated precisely.

These evidences inform us the pieces of fundamental question for the origin and evolution of the solar system. To connect piece by piece such the relationship between asteroids and meteorites will reveal the physical circumstances, differentiation of materials, the history of heating, melting, impacting, redox condition, accretion of planetesimal, and so on in the solar system.

1.1.1 Review of asteroids

Asteroids are believed the parent bodies of meteorites. In 1950s, the trajectory of a fire ball, observed by ground based photometry, was calculated. This result implied that most meteorites are coming from an inner part of the asteroid belt between Mars and Jupiter. Therefore, many researchers have believed that meteorites are portions of asteroids.

Figure 1.1 shows the distribution of asteroids in heliocentric distance, observed by ground-based telescopes. Large numbers of asteroids are found in the main belt (over 300 thousands). Most asteroids (98%) exist in the heliocentric distance of 2 to 3.5 AU in the main belt. 3800 asteroids are found in near-Earth orbits and they are called Near-Earth Asteroid (NEA). The NEAs are classified into clans such as Amors (a>1AU, 1.017 < q < 1.3 AU), Apollo (a>1AU, q < 1.017 AU), and Atens (a<1AU, Q > 0.983 AU), where a is a semi major axis, q is a perihelion distance, Q is an aphelion distance.

In ground based visible and near-infrared spectroscopy, the asteroids have been classified by the feature of albedo and spectrum as shown in Figure 1.2. Table 1.1 shows the definition of asteroid taxonomy (Tholen and Barucci, 1989).

Some asteroids have been explored by unmanned spacecrafts. Figure 1.3 shows the images of explored asteroids taken by spacecrafts. The Galileo spacecraft flew by S-class asteroid 951 Gaspra in 1991, and took the multi spectral images of the surface. These images indicated that spectral variations were found in fresh craters at ridges. Craters at ridges tend to be bluer than the nearby surrounding terrain in color. Although the degree of color heterogeneity is much less than 5%, the association of color with craters strengthened the interpretation that these craters excavated relatively fresh subsurface materials (Clark, 1993; Chapman, 1996). S-class asteroid 243 Ida was also observed by the Galileo spacecraft in 1993. Chapman has suggested that the surface materials of Ida are altered by space weathering which is a confirmed phenomenon in lunar samples. Asteroid 253 Mathilde is a C-class asteroid whose photos were taken by NEAR-Shoemaker. Asteroid 433 Eros is an S asteroid which has been explored by NEAR-Shoemaker in detail. NEAR-Shoemaker observed Eros during 1999 to 2000. Also, the density of Eros, measured in trajectory of spacecraft, was about 2.4 g/cm^3. The size and the density of Eros imply that the inner structure of Eros appears to be fractured rocks.

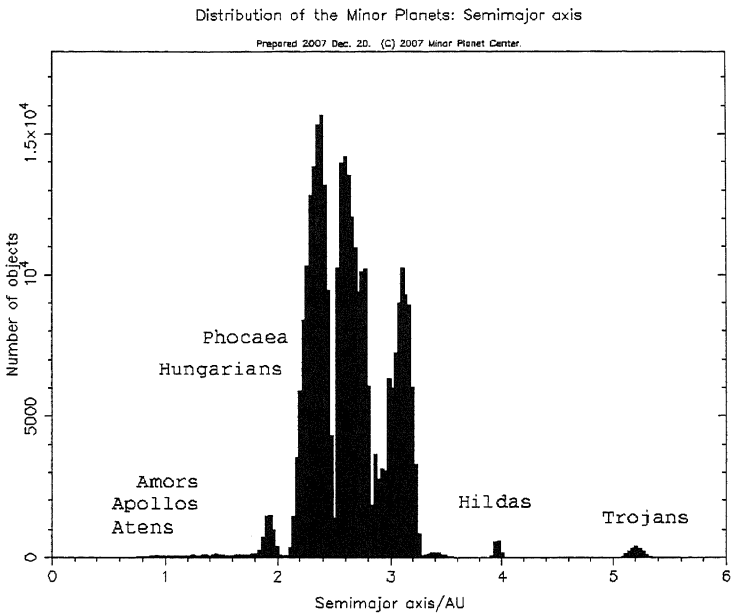

Figure 1.1: Distribution of asteroids in semi-major axis, obtained from http://cfa-www.harvard.edu/. There are many asteroids classified as clans. The NEAs are classified as clans such as Amors, Apollo, and Atens.

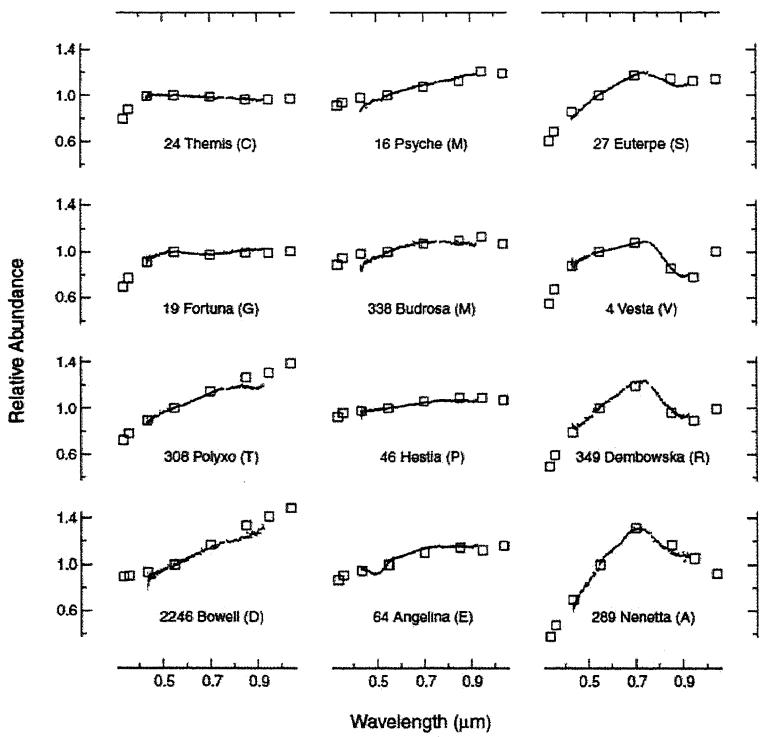

Figure 1.2: Spectral features classified by asteroid taxonomy, obtained from Bus *et al.*, (2002). These data have been observed by ground based visible to near infrared spectroscopy and they have been classified according to albedo and spectral features.

Table 1.1: Asteroid taxonomy (Tholen style), obtained from Tholen and Barucci (1989).

Class	Albedo	Spectrum
C	low	ultraviolet absorption feature shortward of 0.4 μm,
		generally flat to slightly reddish longward of 0.4 μm
G	low	very strong ultraviolet absorption feature shortward of 0.4 μm, flat longward of 0.4 μm;
		differs from the C class in the strength of the ultraviolet absorption feature (subclass of C)
T	low	moderate absorption feature shortward of 0.85 μm, and generally flat longward of 0.85 μm.
D	low	generally featureless spectrum;
		neutral to slightly reddish shortward of 0.55 μm, very red longward of 0.4 μm
M	moderate	featureless spectrum; flat to slightly reddish over entire 0.3 to 1.1 μm wavelength range;
		differs from the spectrally identical E and P classes in albedo only
P	low	featureless spectrum; flat to slightly reddish over entire 0.3 to 1.1 μm wavelength range;
		differs from the spectrally identical E and M classes in albedo only;
		spectra are intermediate between C and D classes
E	high	featureless spectrum; flat to slightly reddish over entire 0.3 to 1.1 μm wavelength range;
		differs from the spectrally identical M and P classes in albedo only
S	moderate	moderate to strong absorption feature shortward of 0.7 μm,
		and moderate to nonexistent absorption feature longward of 0.7 μm
V	moderately	strong absorption feature shortward of 0.7 μm
	high	and strong absorption feature longward of 0.7 μm, centered near the 0.95 μ filter
R	moderately	strong absorption feature shortward and longward of 0.7 μm;
	high	band center between those of A and V classes
A	moderately	extremely reddish shortward of 0.7 μm;
	high	strong absorption feature longward of 0.7 μm,
		centered near the 1.05 μm filter
Q		strong absorption feature shortward and longward of 0.7 μm;
		band center between those of A and V classes

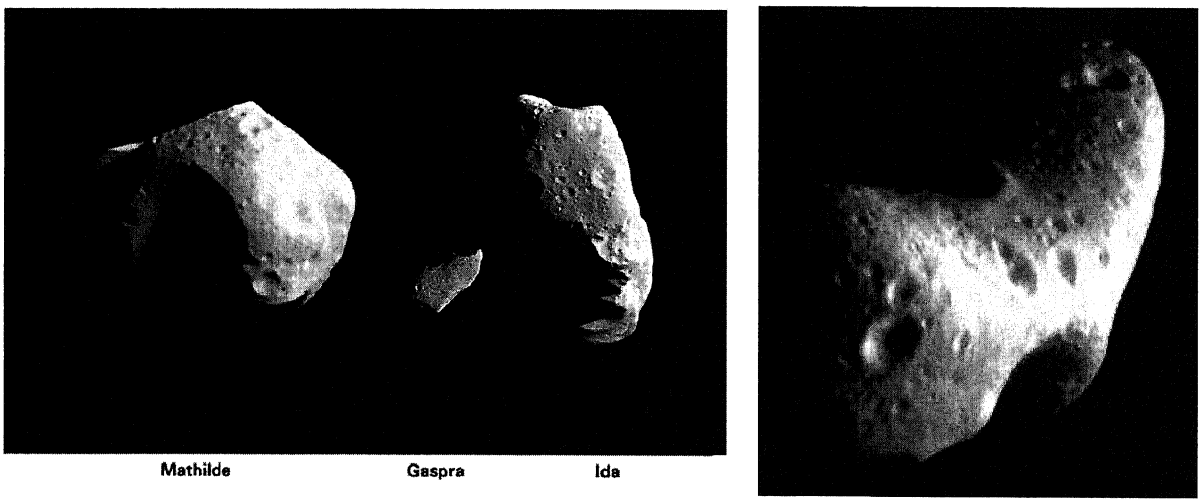

Figure 1.3: Asteroid 951 Gaspra (18.2×10.5×8.9 km^3) and asteroid 243 Ida (53.6×24.0×15.2 km^3) observed by Galileo spacecraft, and asteroid 253 Mathilde (66×48×46 km^3) and 433 Eros (13×13×33 km^3) observed by NEAR-Shoemaker, obtained from NASA's web site.

1.1.2 Review of meteorites

Meteorites are most informative source of the solar system science because the physical properties of the solar system can be directly obtained from analyses of them. Meteorites are classified with analytical methods in chemistry, mineralogy, petrology, and O-isotopic composition (*e.g.*, Weisberg *et al.*, 2006). Many primitive meteorites, containing a chondrule which is a spherical particle in millimeter size, are classified as a chondrite in Table 1.2. In contrast, differentiated meteorites, not including chondrules but having primitive composition are classified as a primitive achondrite as shown in Table 1.3, and totally differentiated meteorites are classified as an achondrite as shown in Table 1.4.

Most popular meteorites, falling to the Earth, are ordinary chondrites. Spectrally, ordinary chondrites have absorption features of Olivines and Pyroxenes in reflectance spectrum of sun light. Ordinary chondrites are composed of chondrules, Olivines, Pyroxenes, plagioclase feldspars and glasses with Olivine-rich matrixes, metals, and sulfides. There are three chemical groups, H, L, and LL, and a range of petrologic types with respect to the degrees of thermal metamorphism, from 3 to 6, and then type 6 has most experienced a heating process. They are classified in mineralogy as follows: Typical H chondrites are composed of Olivine/Pyroxene ratios ~54:46 and metal concentration ~18 vol%. Typical LL-chondrites are composed of Olivine/Pyroxene ratios ~66:34 and metal composition ~4 vol%. LL-chondrites have more distinctive Olivine absorption bands because of their higher Olivine contents.

Major contributions of meteorites analysis to the solar system science can be expected from an age determination as shown in Figure 1.4. Radio isotopic age determination informs us the chronology of meteorites. If asteroid samples can be obtained, elemental distribution of materials and these chronologies will be revealed.

Table 1.2: Chondrites (Undifferentiated).

	chondrite														
Class	Carbonaceous								Ordinary (O)			Enstatite (E)			
Clan	CI	CM-CO		CV-CK		CR clan			H-L-LL			EH-EL			
Group	CI	CM	CO	CV	CK	CR	CH	CB	H	L	LL	EH	EL	R	K

Table 1.3: Primitive achondrites.

	Primitive achondrite						
Clan			ACA-LOD		WIN-IAB-IICD		
Group	URE	BRA	ACA	LOD	WIN	IAB	IICD

Table 1.4: Achondrites (Differentiated).

	Achondrites					Stony Iron				Iron									
Clan			Vesta?																
Group	ANG	AUB	EUC	DIO	HOW	MES	M-PAL	E-PAL	P-PAL	IC	IIAB	IIC	IID	IIE	IIIAB	IIIE	IIIF	IVA	IVB

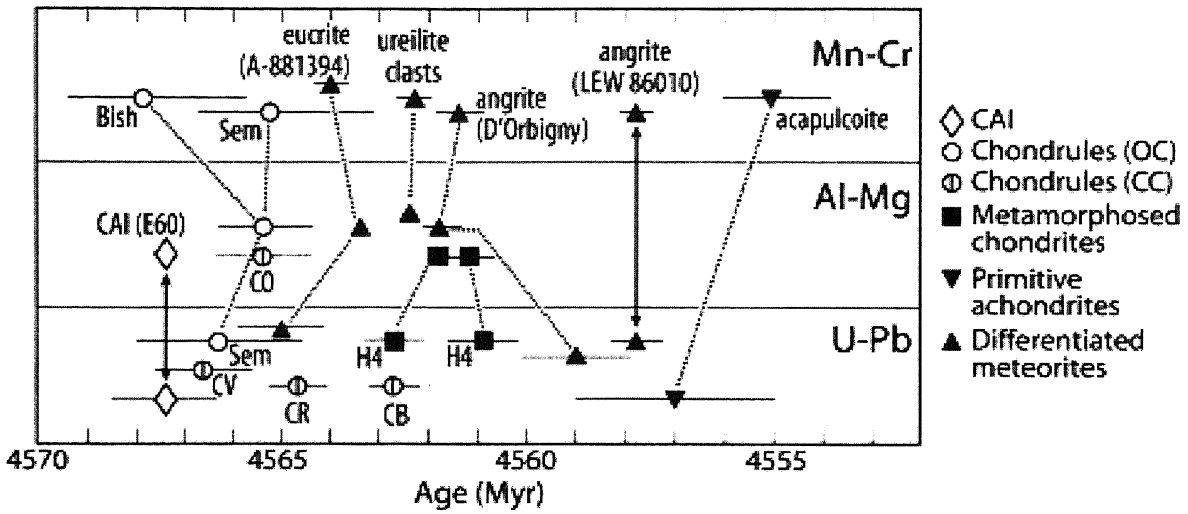

Figure 1.4: Chronology of the early solar system with analysis of Mn-Cr, Al-Mg, U-Pb isotopic method (Scott, 2006). Bish denotes Bishunpur LL3, and Sem denoted Semerkona LL3. Radio isotopic age determination informs us the chronology of meteorites.

1.1.3 Spectral paradox between asteroid and meteorites

Many asteroids have been studied by ground-based observation. However, their albedos and spectral features do not correspond to those of meteorites in many cases. In particular, spectral features are not consistent between S-class asteroids and ordinary chondrites, and then the spectral feature of S-class asteroids is mostly redder than that of ordinary chondrites. S-class asteroids, found in the inner main belt, are most abundant (~80%). They have long been considered possible parent bodies of the ordinary chondrites because large number of those have indicated the similar spectral features of Olivine and Pyroxene as major compositions of the ordinary chondrites. In particular, the spectral features of 1 and 2 μm absorption bands in visible and near-infrared reflectance spectrum (reflectance of sun light) are found in both S asteroids and ordinary chondrites. However, S asteroids are spectrally redder than ordinary chondrites and tend to have weaker absorption. It has long been unclear and has been known as a spectral paradox.

Some researchers have suggested that some of the S asteroids are composed of ordinary chondrites, and only small asteroids (diameters < 10 km) may be the parent body of ordinary chondrites because small asteroids should not have experienced a differentiation due to melting by release of self gravitational energy. If so the reflectance spectrum of small objects should not have redder and weaker absorption features (*e.g.*, Burbine *et al.*, 2002).

Gaffey *et al.* (1993) have classified the spectral feature of S-class asteroids in details as subtypes. S-class asteroids related to stony and stony-iron meteorite-analogues are shown in Table 1.5, where the spectral feature of S asteroid are similar to not only that of stony meteorites but also that of stony iron meteorites. Probably, abundant metal (Fe-Ni) in silicates causes relatively reddened and darkened spectra in 1 and 2 μm absorption band compared to the mixtures of pure olivine and pyroxenes. Although ordinary chondrites also include Fe-Ni metal, these particles are too small to cause the reddened and darkened spectra. Hence, mixtures of ordinary chondrites and large amount of iron meteorites may resolve the spectral paradox.

Many researchers have considered that space weathering is not effective in the surface of asteroids because there is no regolith on the asteroid surface like a lunar soil altered by space

weathering. Also, they have considered that the escape velocity of asteroid is too low for the regolith to remains on the surface. However, Chapman *et al.* (1996) have suggested that space weathering causes color variation in the surface material of asteroids 951 Gaspra and asteroid 243 Ida observed by the Galileo spacecraft. Recently, space weathering process in the surface of asteroids has been proposed from experimental evidence. Some researchers (*e.g.*, Pieters *et al.*, 2000; Hapke, 2001; Sasaki *et al.*, 2001) have suggested that the impacts of micro meteorites and/or the ion sputtering of solar wind make nano phase iron on the uppermost surface in reduced condition, and then they cause the reddish and darker feature in visible and near infrared spectrum.

It is important to find out whether the origin of the paradox is the mixtures of metallic Fe materials, space weathering or another process in order to connect the missing link between asteroids and meteorites.

Table 1.5: S asteroid subtypes and possible meteorite analogues, obtained from Gaffey (1993).

Subtype	Possible meteorite analogues
S(I)	Pallasites
	Pyroxene-poor Ureilites
	Pyroxene-poor Brachinites
	Olivine-metal partial melt residues
S(II)	Cpx-bearing Ureilites
	Cpx-bearing Brachinites
	Olivine-Cpx cumulates
	Cpx-bearing Pallasites
	highly metamorphosed C-type assemblages
S(III)	Cpx- and opx-bearing Ureilites
S(IV)	Opx-bearing Ureilites
	Lodranites
	Winonaites and IAB irons
	H,L,LL Chondrites
S(V)	Lodranites
	Cpx-basalt intrusions into H-chondrite matrix
S(VI)	Siderphyres (Steinback)
	Lodranites
	Winonaites and IAB irons
	Subsolidus-reduced chondrites
	Anorthosite
S(VII)	Mesosiderites
	Siderphyres (Steinback)
	Lodranites
	Winonaites and IAB irons
	Cpx-poor Mesosiderites
	Subsolidus-reduced chondrites
	Anorthosite

1.2 Overview of the Hayabusa mission

Hayabusa is the first spacecraft who explored near-Earth objects in order to reveal the relationship between asteroids and meteorites. The Hayabusa spacecraft was launched by the 5th M-V launch vehicle May 9, 2003 as shown in Figure 1.5 and rendezvoused with near-Earth asteroid 25143 Itokawa September 12, 2005.

The main purpose of the Hayabusa mission is demonstration of new technologies such as ion thruster, interplanetary cruise using the ion thruster, autonomous navigational control at 300 million km away from the Earth, and sample return in micro gravity.

Science observation is also the important aims of the Hayabusa mission. Recently, un-

manned spacecraft has obtained some information such as imaging and spectroscopy of some asteroids but the data are not sufficient to reveal the relationship between asteroids and meteorites because they have not obtained any direct evidence such as samples. Therefore, Hayabusa carried out a sample return and rendezvous observation of asteroid 25143 Itokawa, including spectroscopy, imaging, and geological and topographical measurements (Fujiwara, *et al.*, 2006). The science instruments are X-ray fluorescence spectrometer (XRS), Near Infrared Spectrometer (NIRS), multi-band camera (AMICA), and laser altimeter (LIDAR); The NIRS measured a surface mineralogy, the AMICA took images and made mineralogical and morphological measurements in the surface, including measurement of distribution of craters and boulders. The XRS observed X-ray emission from the surface materials of Itokawa in order to determine these major chemical compositions.

(a) The Hayabusa spacecraft

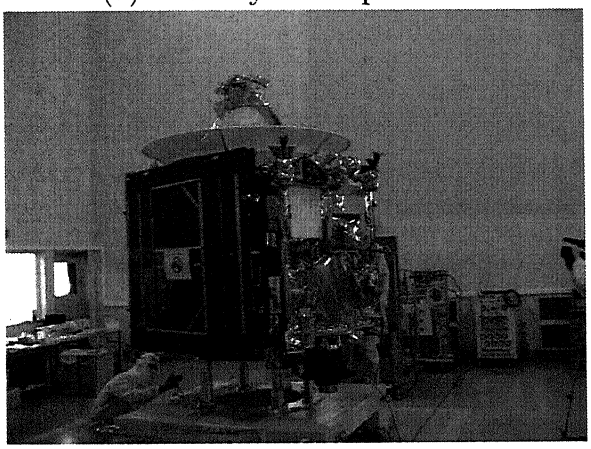

(b) M-V launched

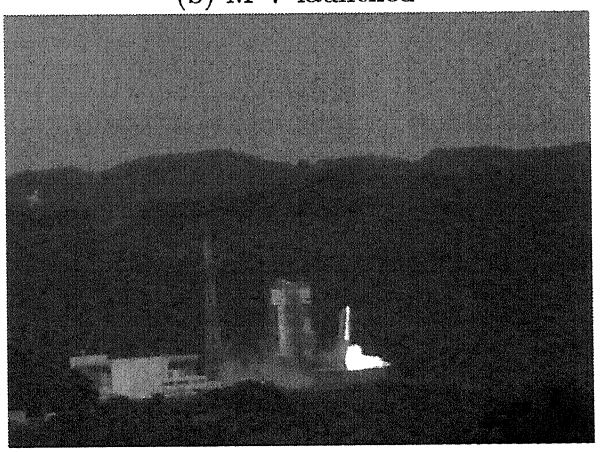

Figure 1.5: (a) The Hayabusa spacecraft, (b) The Hayabusa spacecraft was launched by 5th M-V launch vehicle May 9, 2003.

1.3 Current knowledge of asteroid 25143 Itokawa

Asteroid 25143 Itokawa is the first asteroid in near-Earth objects explored by unmanned spacecraft (Figure 1.6). It was discovered by a 1 m folded Cassegrain-type telescope of the LINEAR project in 1998 (http://www.ll.mit.edu/LINEAR/), and its trajectory was determined. Figure 1.7 shows the trajectory of Itokawa. Itokawa is considered to have came from the main belt owing to the chaotic perturbation of kinetic force (*e.g.*, Michel and Yoshikawa, 2005).

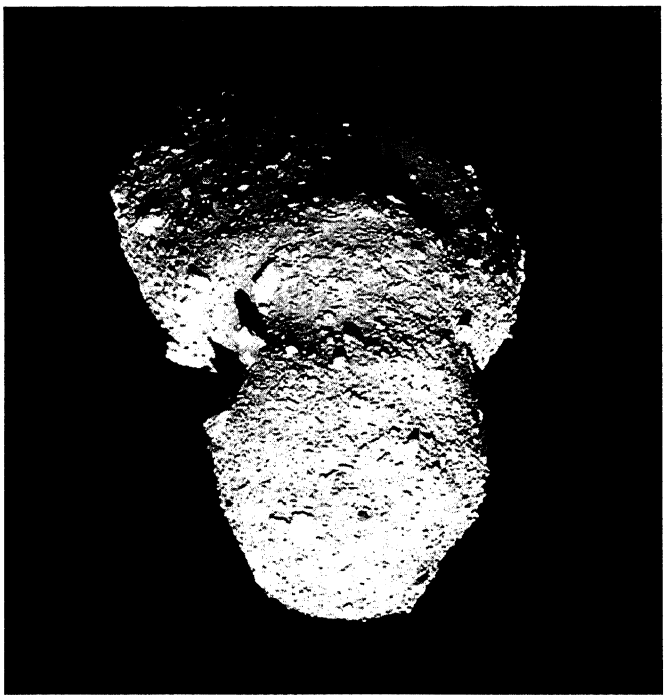

Figure 1.6: Picture of Itokawa, taken by the AMICA onboard the Hayabusa spacecraft. The black boulder is found below the center of the picture.

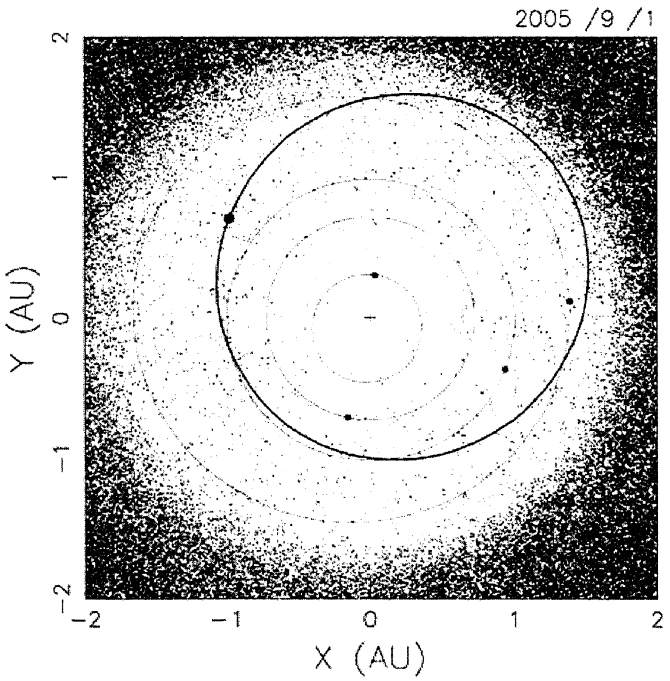

Figure 1.7: The trajectory of Itokawa plotted on the heliocentric coordinate system, obtained from JAXA's web site.

1.3.1 Results of ground-based observation

In ground-based observation, Itokawa has been classified as an S class asteroid and an S(IV) subtype (Table 1.5) by visible and near infrared spectral features (Binzel *et al.*, 2002) as shown in Figure 1.8. Its rotation period, measured by light curve in ground-based photometry, is 12.1324±0.0001 hours (Nishihara *et al.*, 2005). Also, the albedo is 0.3 (Lederer *et al.*, 2005). Thermal inertia has been measured by Müller *et al.* (2005), and the result ($\sim$750 $\mathrm{Jm^{-2}s^{-0.5}K^{-1}}$) has indicated that the surface materials on Itokawa may be composed of intermediate materials between rocks and sands. Shape model has been constructed by light curve observation (Kaasalainen *et al.*, 2002) and radar observation (Ostro *et al.*, 2004) as shown in Figures 1.9a and 1.9b, respectively. They were used to estimate the rotation period of Itokawa and detail orbits of Itokawa.

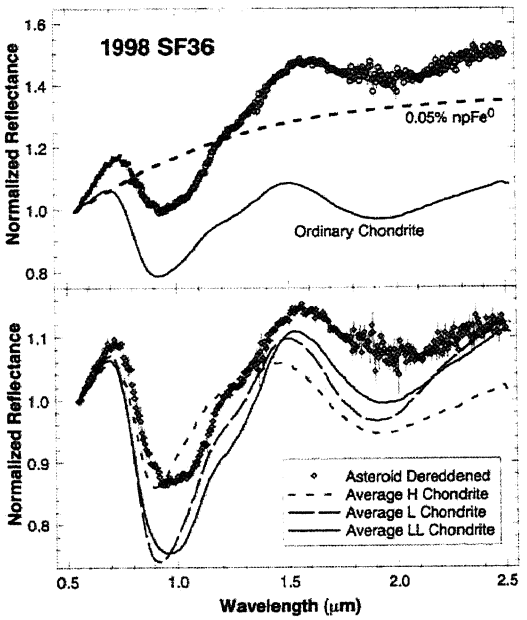

Figure 1.8: Itokawa observed by ground based visible and infrared spectroscopy, obtained from Binzel *et al.* (2001). The band absorption in about 1 μm is shallower than that of pure silicates. It is considered to be caused by abundant metal in silicate or surface alteration by space weathering.

(a) Light curve observation (b) Radar observation

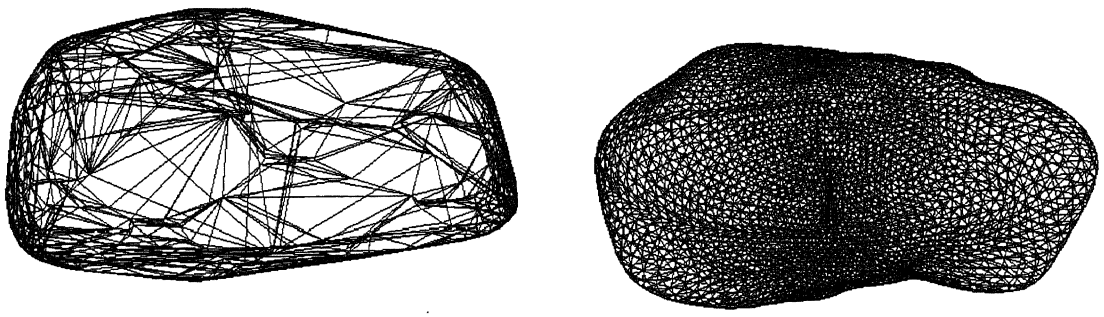

Figure 1.9: Itokawa shape model constructed by results of ground-based observation. (a) Constructed by light curve observation (Kaasalainen *et al.*, 2003). (a) Constructed by radar observation (Ostro *et al.*, 2004).

1.3.2 Preliminary results of rendezvous observation

The results of observation with some instruments onboard Hayabusa have suggested that Itokawa is compositionally similar to ordinary chondrites. They are consistent with the results of this study and details are described below.

Preliminary results of NIRS observation

The NIRS observed the surface materials in the wavelengths of 0.8 to 2.1 μm as shown in Figure 1.10. This result has indicated that the compositional variation was not fond in the surface but color and reflectance vary from areas to areas (Abe *et al.*, 2006). Also the results have indicated that the ratio of Olivine/(Olivine+Pyroxene) was 70% to 80%, derived from about 1 μm absorption band, are thus the mineral composition in the surface of Itokawa similar to LL-chondrites. Petrologic type of Itokawa was also derived from the band ratios such as 0.95, 1.01, and 1.25 μm, and the result indicates that the petrologic type of Itokawa is type LL5 or LL6 (Abe *et al.*, 2006). It implies that the surface materials on Itokawa were affected by a heating process.

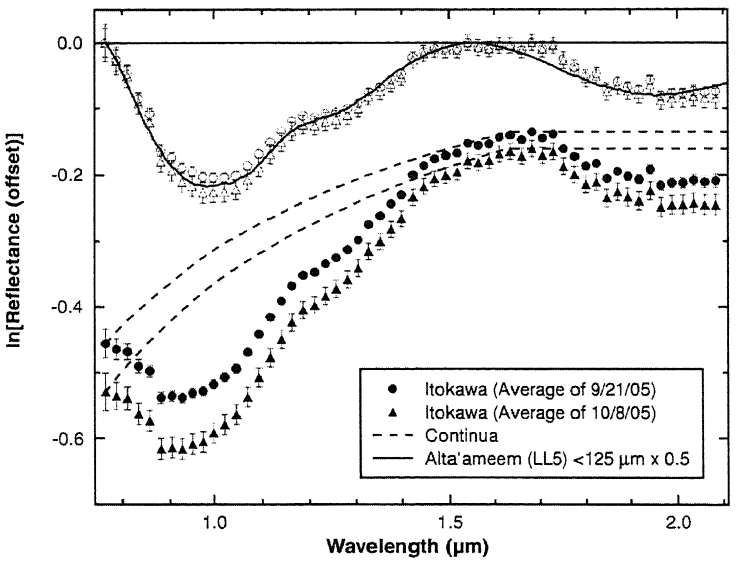

Figure 1.10: Near-infrared average reflectance spectra of Itokawa observed by the NIRS are shown in natural log, obtained by Abe *et al.*, (2006). Background continua (broken curves) are subtracted from observed spectrum and they are plotted (open circles and triangles) together with the continuum-removed spectrum of an Alta'ameem LL5 chondrite sample (solid line).

Preliminary results of the XRS observation

Preliminary results of the XRS have indicated that the surface elemental ratios of Mg/Si and Al/Si resemble ordinary chondrites (Okada *et al.*, 2006a) as shown in Figure 1.11. The data analysis has been carried out by a comparative analysis (Masuda, 2002) for decent phase (touch down phase #1), directly comparing the intensities of X-rays from Itokawa and from the onboard standard sample. The X-ray intensities for fluorescence line spectra of Mg, Al, and Si were estimated; A polynomial function was used to represent the background spectrum, and a Gaussian function was assumed to be the response for each line spectrum. The phase angle (the Sun-to-Itokawa-to-detector) was assumed to be 0°, where the attitude of spacecraft was controlled in such a way that the phase angle is less than 10°. Although these simple assumptions

were practical and often used for X-ray spectroscopy, there are potential problems as described below: (1) Using a polynomial function as spectral background is not always the most practical method for quantitative analysis, and thus it needs precise background functions, such as scattering solar X-rays, space radiation, and instrumental background. (2) Temporal change of the observed phase angle causes apparent changes in the elemental composition ratios, and thus it needs to be corrected by using a precise surface geometry for X-ray incident and emission angles. (3) The actual response function of the XRS is not a Gaussian but a Gaussian-like function, and thus a precise response function is necessary to be constructed.

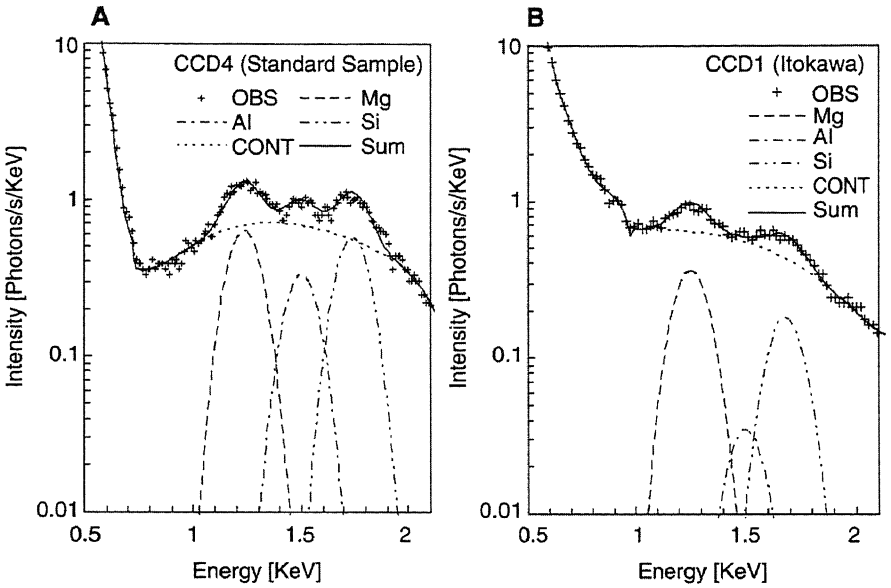

Figure 1.11: X-ray spectra of the onboard standard sample (A) and asteroid Itokawa (B) were simultaneously obtained by the XRS at 9:27 UTC November 19, 2005, obtained from Okada *et al.*, (2006). The observed spectra (OBS) are fitted by Gaussian for Kα lines of major elements (Mg, Al, and Si), and they were assumed to be a background as continuum (CONT).

Reddish and darker features

In rendezvoused observation, reddish and darker features have been also found in repentance spectra of the NIRS (Abe *et al.*, 2006). Although the spectral feature of Itokawa was more reddish and darker, it was similar to that of ordinary chondrites, especially of LL-chondrites after corrected background continuum.

Surface heterogeneity

In the observations of Itokawa, brightness and color variations in the surface have been found with the multi-band imager AMICA (*e.g.*, Saito *et al.*, 2006; Ishiguro *et al.*, 2006; Sasaki *et al.*, 2006) as shown in Figure 1.12, and the near-infrared spectrometer NIRS (Abe *et al.*, 2006). Ishiguro *et al.* have suggested that most reddened area is probably deposit of matured materials by space weathering. Also, average of albedo was 30% and it varied in the range of 10 to 20% (Sasaki *et al.*, 2006) in the surface.

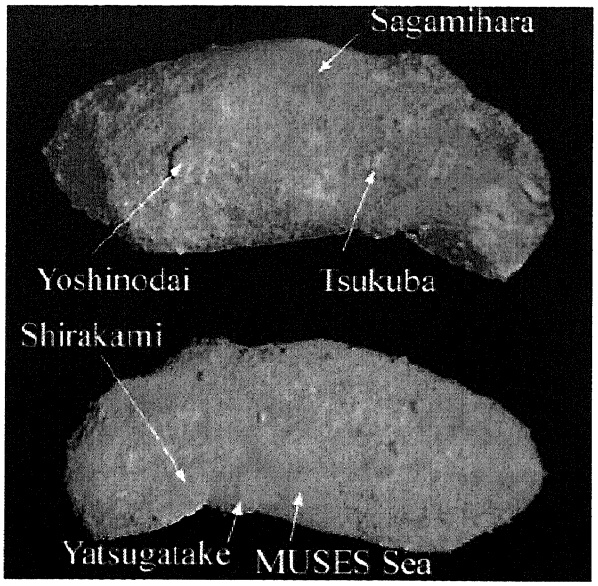

Figure 1.12: False color images obtained from the AMICA (modulated "w" band to "b" band). This redder color indicates more altered area by space weathering, obtained from Ishiguro *et al.* (2006).

Rubble-pile structure

The mass of Itokawa is very small ($3.51 \pm 0.105 \times 10^{10}$ kg), and also its density is small (1.9 $\pm$ 0.13 g/cm^3), as measured by the trajectory of spacecraft (Fujiwara *et al.*, 2006). Since the macroporosity of Itokawa is large ($\sim$0.41) as shown in Figure 1.14, Itokawa is probably composed of very fractured rocks called a rubble-pile (Fujiwara *et al.*, 2006) as schematically shown in Figure 1.13. Portions of partial melting features have been found in Itokawa at about 2 micron absorption band of the NIRS and also found in the Earth-based observations (Abell *et al.*, 2006). These results have indicated that the portion of Itokawa is more enriched in Olivine than that of primitive ordinary chondrites. It may be caused by fraction due to melting.

Figure 1.13: Schematic image of rubble-piles, obtained from Fujiwara *et al.*, (2006). Fractures due to impacts make small portions of rocks.

(a) Mass *vs.* Density

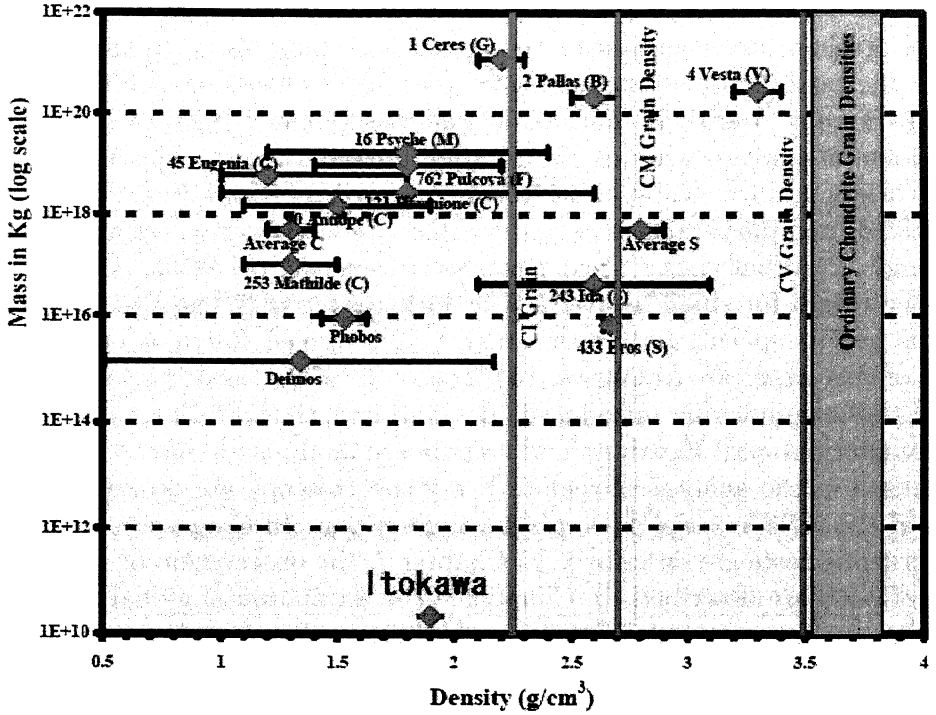

(b) Mass *vs.* Macroporosity

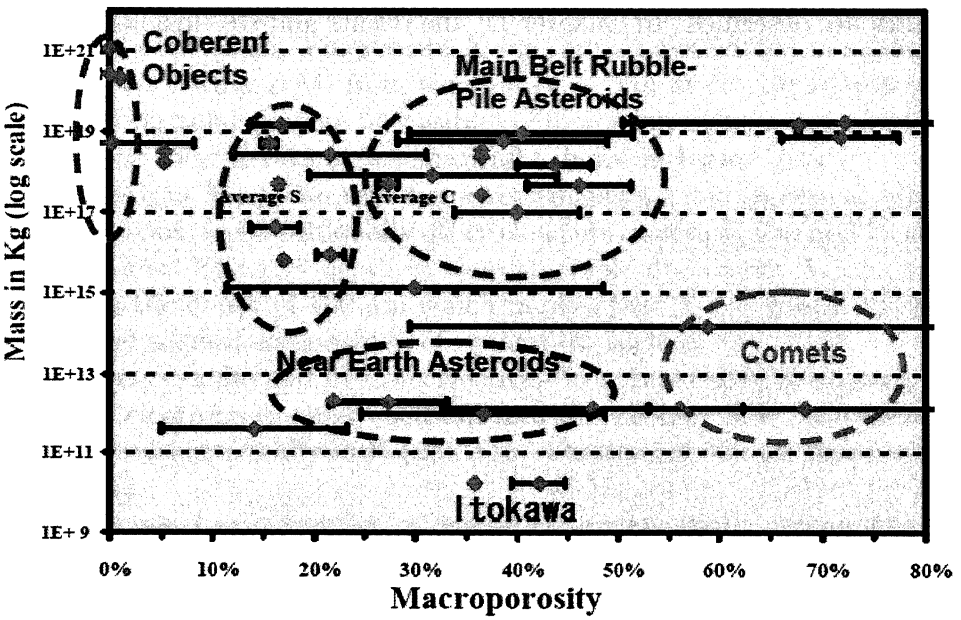

Figure 1.14: (a) Mass *vs.* density relation for asteroids. The mass ($3.51 \pm 0.105 \times 10^{10}$ kg) and density ($\sim 1.9 \pm 0.13$ g/cm^3) of Itokawa are very small compared to ever explored asteroids. The densities of asteroids, plotted on this figure, are modified from Britt *et al.* (2001). (b) Mass *vs.* macroporosity relation for asteroids. Macro porosities of asteroids are modified from Britt *et al.*, (2006). Upper right asteroids represent M type.

1.4 Objectives of this study

In this study, major elemental composition in the surface materials of Itokawa is estimated, and it related to the possible meteorite-analogues such as Opx-bearing Ureilites, Lodranites, Winonaites and IAB irons, and H, L-, and LL- Chondrites (Gaffey, 1993) or other candidates, including a fundamental question whether the asteroids are the parent body of meteorites or not. Additionally, the origin and the evolution of Itokawa are discussed as follows: (1) What causes the spectrally reddish and darker features, and whether they are caused by metal mixtures or a space weathering? (2) What causes the surface heterogeneity? (3) What is the parent body of Itokawa and the origin for small object in near-Earth asteroid? These are the first major elemental analysis and its speculation for the small bodies in near-Earth asteroids.

The contents of this paper are as follows: In Chapter 2, the methodology of a remote X-ray spectroscopy and past examples are introduced. In Chapter 3, the instrumentation of X-ray fluorescence spectrometer onboard Hayabusa and its onboard analysis are introduced. In Chapter 4, X-ray models used in the analysis of remote X-ray spectroscopy are described. In Chapter 5, performances of the XRS in pre-launch tests are described. In Chapter 6, performances of the XRS in the cruising tests are described. In Chapter 7, the observation of Itokawa with the XRS and status of XRS are described. In Chapter 8, the estimation of global major elemental composition for the surface materials of Itokawa and the results of analysis are described. In chapter 9, the estimation of local major elemental composition for the surface materials of Itokawa and the results of analysis are described. In Chapter 10, the discussion of the relationship between Itokawa and meteorite-analogues, and the speculation of the origin and the evolution of Itokawa are described. In Chapter 11, the results and conclusions of this study are described.

Chapter 2

Remote X-ray fluorescence spectroscopy

In this chapter, the basic theories and methods of remote X-ray fluorescence spectroscopy are described.

2.1 Basic theory of fluorescent X-ray excitation

X-ray fluorescence spectroscopy, used for quantitative analysis of elements, is a confirmed method in laboratory experiments but remote X-ray fluorescence spectrometry has been performed in space only a few times. Fluorescent X-rays are always excited in sunlit areas of solid planets by solar X-rays within 2 AU from the Sun (*e.g.*, Yin *et al.*, 1993), where quantitative analysis of elements on solid planets is feasible. Fluorescent X-rays are also excited in the surface of asteroids by solar X-rays as schematically shown in Figure 2.1a.

Measurable fluorescent X-rays for remote measurements are line spectra of Mg, Al, and Si in quiescent solar conditions, and additionally other elements such as S, Ca, and Fe are measurable in solar flare conditions. Effective depth in the detectable fluorescent X-rays from the rocky surface are less than the depth of 100 μm which implies that X-ray fluorescence spectroscopy can estimate major elemental composition of uppermost surface.

Incident solar X-rays excite and flick out electrons from inner shell of atoms by a photoelectric effect, and then electrons in outer shell fall into the vacancy hole, and fluorescent X-rays are emitted as shown schematically in Figure 2.1b. Fluorescent X-rays flux is proportional to elemental abundance.

Incident solar X-rays J as a function of energy are exponentially attenuated in the surface layer in the ratio of μ_i for element i as function of energy, called attenuation coefficient as follows,

$$I(E_i) = \int J(E) \exp\left(-\frac{\rho \mu_i(E) z}{\cos\phi_1}\right) dE,$$

where I is the X-ray intensity, z (cm) is the depth, ρ is the density (g/cm^3) of target material, $\mu_i(E)$ is the mass attenuation coefficient (cm^2/g) (Figure 2.2), and ϕ_1 is the incident angle of solar X-rays as schematically shown in Figure 2.3. Then, the intensity of fluorescent X-rays, emitted in z ($z = z \sim z + dz$), is written as follows,

$$dI(E_i) = \omega_i t_i s_i j_i \rho \int \mu_i(E) J(E) \exp\left(-\frac{\rho \mu_i(E) dz}{\cos\phi_1}\right) dE,$$

where ω is fluorescence yield in conversion ratio of incident X-rays to fluorescent X-rays, s_i is probability of line emission for element i (α or β), t_i is the ratio of shell transition probability

for element i, and j_i is the jump ratio which is the K or L shell absorption ratio for element i. Fluorescent X-rays are absorbed in the nearby layer in the ratio of τ_i for element i as function of energy, called absorption coefficient. Also, fluorescent X-rays are attenuated in the ratio of μ_i before being emitted from the surface as follows,

$$dI(E_i) = \omega_i t_i s_i j_i \rho \int \tau_i(E) J(E) \exp\left(-\frac{\rho\mu_i(E)dz}{\cos\phi_1}\right) \exp\left(-\frac{\rho\mu_i(E^f)dz}{\cos\phi_2}\right) dE,$$

where ϕ_2 is the emission fluorescent X-ray angle. Here, total intensities of attenuated and absorbed X-rays are given as integrated in the depth D as follows,

$$\begin{aligned} I(E_i) &= \omega_i t_i s_i \rho \int \tau_i(E) J(E) \int_0^D \exp\left(-\frac{\rho\mu_i(E)}{\cos\phi_1} - \frac{\rho\mu_i(E^f)}{\cos\phi_2}\right) dz dE \\ &= \omega_i t_i s_i \int \frac{\tau_i(E)J(E)}{\frac{\mu_i(E)}{\cos\phi_1} + \frac{\mu_i(E^f)}{\cos\phi_2}} \left(1 - \exp\left(-\frac{\rho\mu_i(E)}{\cos\phi_1} - \frac{\rho\mu_i(E^f)}{\cos\phi_2}\right) D\right) dE. \end{aligned}$$

When the size of target materials is sufficiently larger than the X-ray depth, D is assumed to be ∞. Then, the intensity of fluorescent X-rays are given as follows,

$$I(E_i) = \omega_i t_i s_i \int \frac{\tau_i(E)J(E)}{\frac{\mu_i(E)}{\cos\phi_1} + \frac{\mu_i(E^f)}{\cos\phi_2}} dE. \tag{2.1}$$

This equation is called Sherman's equation (*e.g.*, Jenkins, 1995; Clark and Trombka, 1997).

(a) Remote X-ray fluorescence observation

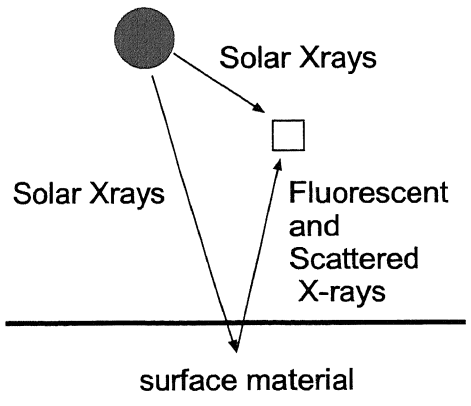

Fluorescent X-rays excitation

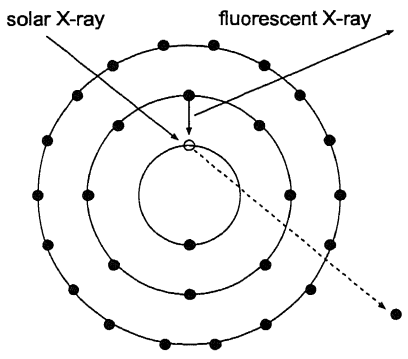

Figure 2.1: (a) **Fluorescent X-rays from the surface materials on a solid state planet, excited by solar X-rays, are remotely sensed by an X-ray detector. In order to quantitatively estimate the elemental abundance of the surface, estimation of incident solar X-rays is required. (b) Incident X-rays excite and flick out electrons in an inner shell of atom by a photoelectric effect, and then electrons in outer shells fall in to the vacancy hole, and fluorescent X-rays are emitted.**

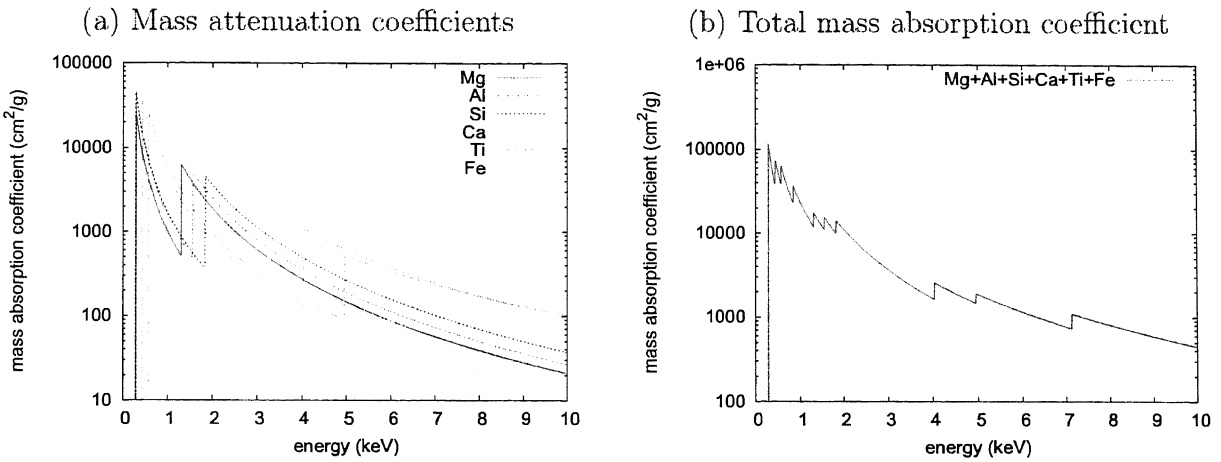

Figure 2.2: (a) Mass attenuation coefficients for each element μ_i. (b) Total mass absorption coefficient $\sum_i w_i \mu_i$ assumed to be the mass fraction of LL-chondrite analogues. They are exponentially proportional to attenuation of X-ray intensity.

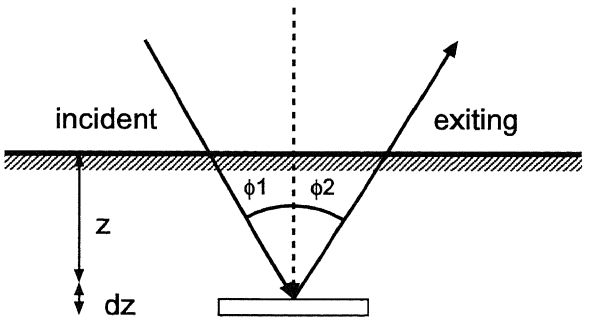

Figure 2.3: Incident solar X-rays are attenuated in upper layer and excite fluorescent X-rays in the neighboring layer (dz). The fluorescent X-rays are also attenuated in an upper layer, and are exiting in space.

2.2 Review of past X-ray fluorescence observation

Remote X-ray fluorescence observations were carried out for the moon and asteroids by the Apollo 15 and 16 missions and the Near-Earth Asteroid Rendezvous (NEAR)-Shoemaker mission, respectively.

2.2.1 X-ray experiments in the Apollo 15 and 16 missions

The X-ray fluorescence spectrometer onboard Apollo 15 and 16 was based on proportional counters (Adler *et al.*, 1972, 1973) as shown in Figure 2.4.

X-ray fluorescence spectrometer onboard Apollo revealed that there are two types of terrain (dichotomy) in the surface of moon such as maria (mare Crisium, mare Serenitatis, and mare Tranquillitatis, which has lower abundances of aluminum and higher abundances of magnesium). The opposite pattern to maria, observation results in highland indicated higher aluminum and lower magnesium abundances in there. Figure 2.5 shows elemental ratios, Mg/Si and Al/Si, mapped in areas of 9% in the moon.

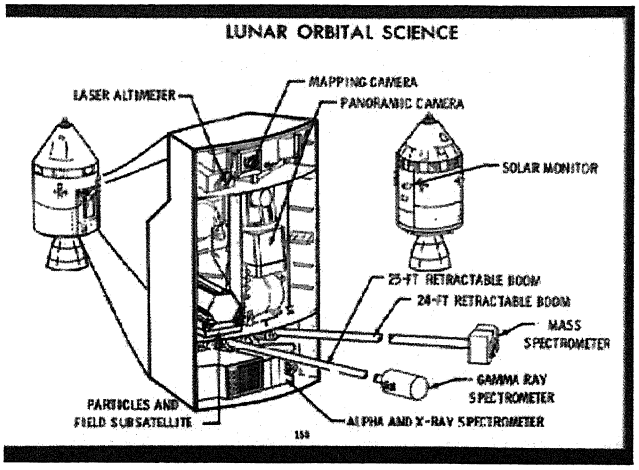

Figure 2.4: Apollo 15 and science instruments illustration, obtained from NASA's web site. The X-ray fluorescence spectrometer onboard Apollo 15 and 16 were based on proportional counters. They are shown in bellow together with alpha particle spectrometer.

(a) Mg/Si ratios

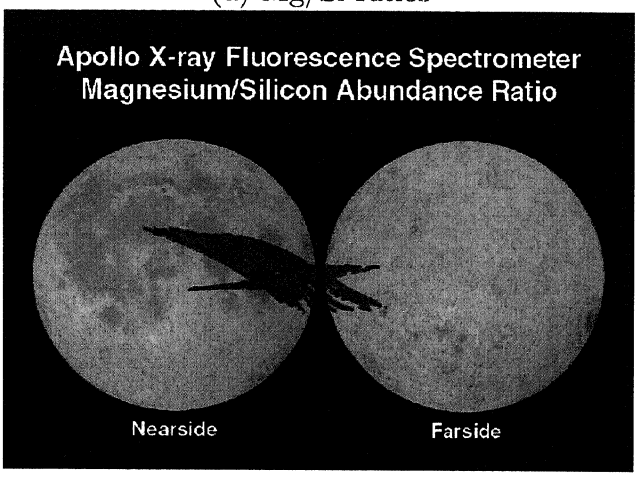

(b) Al/Si ratios

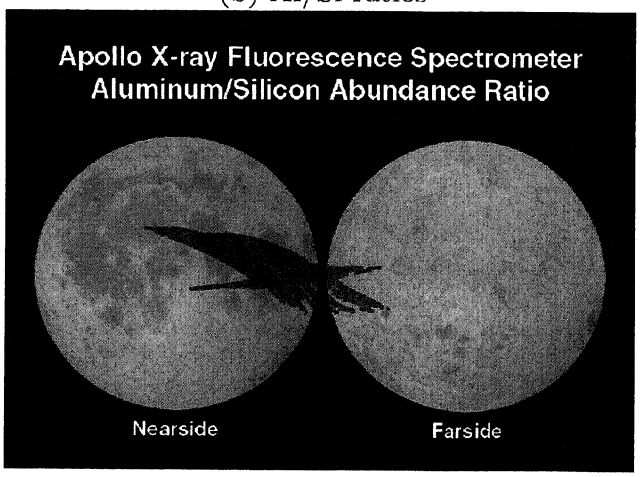

Figure 2.5: (a) Mg/Si ratio. (b) Al/Si ratio. There are two types of terrain in the surface of moon, where opposite patterns are found; higher aluminum and lower magnesium abundances in highlands, while lower aluminum and higher magnesium abundances in Maria, respectively.

2.2.2 X-ray experiments in the NEAR-Shoemaker mission

The X-ray fluorescence spectrometer (XRS) onboard NEAR-Shoemaker (Figure 2.6a) was based on gas proportional counters and developed to measure the surface major elemental composition of asteroid 433 Eros (Goldstein *et al.*, 1997). It remotely sensed characteristic x-rays, and measured elemental compositions in the surface of Mg, Al, Si, Ca, Ti, and Fe with spatial resolutions less than 2 km.

Three gas-filled proportional counters are mounted on the XRS onboard NEAR-Shoemaker (Figure 2.6b). In order to separate the energy peak of fluorescent X-rays, the sensors have filters such as only a Beryllium filter (bare), Mg+Be filters, and Al+Be filters. It was analogy to the XRS onboard Apollo, and then the same analysis method was also used with Apollo style analysis. The background (*i.e.*, scattering X-ray of solar X-ray) were not separated from the observed spectra, and then large estimation errors were included in the results. Also, two solar monitors were mounted on the top deck of the spacecraft to estimate incident solar X-rays. One of the solar monitors was also gas-filled proportional counter. The other solar monitor was a solid state Si detector. The gas-filled proportional counters, collimated to a 5° field of view, had an energy resolution of about 0.84 keV Full Width at Half Maximum (FWHM) at 5.9 keV. The solid state solar monitor had a FWHM of about 0.60 keV at 5.9 keV. ^{55}Fe calibration source was mounted for in-flight calibration of the main sensor.

Figure 2.7 shows elemental mass ratios, Mg/Si *vs.* Al/Si, Mg/Si *vs.* S/Si, Al/Si *vs.* Ca/Si, and Mg/Si *vs.* Fe/Si observed by X-ray spectrometer onboard NEAR-Shoemaker (Lim *et al.*, 2005). The major elemental composition of Eros was similar to that of H- or L-ordinary chondrites but other instruments indicated that composition of Eros was similar to that of LL- or L-ordinary chondrites (*e.g.*, McCoy *et al.*, 2001).

The elemental mass ratio of S/Si in the surface was much lower than that of average composition of ordinary chondrites, which has been reported by Trombka *et al.* (2000) and Nittler *et al.* (2001). They have suggested that the reason for low S/Si was impact-induced volatilization and/or photo- or ion-induced sputtering at the surface materials of the asteroid, or loss of FeS-rich material due to partial melting.

(a) NEAR-Shoemaker

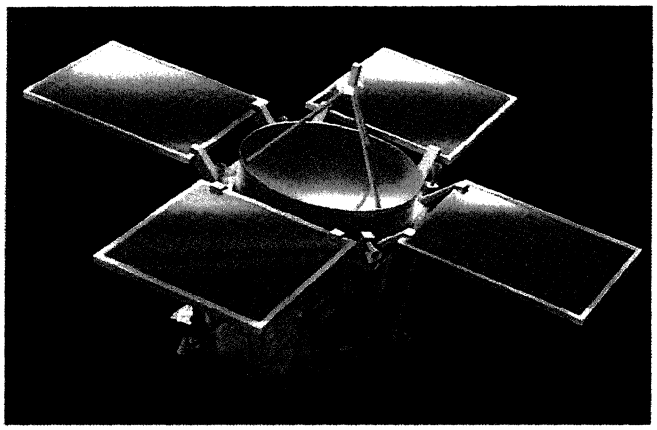

(b) XRS onboard NEAR-Shoemaker

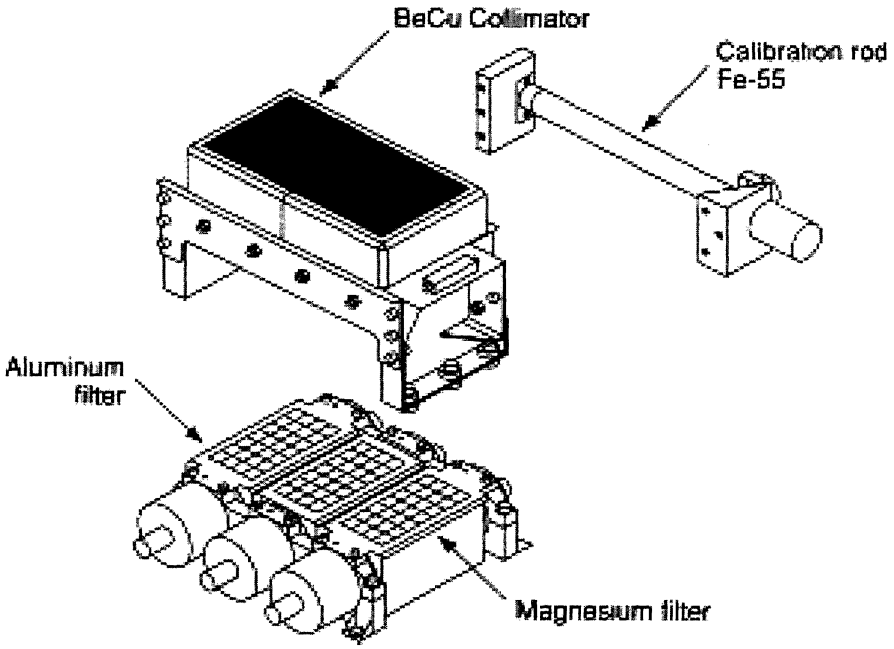

Figure 2.6: (a) NEAR-Shoemaker and (b) X-ray spectrometer, illustration obtained from http://near.jhuapl.edu/. The main sensors of XRS onboard NEAR-Shoemaker are composed of three gas-filled proportional counters with only a Beryllium filter (bare), Mg+Be filters, and Al+Be filters, respectively. They have an energy resolution of about 0.84 keV Full Width at Half Maximum (FWHM) at 5.9 keV.

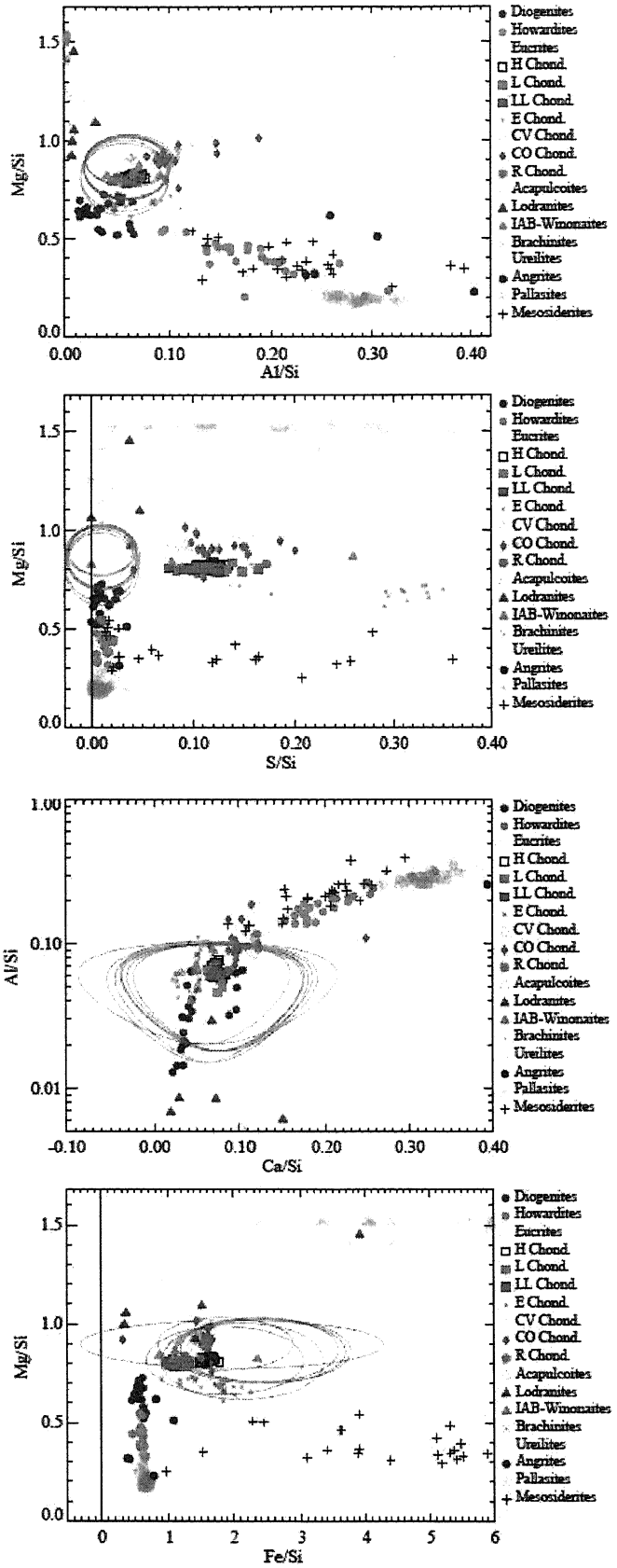

Figure 2.7: Observation results of asteroid 433 Eros by XRS onboard NEAR-Shoemaker, plotted with the elemental ratios of meteorite-analogues, such as Mg/Si *vs.* Al/Si, Mg/Si *vs.* S/Si, Al/Si *vs.* Ca/Si, and Mg/Si *vs.* Fe/Si, obtained from Lim *et al.*, (2005). The results indicated that the surface elemental composition of Eros similar to ordinary chondrite-analogues but the elemental ratio of S/Si is much lower than that of chondrites.

Chapter 3

X-ray fluorescence spectrometer onboard Hayabusa

In this chapter, the specification of X-ray fluorescence spectrometer onboard Hayabusa, characteristics of CCD, and data reduction logics are described.

3.1 Specification of XRS

The XRS is a charge-coupled device (CCD) based X-ray fluorescence spectrometer (Figure 3.1), composed of an asteroid detector and a solar monitor. They perform X-ray measurements with a good energy resolution (Okada *et al.*, 2000; 2006b) relative to the past X-ray detectors of planetary missions such as Apollo 15 and 16, and NEAR-Shoemaker.

The asteroid detector, with arrays of four CCDs (CCD#0, 1, 2, and 3), observes X-ray photons from the surface materials of asteroids. Energy resolution (full width at half maximum) of CCDs is about 180 eV at 5.9 keV in the detection energy range of 0.7 to 10.0 keV. The footprint at observation area of asteroid detector is limited with a mechanical collimator whose field of view is 3.5°×3.5°. Bright visible reflection from the target is shielded with a beryllium window (5 μm thickness). The effective area of the asteroid detector is 25 cm^2 (four pieces of CCD chips), and effective pixels of CCD are 1024×1024, with one pixel size of 24 μm^2. The CCD is not used for imaging but for photon counting of X-rays. This is an energy dispersion detector.

The solar monitor is also a CCD-based detector (CCD#4) whose effective area is 1/4 of asteroid detector. It always monitors a glass plate called a standard sample. The standard sample whose size is 14.76 cm^2 is mounted on +Y plane of Hayabusa in the Hayabusa coordinate system, exposed in space, as shown schematically in Figure 3.2. Elemental compositions of the standard sample are known as shown in Table 3.1, that resemble mixtures of CI chondrites-analogues and basalts-analogues. Since the standard sample is a glass plate, its elemental composition is almost homogeneous.

The electronics onboard the XRS called XRS-E contains analog and digital electronics and onboard computer (SH-OBC) (Yamamoto, 2002). It performs a telemetry and command interface, power supply, CCD driver, data acquisition, data handling, and onboard analysis. XRS-E supplies the drive clocks of CCD to sensors (XRS-S) and receives the signal of CCD from XRS-S as schematically shown in Figure 3.3.

(a) The XRS

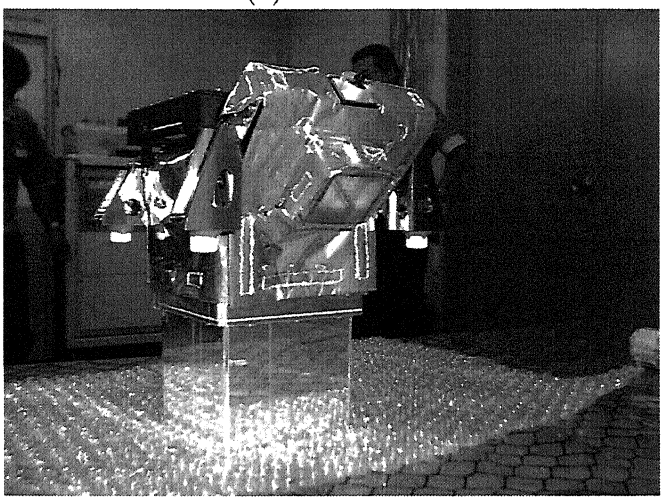

(b) inside of the XRS

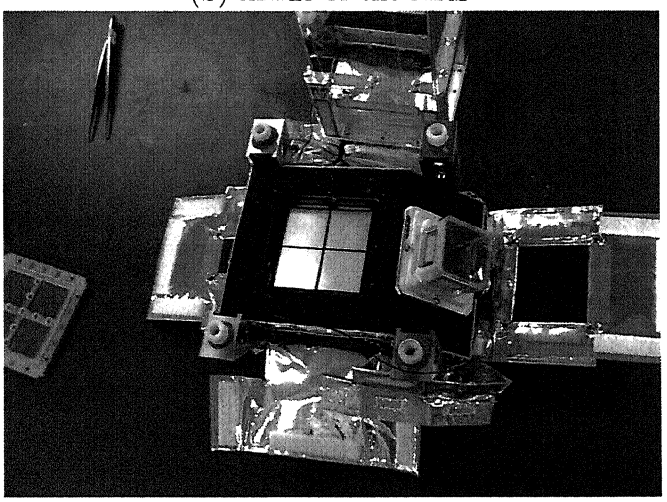

Figure 3.1: X-ray fluorescence spectrometer onboard Hayabusa. The asteroid detector, with arrays of four CCDs (CCD#0, 1, 2, and 3), observes X-ray photons from X-ray sources and Itokawa, while other single CCD (CCD#4) observes X-rays from an onboard standard sample.

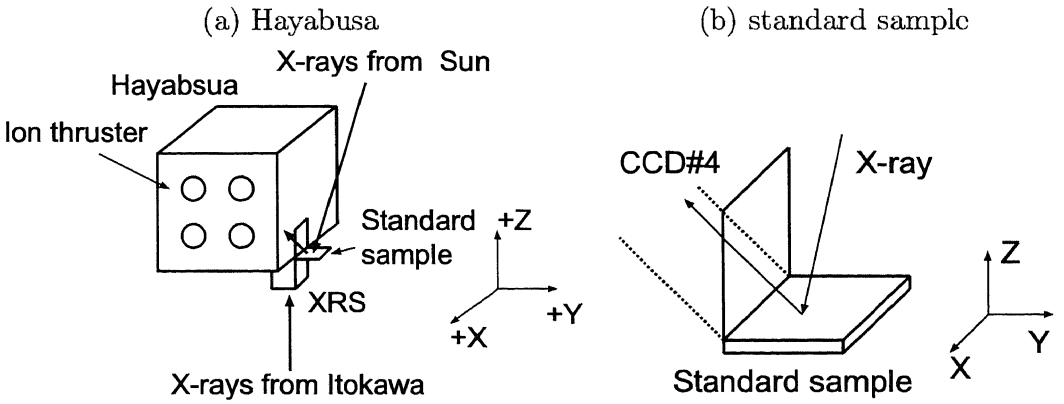

Figure 3.2: The Hayabusa coordinate system. In order to estimate the solar X-rays, it is necessary to illuminate sun light to the standard sample.

Table 3.1: The elemental composition of the standard sample (wt.%).

element	standard sample
H	-
C	-
O	40.80
Na	2.30
Mg	8.70
Al	5.20
Si	19.70
P	-
S	~0.0
K	0.35
Ca	5.00
Ti	0.60
Cr	0.35
Mn	0.35
Fe	16.00
Co	0.35
Ni	0.70
total	100.4

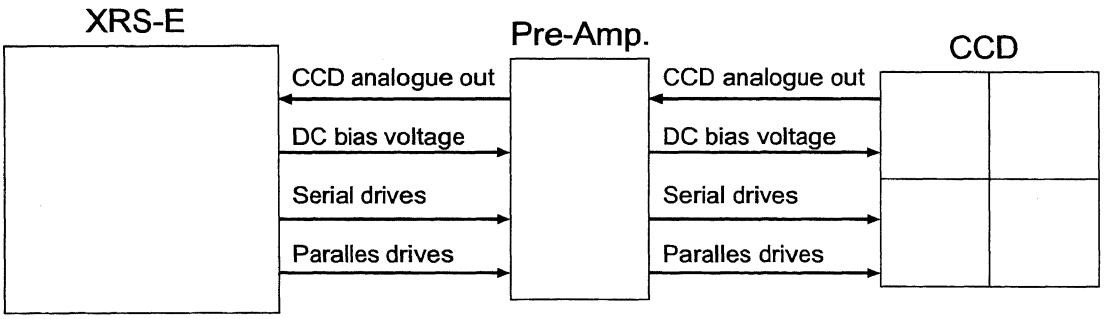

Figure 3.3: Electronics–Pre-amplifier–CCD relation. Electronics (XRS-E) supplies the voltages and drive clocks to CCD. Also, the electronics perform a telemetry and command interface, power supply, data acquisition, data handling, and onboard analysis.

3.2 Characteristics of charge coupled devices

Charge coupled-devices (CCDs) are used for the XRS as a main sensor (Deep-1) (*e.g.*, Miyata *et al.*, 1999). It is a full frame transfer CCD in order to achieve a large effective area in spite of its small size. It does not contain a trigger and data stored area. A P-N semiconductor is undergone a negative-bias that makes a depletion layer, where X-rays are trapped. Each pixel is Si-semiconductor, where potential changes with clock pulse which drives charges as shown in Figure 3.4, where DN means a digital number generated by an analog-to-digital converter for each pixel. The XRS usually performs with vertical a 16 line binning transfer mode for fast readout. where charges are effectively transferred in vertical 64 pixels and horizontal 1024 pixels in active detection area. The CCD includes imaginary regions, called vertical and horizontal over-clocked region, in vertical and horizontal as schematically shown in Figure 3.5. More detail specifications are shown in Table 3.2.

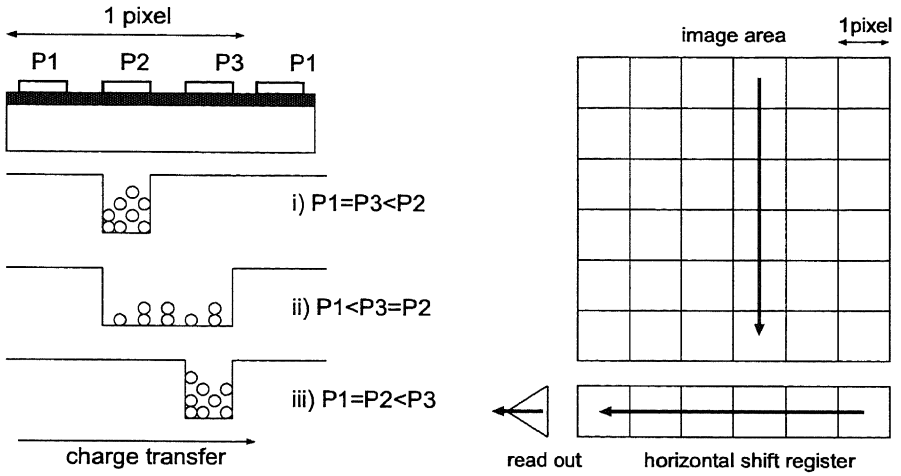

Figure 3.4: Schematic diagram of CCD charge transfer. Clock pulse carries charges, where P1, P2, and P3 indicate clock voltages. Charges are carried step i) to step iii) with a clock pulse. The CCD performs with the transfer of vertical 64 pixels, followed by that of horizontal 1024 pixels.

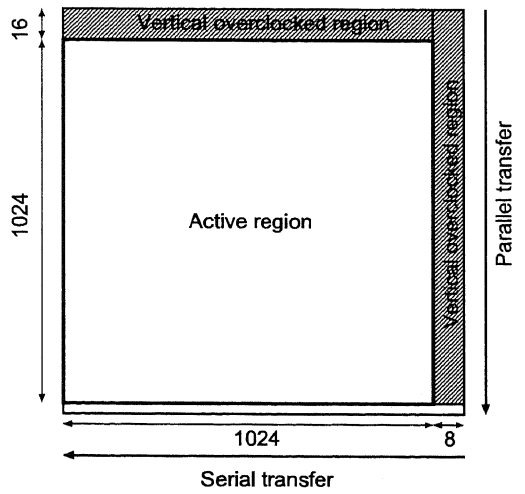

Figure 3.5: Effective and over-clocked regions of CCD. The values indicate the number of pixels. The CCD includes imaginary regions called vertical and horizontal over-clocked regions.

Table 3.2: Specifications and performances of CCD

CCD (Deep-1 type)	
Fabrication	Hamamatsu photonics
Effective pixels	1024×1024pixels
Size of pixels	24μm×24μm
Transfer	full-frame transfer
Package shape	3-side Buttable
others	TEC(δT=40°C @ 1W in vacuum)
Fill factor	100%
Full well capacity	300 K e- (standard)
Dark current	2-4e-/pixel/s at -20 degrees Celsius
CCD node sensitivity	2.7 μV/e-
Readout noise	5-8e-rms
Package	Ceramic package with TEC
Dead space	Horizontal < 500 μm (each CCD chip)
	Vertical < 150 μm (each CCD chip)
Flatness	Not guaranteed
Pixel alignment	Less than 1 pixel
Structure	Aluminum light shield 200nm
	Temperature sensor (MOSFET)
	Options: thin dead layer, thin gate

3.2.1 Split events

X-ray events produce electron charges that are ideally included in a single pixel but often intrude neighboring pixels, which is called "split events" (see also Figure 3.8). It disperses some pixels and causes the degradation of detection efficiency and energy resolution, and thus only single pixels are extracted in onboard reduction of XRS.

3.2.2 Pile-up phenomena

Those events where more than two X-ray photons irradiate into a pixel are called "pile-up". The probability of pile up is represented by Poisson distribution P as follows,

$$P_\mu(n) = \frac{\mu^n}{n!}\exp(-\mu),$$

where μ is a mean count of X-ray photons for one pixel and n is counts of incident photons. Since the XRS performs with a vertical 16 binning mode, pile-up feared pixels are 16 times as large as those of 1 binning mode. Also, the pile-up of split events in neighboring pixels of the event pixel is necessary to avoid. Thus, the number of net pile-up feared pixels is 3×16 = 48 pixels as schematically shown in Figure 3.6, and then the pile up probability is written as follows,

$$P_{\rm pileup} = 1 - \frac{P_\mu(1)\times P_\mu(0)^{47}}{P_\mu(1)\times 1^{47}} = 1 - \exp(-47\mu).$$

If the probability of pile-up keeps less than 1%, it the following relationship is needed,

$$\exp(-47\mu) \geq 0.99.$$

Hence, for 1% pile-up count rate,

$$\mu \leq 2.14 \times 10^{-4} \quad \text{(photons/pixel/frame)},$$

$$\textit{also}, 1024 \times 1024 \times 2.14 \times 10^{-4} \sim 225 \quad \text{(photons/frame)}$$

i.e., XRS can detect the events of 225 (events/sec/frame) without pile-up.

3.2.3 Read-out noise

Read out noise is the total analog noise of an electric circuit, given by the standard deviation of the horizontal overclocked region $\Delta \mathrm{PH_{HOC}}$ as a function of pulse height as follows,

$$\text{read out noise} = \Delta \mathrm{PH_{HOC}} \times \frac{\text{gain}}{w}.$$

where w is the mean ionization energy of Si ($\sim$ 3.65 eV), and gain represents the energy to channel conversion factor. It affects the performance of energy resolution of XRS. XRS usually operates int the fast read out mode, binned vertical 16 pixels, in order to achieve high energy resolution.

3.2.4 Transfer noise

The transfer noise, produced during charge transfer, is defined as the difference between the Gaussian peak-center of standard deviation of vertical pixel values $\Delta \mathrm{PH_{VOC}}$ and that of horizontal pixel values $\Delta \mathrm{PH_{HOC}}$ as follows,

$$\text{transfer noise} = \left(\bar{\mathrm{PH}}_{\mathrm{VOC}} - \bar{\mathrm{PH}}_{\mathrm{HOC}}\right) \times \frac{\text{gain}}{w}.$$

The transfer noise also affects the performance of energy resolution of XRS, and shifted position of peak center of line spectrum.

3.2.5 Dark current

Carriers are thermally generated under totally dark conditions. The dark currents are defined as average levels of pulse heights, including that of totally dark level. The energy resolution of XRS depends on the dark current, and thus the performance of XRS is better in cooled condition. XRS usually performs fast readout (16 binning mode) in order to reduce the dark current.

3.2.6 Charge transfer efficiency

Charge transfer efficiency is defined as that the fraction of charge successfully transferred for pixel transfer as follows,

$$\mathrm{CTE} = 1 - \frac{\text{lost charge}}{\text{total charge}} \times \frac{1}{n},$$

where n is the number of transfer times. It also affected the performance of energy resolution of XRS, and shifted position of peak center of line spectrum.

3.2.7 Hot pixels

Carrier carries electrons from electrode to depletion layer due to degradation of insulation by space irradiation damage. In serial and parallel transfer of carrier, many carriers are charged from electrode cause high charged called hot pixels. They usually produce a high output, and then most of hot-pixels are subtracted by onboard reduction. However, some hot pixels randomly generate carrier called white damage or vacuum carrier called black damage. They can not be reduced in the observation spectra.

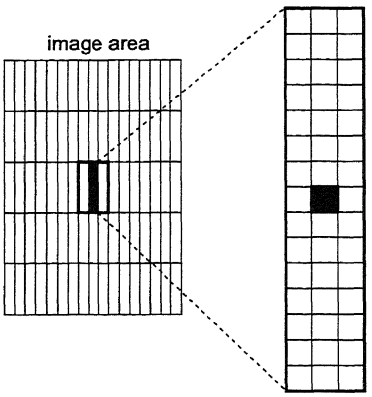

Figure 3.6: The probability of pile-up is calculated with Poisson distribution. Since the XRS operates in the vertical 16 binning mode, the number of pile-up feared pixels is 3×16 pixels.

3.3 Overview of onboard data reduction

XRS performs onboard data reductions by a combined process of hardware and software. The hardware process extracts X-ray events, and the software process makes the histogram (spectral data). The extraction events has the value of exceeding event threshold from background level (usually 60 channels $\sim$ 600 eV) in the unit of pulse heights. The background is calculated as follows,

$$\bar{B}_{xy}^{\rm new} = \bar{B}_{xy}^{\rm old} + \frac{B_{xy}^{\rm now} - \bar{B}_{xy}^{\rm old}}{h},$$

where h is a history parameter (=4) which proportional to a convergence time for background update. Figure 3.7 shows a schematic view of event extraction and histogram making, where XRS extracts only the event exceeding the event threshold level, set by command.

The split events decrease the energy resolution and thus the onboard software reduces the split events as shown in Figure 3.8. The grade classifications for the XRS are defined as follow: Grade-0: single pixel event, Grade-1: left split event, Grade-2: right split event, and Grade-3: left and right split events. Thus, only the grade-0 events are integrated in the spectrum. The XRS extracts only grade-0 events and makes a histogram.

Observation data as histogram are usually integrated every 300 seconds, and then background update times are 60 seconds. There has a dead-time every integration interval. Also, XRS reduced the data amount by using Huffman compression with software control (Yamamoto, 2002). XRS data usually obtains the data of 7 packets *i.e.*, 5 CCDs packets and 2 status packets which require the maximum amount of 7168 Bytes.

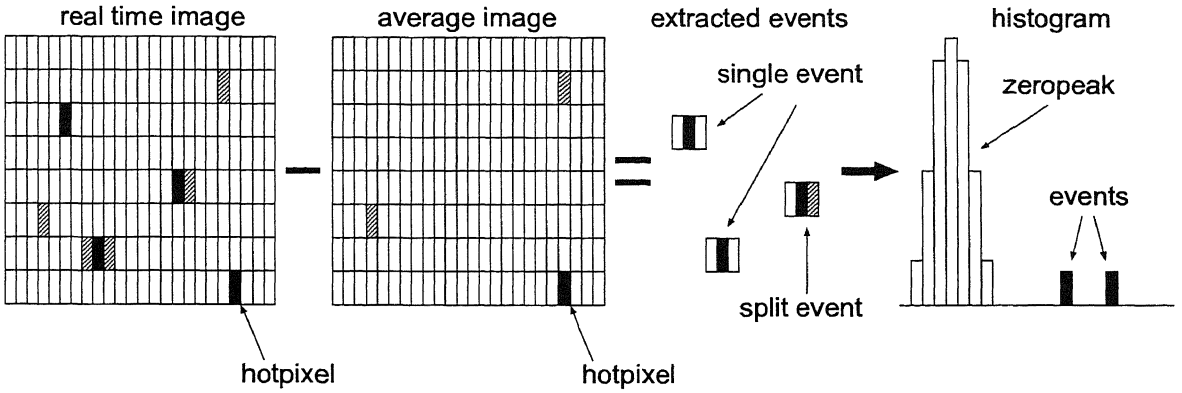

Figure 3.7: Schematic view of onboard histogram making. The XRS makes a histogram (X-ray spectrum). XRS makes a background image and subtract it from the real time image. The XRS makes a histogram with only grade-0 events (single pixel events).

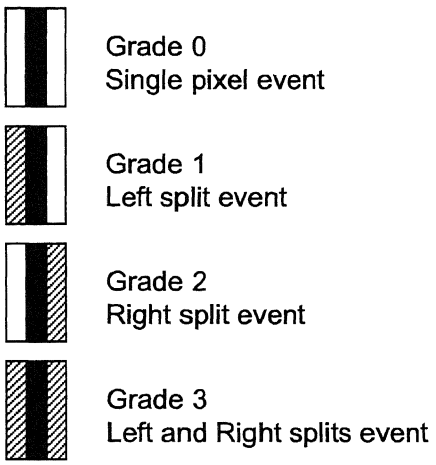

Figure 3.8: Definition of grade classification for the XRS. Grade-0: single pixel event. Grade-1: left split event. Grade-2: right split event. Grade-3: left and right splits event.

Chapter 4

X-ray Models

In this chapter, X-ray models, used in our analysis, are described for solar X-rays, and for fluorescent and scattering X-rays emitted from the planetary surface.

4.1 Overview of X-ray interactions in planetary surface

The XRS observes both fluorescent and scattering X-rays from the surface materials of Itokawa and X-rays from the onboard standard sample, excited by incident solar X-rays. The intensities of fluorescent and scattering X-rays depend on model parameters, such as emission measure as plasma density and size, and plasma temperature of the solar coronal region. Fluorescent X-rays have line spectra whose intensities are proportional to elemental abundance. Scattering X-rays are either a coherent or incoherent scatter of solar X-rays, composed of line spectra representing characteristics of ions in plasmas and continuum spectrum representing thermal bremsstrahlung emission. In order to determine the elemental abundance, it is necessary to quantitatively estimate the fluorescent X-rays and to separate the fluorescent and scattering X-rays from observed spectrum. Hence, precise X-ray models for solar X-rays, and for fluorescent X-rays and scattering X-rays are required.

4.2 Model of solar X-rays

Solar X-ray models have been formulated by Raymond and Smith (1977) and Mewe *et al.* (1985). Solar X-ray model spectrum J is expressed by plasma temperature T and emission-measure ϵ for thermal bremsstrahlung as follows,

$$J(E,T,\epsilon) = k\bar{G}\frac{\sqrt{T}}{E}\epsilon \exp\left(-\frac{11.6E}{T}\right),$$

where k is a proportional constant, and $\bar{G}$ is a gaunt factor, including free-free transitions (bremsstrahlung), free-bound transitions (radiative recombination) and two-photon decay of measurable 2s states of hydrogen and helium like ions.

Here, the MEKAL (Mewe-Kaastra-Liedahl) model (Arnaud *et al.*, 2005), which represents solar X-rays well in the hard energy range, is used for analysis in this study. The solar abundance assumed in this model was taken from Anders and Grevesse (1989). Examples of the MEKAL model spectra with different emission-measures and temperatures are shown in Figure 4.1, where plasma temperatures are 4, 8, and 16 MK (http://www.swpc.noaa.gov/).

The solar X-ray flux levels are defined by GOES X-ray flux levels as shown in Table 4.1. That the solar X-ray fluxes are proportional to plasma temperatures have been studied by

Feldman *et al.*, (1996) as shown in Figure 4.2. These relations can be expressed by log-liner curves as follows,

$$\begin{aligned} f_{\rm long} &= 3.5 \times 10^{0.185T_e - 9.0} \quad (1.55 - 12.40{\rm keV}), \\ f_{\rm short} &= 1.1 \times 10^{0.263T_e - 10.0} \quad (3.10 - 24.80{\rm keV}), \end{aligned} \tag{4.1}$$

where $f_{\rm long}$ is the flux in the energy range from 1.55 to 12.40 keV, $f_{\rm short}$ is also the flux in the energy range from 3.10 to 24.80 keV, and T_e is the plasma temperature for He-like lines of Fe, Ca, and S. These equations are used for initial values of model fitting in analysis of the observed Itokawa spectra.

Recently, new solar X-ray models are developing such as the CHIANTI model. The CHIANTI model well represents the lower energy spectrum of Solar X-rays (less than 2 keV). For X-ray spectrometer onboard NEAR-Shoemaker, a blend of the CHIANTI and MEKAL models has been used (Lim *et al.*, 2006). In contrast, blend models of two MEKAL spectra were used in the analysis for this study because observed data of the XRS cannot resolve the CHIANTI and MEKAL spectra. However, more accurate solar X-ray models should be used in the future missions.

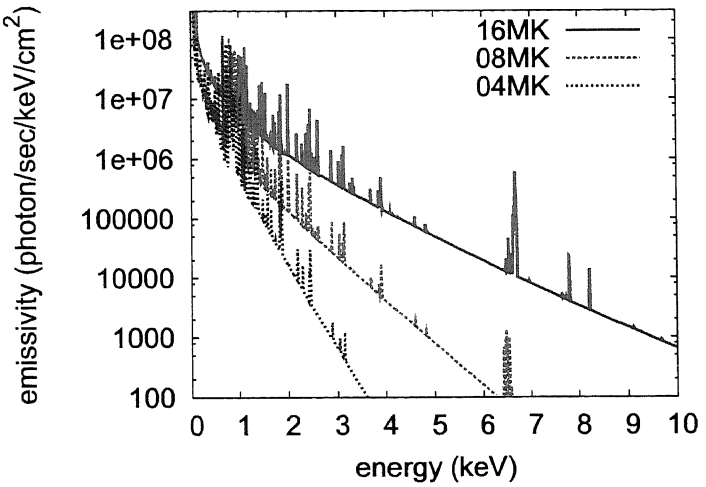

Figure 4.1: Examples of solar X-ray models calculated by using MEKAL models, where plasma temperatures are 4, 8, and 16 MK, and fluxes are normalized as M1:10^{-5}Watts/m^2, C1:10^{-6}Watts/m^2, B1:10^{-7}Watts/m^2.

Table 4.1: GOES X-ray flux level.

flare level	flux in 1–8 $\AA$
A1	10^{-8} Watts/m^2
B1	10^{-7} Watts/m^2
C1	10^{-6} Watts/m^2
M1	10^{-5} Watts/m^2
X1	10^{-4} Watts/m^2

(a) Emission measure *vs.* Temperature

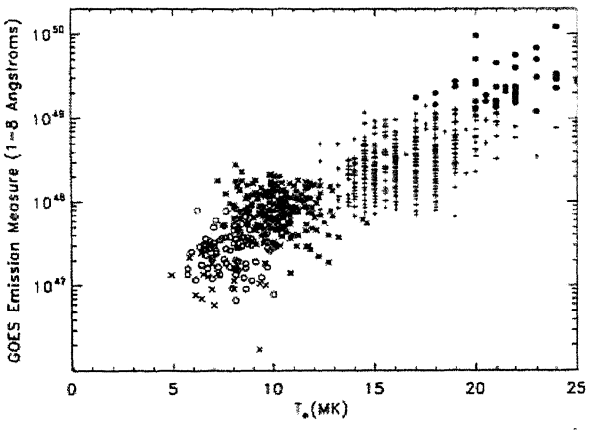

(b) X-ray flux *vs.* Temperature

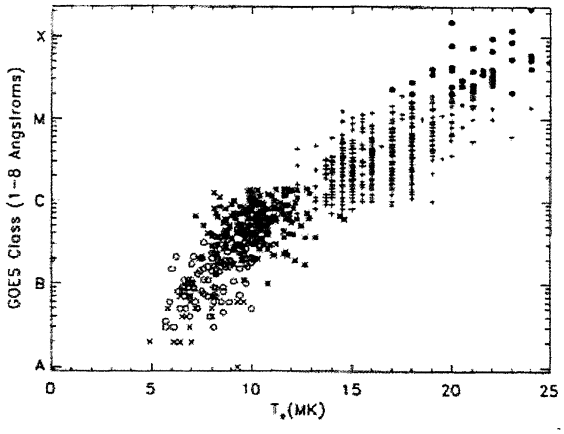

Figure 4.2: (a) Relation between the emission measure and plasma temperature, obtained from Feldman *et al.* (1996). (b) Relation between GOES X-ray flux and plasma temperature, obtained from Feldman *et al.* (1996). These relations are used for estimation of initial values for model fitting in analysis of observed spectra of Itokawa.

4.3 Matrix effect on materials

In this study, rocky materials, composed of many elements, are considered as the target objects. When X-rays are attenuated in the objects, attenuation ratios vary for each element in the ratios of elemental mass fraction w_i for element i. In order to correct this effect, the attenuation coefficients $\mu_i(E)$ for a single element in Equation 2.1 is rewritten as a sum of many elements using the ratios of elemental mass fraction as follows,

$$\mu_i(E) \rightarrow \sum_j w_j \mu_j(E). \tag{4.2}$$

This replacement is called a matrix effect.

4.4 Model of fluorescent X-rays

Fluorescent X-rays of an element are proportional to elemental mass fraction of the element in materials. The X-ray fluorescence model was previously described in Chapter 2. Here, the model is rewritten as follows,

$$I^f(E_i^f) = \frac{\Omega S}{4\pi} \int \frac{\omega_i p_i j_i t_i w_i \tau_i(E) J(E)}{\sum_j w_j \mu_j(E) + \sum_j w_j \mu_j(E_i^f) \frac{\cos\phi_1}{\cos\phi_2}} dE, \tag{4.3}$$

where Ω is a field of view of the XRS (observation area divided by altitude squared), S is an effective area of the XRS (1 inch^2 for CCD), ω_i is an X-ray fluorescence yield which is K or L α line emission yield (Krause, 1979), p_i is a ratio of α or β line emission (we used an empirical value: α:β=15:2), j_i is a jump ratio which is K or L shell absorption ratio (Chantler *et al.*, 2005), s_i is a ratio of shell transition probability, τ is a mass absorption coefficient as a function of energy (Chantler *et al.*, 2005), μ is a mass attenuation coefficient as a function of energy (Chantler *et al.*, 2005), E^f is a X-ray fluorescence line energy (Bearden, 1967), ϕ_1 and ϕ_2 are incident solar X-rays angle and emission fluorescent X-rays angle, respectively, and J is

an intensity of solar X-rays as a function of energy. The integration interval is from the edge energy to ∞. Also, L line emissions (L_1, L_2, and L_3) are derived from the exchange of jump ratios from $(r_z^K - 1)/r_z^K$ to $(r_z^L - 1)/(r_z^K r_z^L)$, which are good approximations, and the exchange of the integration interval from $[E_z^{K_{deg}}, E^{max}]$ to $[E_z^{L_{deg}}, E^{max}]$. This equation is used for the model fitting in the analysis of the observed spectra of Itokawa.

Furthermore, secondary-fluorescent X-rays, excited by primary fluorescent X-rays in near layers, have been formulated by Shiraiwa and Fujino (1966).

4.5 Model of scattering X-rays

Scattering of solar X-rays is expressed by a coherent scattering and incoherent scattering. Incoherent scattering, which is the Compton scattering, is not effective in the observable energy range from 0.7 to 10.0 keV for the XRS. Thus, incoherent scattering is neglected in this study.

Here, coherent scattering is described. Cross section of the Rayleigh scattering (the Thomson scattering) σ is written as follows,

$$d\sigma = \frac{1}{2}\left(\frac{e^2}{mc^2}\right)^2 (1 + \cos\theta) d\omega,$$

where m is a mass of target, c is a light speed, and e is en elementary electric charge. The model of scattering X-ray spectrum is a continuum emission I^s for element i. Rayleigh scattering of solar X-rays (*e.g.*, Thomson *et al.* 1906; Clark and Trombka, 1997) is written as follows,

$$I^s(E) = \Omega S \frac{\sum_i w_i \left(\frac{N_A}{M_i} r_e^2 \frac{1+\cos^2\theta}{2} f_i^2\right) J(E)}{\sum_i w_i \mu_i(E) \left(1 + \frac{\cos\phi_1}{\cos\phi_2}\right)}, \tag{4.4}$$

where N_A is the Avogadro constant of 6.02×10^{23} mol^{-1}, r_e is the classical electron radius of 2.82×10^{-13} cm, θ is a back scatter angle of θ=180°-(ϕ_1+ϕ_2), M_i is an atomic weight for element i (Chantler *et al.*, 2005), and f_i is the atomic scattering factor for element i (Maslen *et al.*, 2004) as a function of scattering angle. Furthermore, secondary-scattering X-rays, excited by primary scattering X-rays in near layers, are written in the same was as for the formula of secondary fluorescent X-rays (Shiraiwa and Fujino, 1966).

4.6 Effect of surface geometry

The surface geometry in Itokawa varied for every observed area, therefore X-ray incident and emission angles also varied. The X-ray angles at each area can be calculated by using the shape model of Itokawa (*e.g.*, Gaskell *et al.*, 2006; Demura *et al.*, 2006). Figure 4.3 shows a shape model of Itokawa (the Aizu 5.02 model (Demura *et al.*, 2006)). X-ray emissions with the shape model in sunlit areas should be calculated, where the X-ray incident angle ϕ_1 and emission angle ϕ_2 in Equations 4.3 and 4.4 are calculated by using the normal vectors of polygon faces and the angle of the Sun. Also, the field of view should be calculated, and then Ω in Equations 4.3 and 4.4 for polygon faces are rewritten as follows,

$$\Omega \rightarrow \frac{s_i}{d_i^2},$$

where s_i is an area for polygon face i and d_i is a distance between the ith face and the XRS. The size of the polygon face s_i is of the order of meters, which is much smaller than the observed area. Roughness of smaller scale than polygon faces is neglected.

Figure 4.4 shows schematic views of the observation for the standard sample and for Itokawa (X-ray models are indicated in parentheses). The standard sample observation and the Itokawa observations are simultaneously performed in all observation period. The CCD#4 observes the X-rays from the standard sample excited by incident solar X-rays. CCD#0, 1, 2, and 3 observe X-rays from the surface materials of Itokawa excited by the same incident solar X-rays. The geometry of observation area in the surface of Itokawa varies at local areas. Therefore, the incident and emission X-ray angles for the surface with the shape model of Itokawa (Demura *et al.*, 2006) should be calculated.

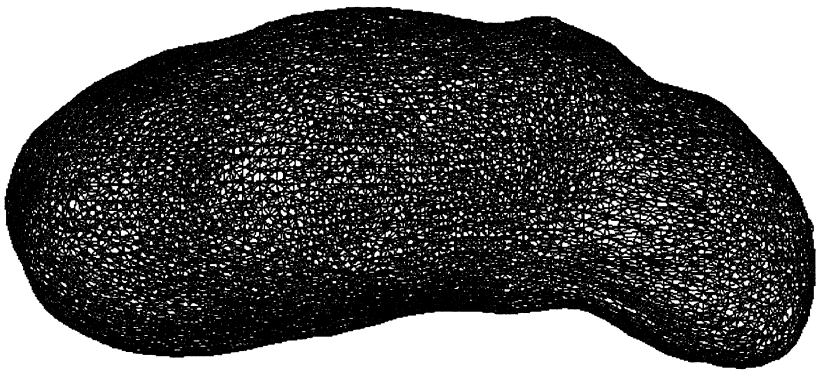

Figure 4.3: **The shape model of Itokawa (Demura *et al.*, 2006). X-ray incident angle ϕ_1 and emission angle ϕ_2 are calculated by using this shape model. The size of the polygon faces is of the order of meters which is much smaller than the observed area of the XRS.**

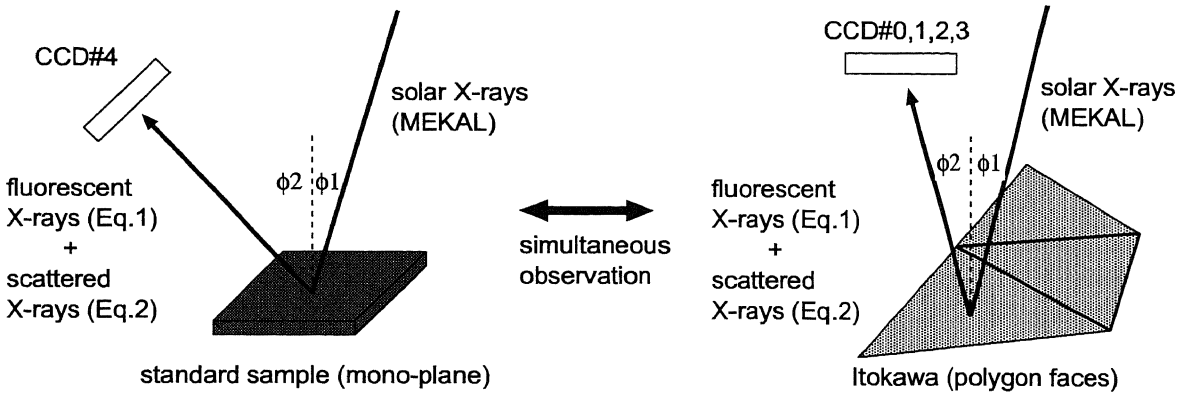

Figure 4.4: **Schematic views of the observation for the standard sample and Itokawa (X-ray models are indicated in parentheses). The standard sample observation and the Itokawa observation are carried out simultaneously in all observations. The CCD#4 (solar monitor) observes the X-rays from the standard sample excited by incident solar X-rays. CCD#0, 1, 2, and 3 observe X-rays from the surface materials of Itokawa excited by the same incident solar X-rays. The geometry of observation area in the surface of Itokawa varies at local areas and thus incident and emission X-ray angles for the surface are calculated with shape model of Itokawa (Demura *et al.*, 2006).**

4.7 Examples of anticipated spectra

Examples of the calculated X-ray spectral models are shown in Figures 4.5a and 4.5b. These examples are for X-ray emissions from the standard sample and from ordinary chondrites analogues. They are composed of the line spectra of fluorescent X-rays and the continuum spectrum of scattering X-rays. Major fluorescent X-rays are found in the energy peaks of O-Kα (0.52 keV), Mg-Kα (1.25 keV), Al-Kα (1.49 keV), Si-Kα (1.74 keV), S-Kα (2.31 keV), Ca-Kα/β (3.69 keV / 4.01 keV), and Fe-Kα/β (6.40 keV / 7.06 keV).

(a) X-rays from standard sample

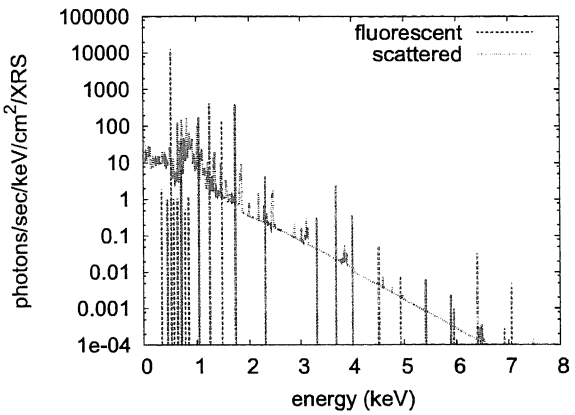

(b) X-rays from Ordinary chondrites

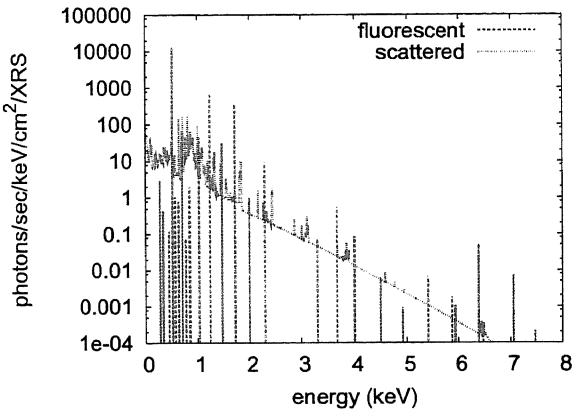

Figure 4.5: Examples of the calculated X-ray spectral models with MEKAL models and Equations 4.3 and 4.4 are shown in these figures. (a) The example of model spectra of X-ray emission from standard sample. It contains the line spectra of fluorescent X-rays and continuum spectrum of scattering X-rays. Major peaks are found such as O-Kα (0.52 keV), Mg-Kα (1.25 keV), Al-Kα (1.49 keV), Si-Kα (1.74 keV), S-Kα (2.31 keV), Ca-Kα/β (3.69 keV / 4.01 keV), and Fe-Kα/β (6.40 keV / 7.06 keV). (b) The example of model spectra of X-ray emission from ordinary chondrites-analogues. Same energy lines are found as same as (a).

Chapter 5

Performance of the XRS in Pre-launch Tests

In this chapter, the sensor characteristics of the XRS examined in the laboratory at the time of the pre-launch test are described.

5.1 Overview of sensor characteristics of the XRS

Observation spectra $O(PH)$ as a function of pulse height are convolution of $I(E)$ with the sensor characteristics of the XRS $R(PH)$ as follows,

$$O(PH) = I(E) \otimes R(PH, E),$$

where $I(E)$ is X-rays incident to the XRS emitted from a target, and $\otimes$ indicates a convolution. The equation is deconvoluted by a least squares-fit method. Since $R(PH, E)$ includes many functions such as a response function, detection efficiency and grade ratios, it needs to be measured in laboratory experiments. When the XRS observed Itokawa, the temperature of CCD was controlled in the range of -52±2 degrees Celsius. Therefore, sensor characteristics for the analysis of Itokawa data should be measured in similar configuration. In this study, the response model for the XRS is constructed by using the data set measured at -53±1 degrees Celsius in the laboratory experiments.

5.2 Measurement of response functions

It is necessary to improve the response model of the XRS easily and flexibly for historical changes. The response model for CCD has been constructed for SIS onboard ASCA, considering physical process of photon attenuation and absorption within the CCD gate structure. It represented the response model as the sum of two Gaussians and a constant called a double Gaussian model. Recently, response models of XIS onboard ASTRO-E has been constructed as a sum of 6 functions that is, main peak, sub peak, triangle, Si K-escape, Si fluorescence line, and a constant component (*e.g.*, Katayama et al., 2000; Imanishi *et al.*, 2000). However, these response functions do not fit the response of the XRS. It is necessary to construct the original response model for the XRS.

In these experiments, the XRS measured fluorescent X-rays from the Oxide target, and then bremsstrahlung and scattering X-rays from the X-ray tube were filtered with the Be window of sample chamber as schematically shown in Figure 5.1. In order to determine the sensor characteristics of the XRS, X-ray line emissions were measured from powdered samples such

as, MgO: Mg-Kα(1.25 keV), Al_2O_3: Al-Kα(1.49 keV), SiO_2: Si-Kα(1.74 keV), $CaCO_3$ Ca-Kα/β(3.69/4.01 keV), TiO_2 Ti-Kα/β(4.51/4.93 keV), and Fe_2O_3 Fe-Kα/β(6.40/7.06 keV), in vacuum chamber ($<10^{-5}$ Torr), and then the temperature was lowered by liquid deposit and heater power to -53±1 degrees Celsius. An X-ray generator with the X-ray tube of Cr target was used, where acceleration voltage was 20 kV. At this voltage, scattering and bremsstrahlung X-rays, shielded by the Be window of the sample chamber, were not prominent in a current of 2 to 20 mA, and thus they were neglected. Figure 5.1 shows the configuration of this experiment.

The gate structure of CCD was assumed to be composed of thin layers, such as Aluminum coat, Silicon oxide insulator and poly-Silicon gate, depletion-layer, and neutral region. Electron clouds, generated by photo-electric effect, diffuse forward toward an electrode along the electric field in the depletion layer and then they are converted to X-ray signals. However, the some portions of electrons cause split events. Thus, the response function of the XRS composed of four functions was constructed such as main-peak, Si K-escape, Si fluorescence line, and continuum component.

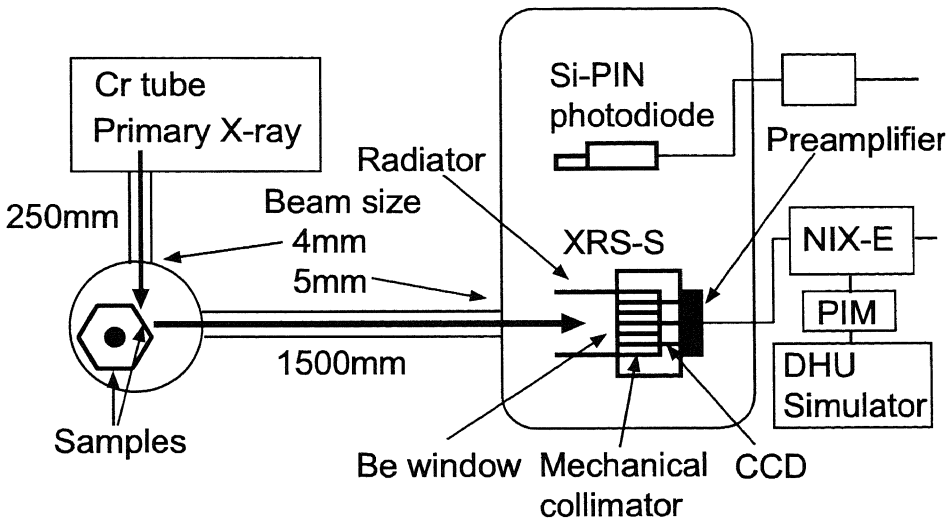

Figure 5.1: Configuration of experimental setup. The XRS was installed in the vacuum chamber (less than 10^{-5} Torr), and then the electric circuit (NIX-E) and data handling simulator (DHU) were set in out of chamber. The CCDs temperatures were the value of -53±1 degrees Celsius. Primary X-rays from Cr tube excited the powdered samples of MgO, Al_2O_3, SiO_2, $CaCO_3$, TiO2, or Fe_2O_3 on the sample holders. X-ray Fluorescence lines were detected with the XRS, and then bremsstrahlung and scattering X-ray were filtered with Be window of sample chamber. Also, same X-rays were measured by Si-PIN photo-diode as reference.

5.2.1 Main peak

When incident X-rays are trapped in the effective region of the depletion layer, an electron cloud is generated by photo electric effects. The spectral response is expressed by a Gaussian as follows,

$$\mathrm{F}_{ij}^{1} = N_j^1 \frac{1}{\sqrt{2\pi s_j^2}} \exp\left(-\frac{(c_i - c_j)^2}{2s_j^2}\right),$$

where indexes i and j indicate an energy interval for bins, N_i^1 is an intensity of the main peak, c_i is a center of peak as expressed by a pulse height, and s_i is standard deviation. Then s_i is a

function of read-out noise n (e^-) and energy as follows,

$$s_i(E) = w_{\rm Si}\sqrt{n^2 + \frac{F}{w_{\rm Si}}E},$$

where F is the Fano factor representing the difference from Poisson distribution (*e.g.*, Knoll, 1999), $w_{\rm Si}$ (eV/electron) is an Si mean ionization energy for an electron-hole pair, and n is a read-out noise. Here, a conversion factor from pulse height to energy is written as linear function as follows,

$$c_i = \text{gain} \times e_i + \text{offset},$$

where offset means a correction factor then a full width half maximum (FWHM) Δ as energy resolution is written as follows,

$$\Delta_i = s_i \times \sqrt{8\log(2)}.$$

Figure 5.2 shows the anticipated energy resolution Δ *vs.* energy, where the read-out noise was assumed to be 18 e^-.

Free parameters for the main peak Gaussian are intensity, peak center, standard deviation, gain, and offset. The Fano factor and Si-mean ionization energy are constants of Si-semiconductor, respectively, f^{Fno} was assumed to be 0.12, $w^{\rm Si}$ was assumed to be 3.65 eV/electron.

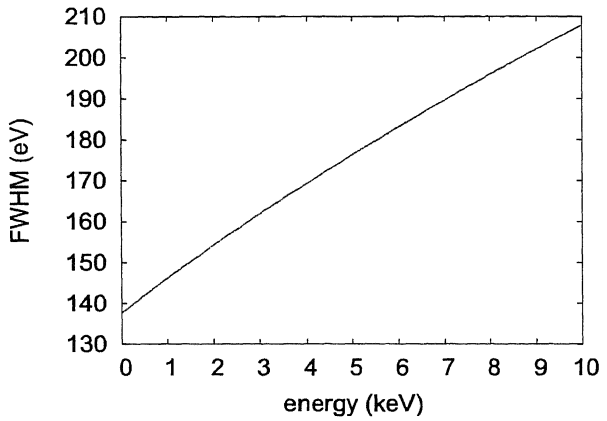

Figure 5.2: Anticipated Energy resolution (FWHM)

5.2.2 Continuum component

When an incident X-ray is trapped in the deep neutral region, generated electron clouds diffuse too many pixels. The response makes an approximately continuum spectrum. Since the response of the XRS includes split events, the intensity of response curve $N_i^{\rm cons}$ for element i was written approximately as a second order function as follows,

$$\begin{aligned} N_i^{\rm cons} &= N_i^{\rm main} \times \frac{-1.0}{(E-(3.0E_{\rm SPLTH})/g)(E-E_i)} && (3\sigma/g < E < E_i - 3\sigma/g) \\ N_i^{\rm cons} &= 0 && (E < 3\sigma/g \;\&\; E > E_i - 3\sigma/g), \end{aligned} \tag{5.1}$$

where g is a gain, $E_{\rm SPLTH}$ is a value of split threshold (60 channels), and σ is a standard deviation. Figure 5.3 shows the best-fit intensity of continuum spectrum divided by that of main-peak by using Equation 5.1.

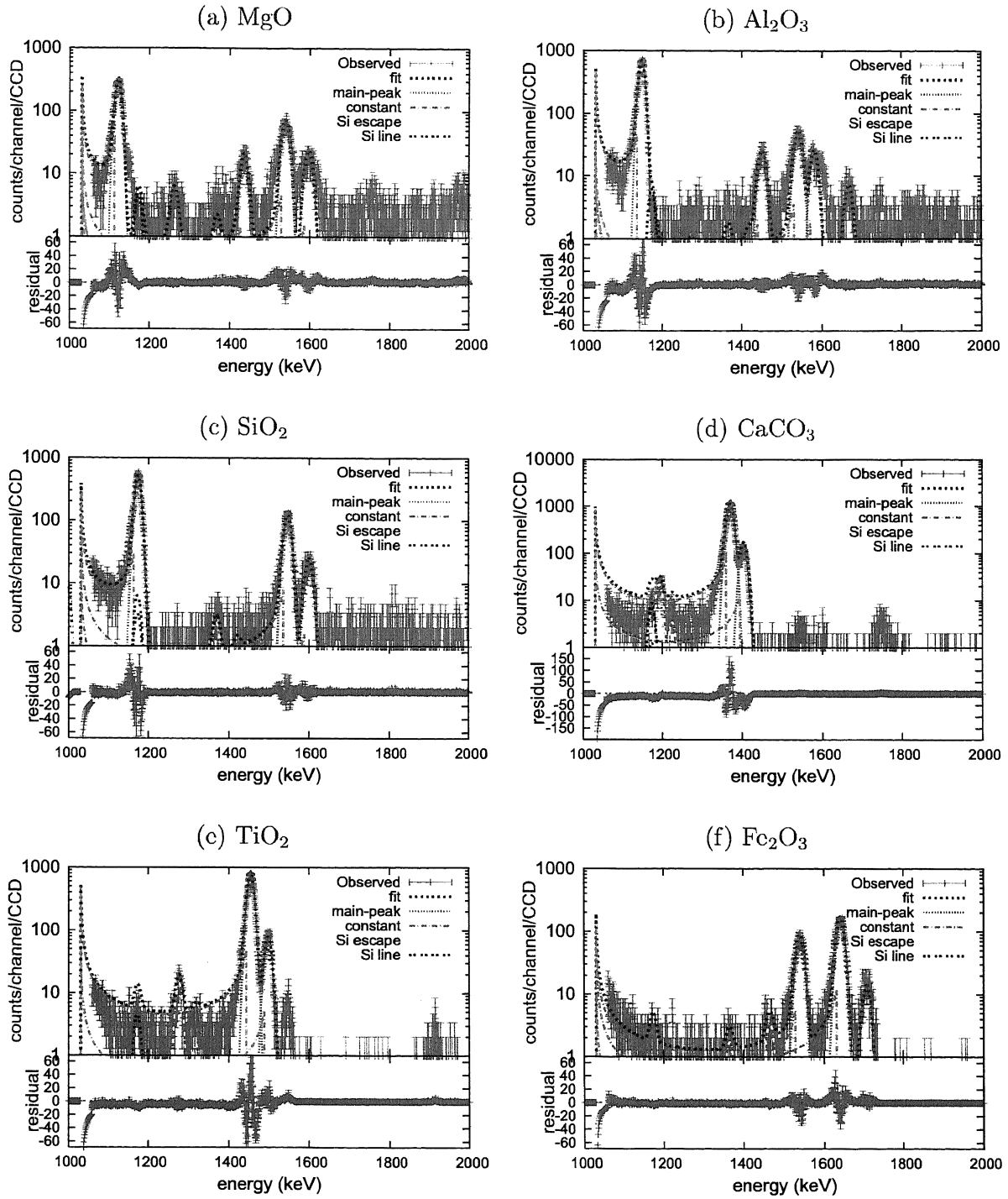

Figure 5.3: Best-fit response functions to observed spectra for (a) Mg-Kα (1.25 keV), (b) Al-Kα (1.49 keV), (c) Si-Kα (1.74 keV), (d) Ca-Kα/β (3.69/4.01 keV), (e) Ti-Kα/β (4.51/4.93 keV), Cr-Kα/β (5.41/5.95 keV), and (f) Fe-Kα/β (6.40/7.06 keV). The response function of the XRS was assumed to be composed of four functions, such as main-peak, Si K-escape, Si fluorescence line, and continuum component.

5.2.3 Construction of response function

The incident X-rays are convolved with sensor characteristics as a response function, leading to a matrix equation as schematically shown in Figure 5.4. The response matrix is given as a sum of response functions as follows,

$$R_{ij} = \sum_k F_{ij}^k,$$

where i, j = 1,2,3,$\cdots$,4096 channels (12 bits), k is an index of response function. Here, the response for the XRS is assumed to be a sum of four functions such as, main peak Gaussian F_{ij}^1, continuum component F_{ij}^2, Si-escape F_{ij}^3 and Si-line F_{ij}^4. The values of the Si-escape and Si-line were obtained from Nishiuchi (1998).

In order to construct the response for all energy ranges, observed results of continuum component were complemented by a power-law model,

$$\frac{N_i^2}{N_i^1} = a \times {c_i}^b,$$

where a is a proportional coefficient and b is an index. Figure 5.5 shows the best-fit power-law model to the intensities of continuum component normalized by the intensities of the main peak. Also, Table 5.1 shows this result.

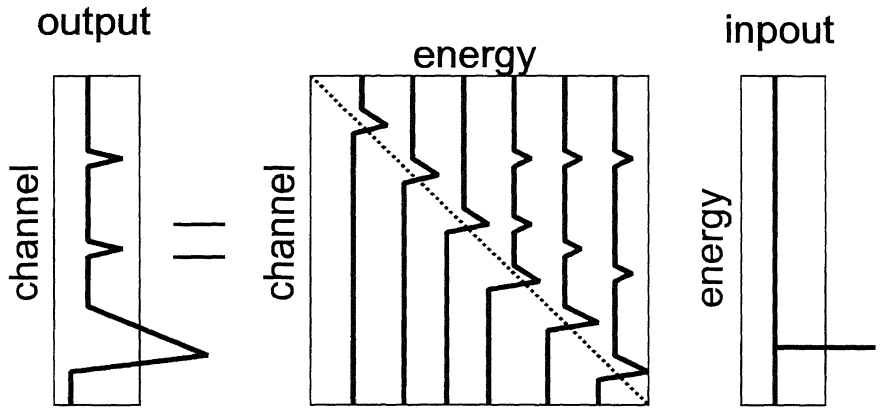

Figure 5.4: Response matrix. Incident X-rays from target are convolved with the sensor characteristics as response function, leading to a matrix equation.

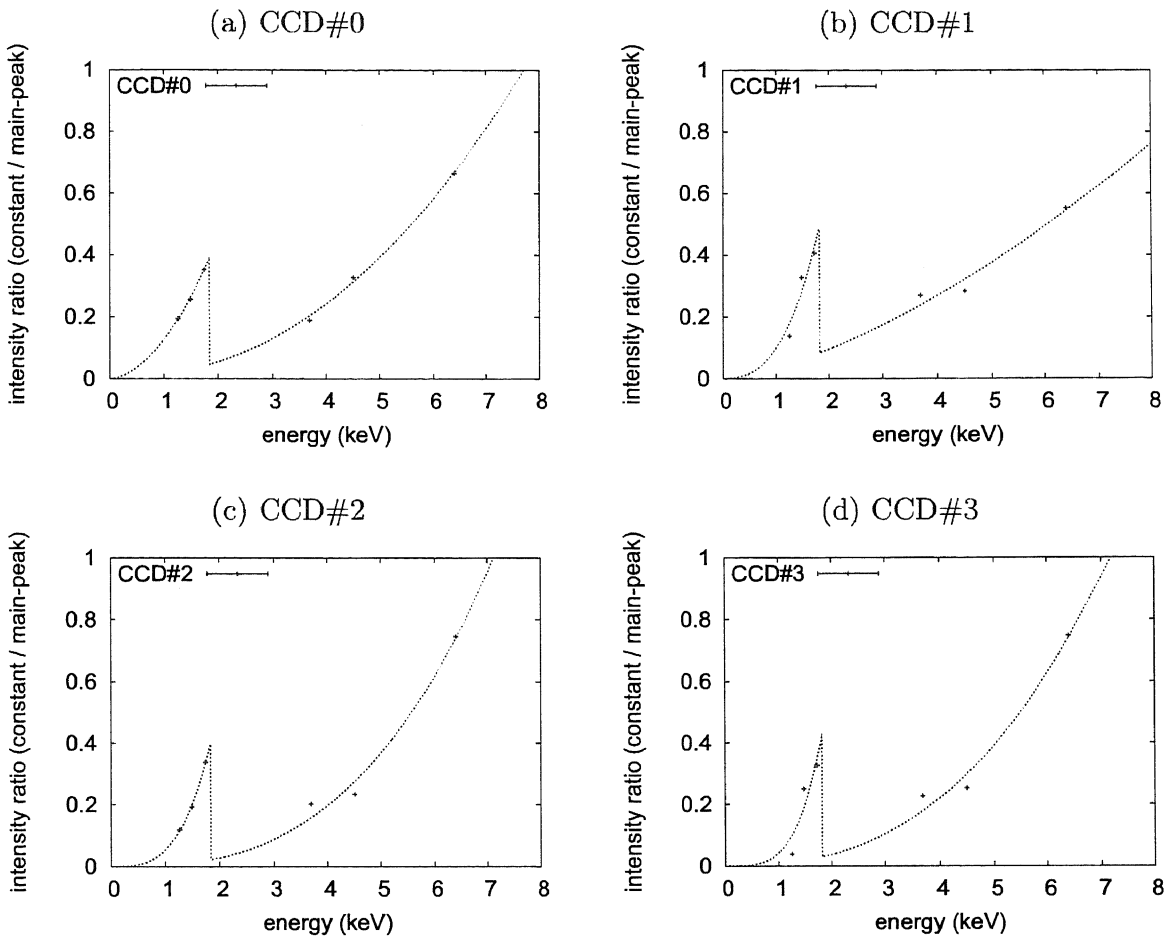

Figure 5.5: Intensities ratio for continuum component / main-peak measured in laboratory experiments, where the temperature of CCD is -53 ± 1 degrees Celsius which is about the temperature when XRS observed Itokawa.

Table 5.1: Best-fit the continuum component model to observed spectrum.

range (keV)	a	b
<1.84	0.096 ± 0.051	2.675 ± 1.088
>1.84	0.033 ± 0.020	1.507 ± 0.356

5.3 Measurement of detection efficiency

In order to estimate the detection efficiency of the XRS, X-rays from the ^{55}Fe radio isotope with the XRS and the Si-PIN photodiode (PD) was measured as schematically shown in Figure 5.6.

Since the XRS and the Si PIN photodiode (Amptek, 2001) were used to measure X-rays from ^{55}Fe in air circumstance, the air attenuation for X-rays was corrected by using the typical weight percent of dry air such as N_2 (75.51 wt.%, O_2), 23.01 wt.%, Ar (1.286 wt.%), and CO_2 (0.040 wt.%) (Rikanenpyo, 2002). Table 5.2 shows the detail configuration of the ^{55}Fe measurements. The count rate of X-rays from ^{55}Fe was 11.8 $\pm$4.6 events/3.3sec/frame.

Figure 5.7a shows the anticipated detection efficiency of Si-PIN photo-diode. The detection efficiency depends on the gate structure of the sensor. The thickness of Beryllium window was assumed to be 25μm, and the thickness of depletion layer was assumed to be 300 μm.

The detection efficiency of the XRS was estimated, and then the observed X-ray intensities of XRS is related to that of Si-PIN photodiode as follows,

$$E_{\rm XRS} = E_{\rm PD} \times \frac{T_{\rm PD}}{T_{\rm XRS}} \times \frac{S_{\rm PD}}{S_{\rm XRS}} \times \frac{A_{\rm PD}}{A_{\rm XRS}} \times \frac{C_{\rm XRS}}{C_{\rm PD}},$$

where E is a detection efficiency, T is an integration time, S is an effective area, and A is a correction factor and C is photon counts. Then error (*e.g.*, Bevington and Robinson, 2003) is written as follows,

$$\delta E_{\rm XRS} = E_{\rm PD} \times \frac{T_{\rm PD}}{T_{\rm XRS}} \times \frac{S_{\rm PD}}{S_{\rm XRS}} \times \frac{A_{\rm PD}}{A_{\rm XRS}} \times \frac{C_{\rm XRS}}{C_{\rm PD}} \sqrt{\left(\frac{\delta C_{\rm XRS}}{C_{\rm XRS}}\right)^2 + \left(\frac{\delta C_{\rm PD}}{C_{\rm PD}}\right)^2}.$$

Table 5.3 shows the best-fit results of X-ray measurement of ^{55}Fe (Figure 5.8). Table 5.4 shows the estimated detection efficiency of XRS in the energy range of 5.9 keV.

The detection efficiency of XRS also depends on CCD gate structures (aluminum coating $\sim 0.2\mu$m, poly silicon gate $\sim 0.4\mu$m, SiO_2 insulator $\sim 1.8\mu$m, and beryllium window (5μm) as optical shield. Incident X-rays were exponentially attenuated and absorbed in CCD gates, and thus the detection efficiency of XRS Q was given as follows,

$$Q(D,\theta;E) = \exp\left(-\frac{\mu_{\rm Be}}{\cos\theta} - \frac{\mu_{\rm Al}}{\cos\theta} - \frac{\mu_{\rm Si}}{\cos\theta} - \frac{\mu_{\rm SiO_2}}{\cos\theta}\right) \times \left[1 - \exp\left(-\frac{\tau_{dep}}{\cos\theta}\right)\right],$$

where θ is an X-ray incident angle, μ is an X-ray attenuation coefficient (see Figure 2.2), τ is an X-ray absorption coefficient, and $d_{\rm Dep}$ is the thickness of depletion layer. If the thickness of depletion layer $d_{\rm dep}$ was assumed to be 13.5 $\pm$ 0.6 μm (Grade 0+1+2+3), the detection efficiency is equivalent to the one shown in Figure 5.8.

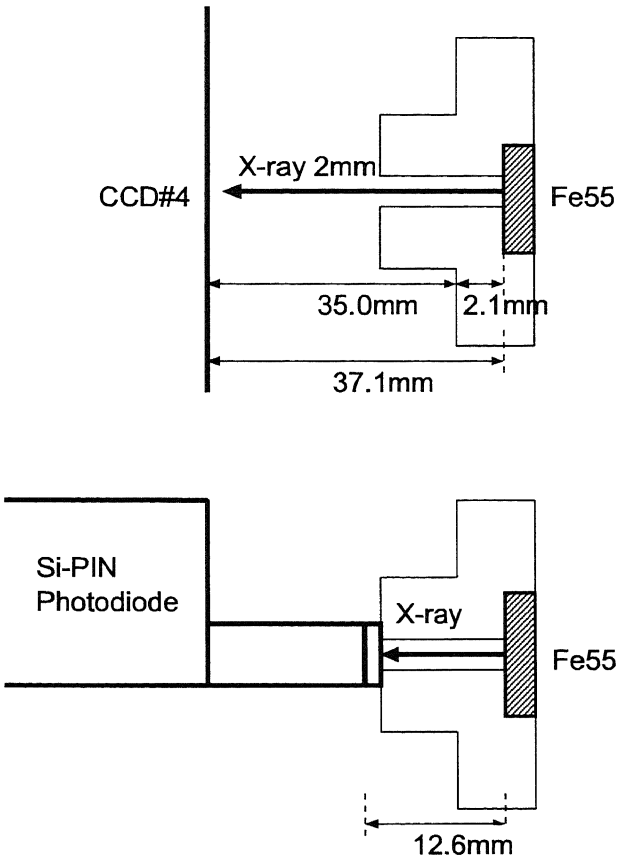

Figure 5.6: Schematic view of experiments of detection efficiency measurements. The XRS and Si-PIN photo-diode measured X-rays from ^{55}Fe isotope in air.

Table 5.2: Configuration (^{55}Fe)

Date	April 25 and 27, 2002
Circumstance	XRS-S @ thermal chamber
	-40 degrees Celsius Dry-air purged
	XRS-E electronics in room
detector	XRS: (CCD#4), Si-PIN photo-diode
effective area	CCD: 25.4 mm × 25.4 mm, PIN: 2.4 mm×2.8 mm
target	^{55}Fe: (half-life: 2.7 years)
pinhole	2 mm ϕ (ARAI pinhole#2)

(a) Detection efficiency of PD

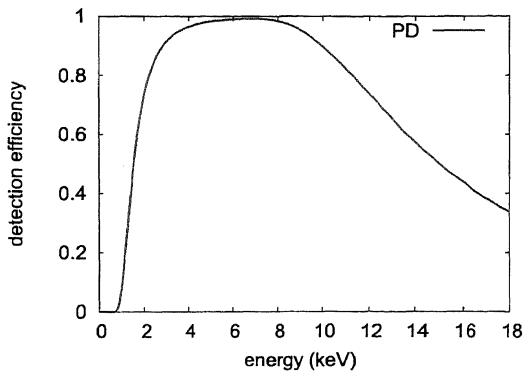

(b) Observed spectra of PD

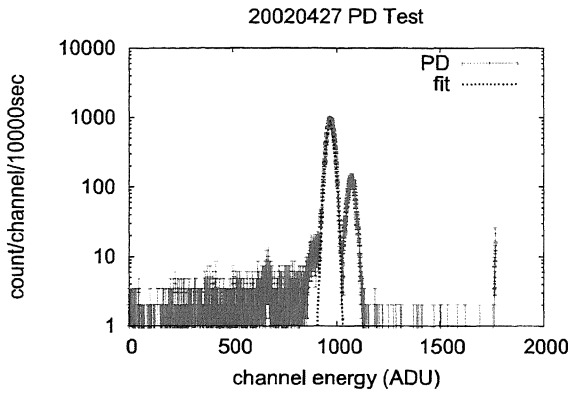

Figure 5.7: (a) Anticipated detection efficiency of Si-PIN photo-diode. The thickness of Beryllium window was assumed to be 25μm, and the thickness of depletion layer was assumed to be 300 μm, (b) Observed and Gaussian-fitted spectrum for ^{55}Fe spectrum by Si-PIN photo-diode.

(a) Detection efficiency of XRS

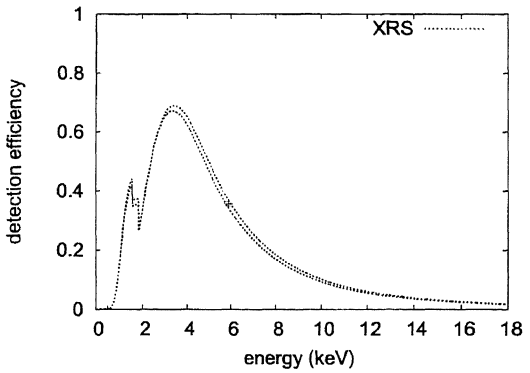

Observed spectrum of XRS

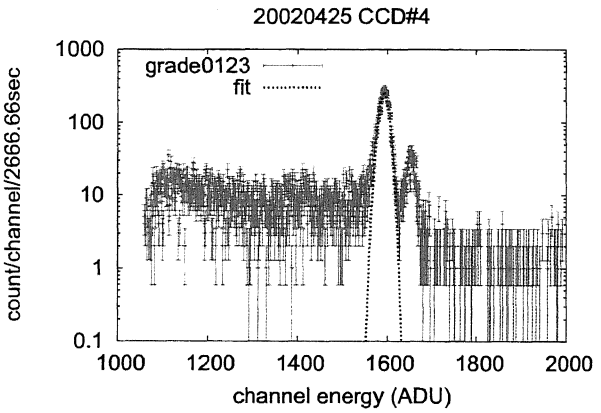

Figure 5.8: (a) Anticipated detection efficiency for XRS. (b) Observed spectra of XRS (20020425). If the thickness of depletion layer $d_{\rm dep}$ was assumed to be 13.5 $\pm$ 0.6 μm (Grade 0+1+2+3), anticipated detection efficiency was equivalent to the value of figure (a).

Table 5.3: Results of Gaussian fitting to Mn-Kα peaks (5.9 keV).

	CCD#4 (Grade 0)	CCD#4 (Grade 0+1+2+3)	PIN-photo-diode
Intensity	2686.0 $\pm$ 67.3	6639.2 $\pm$ 140.2	39662.3 $\pm$ 222.9
Peak center	1596.1 $\pm$ 0.2	1594.2 $\pm$ 0.2	970.9 $\pm$ 0.1
Standard dev.	7.7 $\pm$ 0.2	9.9 $\pm$ 0.2	16.9 $\pm$ 0.1

Table 5.4: The detection efficiency of XRS at 5.9 keV.

Grade 0	Grade 0+1+2+3
14.4 $\pm$ 0.4 %	35.6 $\pm$ 0.8 %

5.3.1 Grade ratios

XRS usually carries out observation with the grade-0 mode (Figure 3.8) because energy resolution is better than other spectra of grade modes. Therefore, it is necessary to correct the grade ratios (grade0/grade0+1+2+3) for the detection efficiency. The grade ratios were also complemented with the power-law model as shown in Figure 5.9. Table 5.5 shows the best-fit results of power-law fitting.

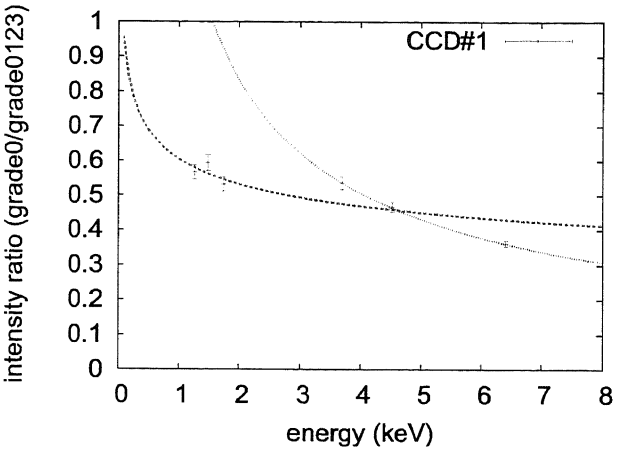

Figure 5.9: Grade ratios for each fluorescence peak of Kα lines for Mg (1.25 keV), Al (1.49 keV), Si (1.74 keV), Ca(3.69 keV), Ti (4.51 keV), and Fe (6.40 keV)

Table 5.5: Grade ratios (CCD#1)

energy range (keV)	a	b
<1.84	0.604 ± 0.065	-0.184 ± 0.260
>1.84	1.370 ± 0.019	-0.717 ± 0.008

5.3.2 Systematic errors

It is necessary to propagate systematic errors as sensor characteristics to the Itokawa observation results, such as errors of detection efficiency, and errors of grade ratios. These results should be propagated to analysis of Itokawa spectra.

Table 5.6: Systematic error ratios of X-ray intensities for each line (%)

Element	Mg	Al	Si	S	Ca	Fe
Error of detection efficiency	2.1	3.9	5.4	5.5	3.3	8.0
Error of Grade ratio	3.7	3.9	3.8	3.9	3.6	2.3

5.4 Examples of anticipated spectra

Figure 5.10 shows the model spectra and anticipated spectra for XRS observation. The target was assumed to be the average of LL-ordinary chondrites analogues. The verification of the XRS response models was carried out in the cruising phase as described in Chapter 6.

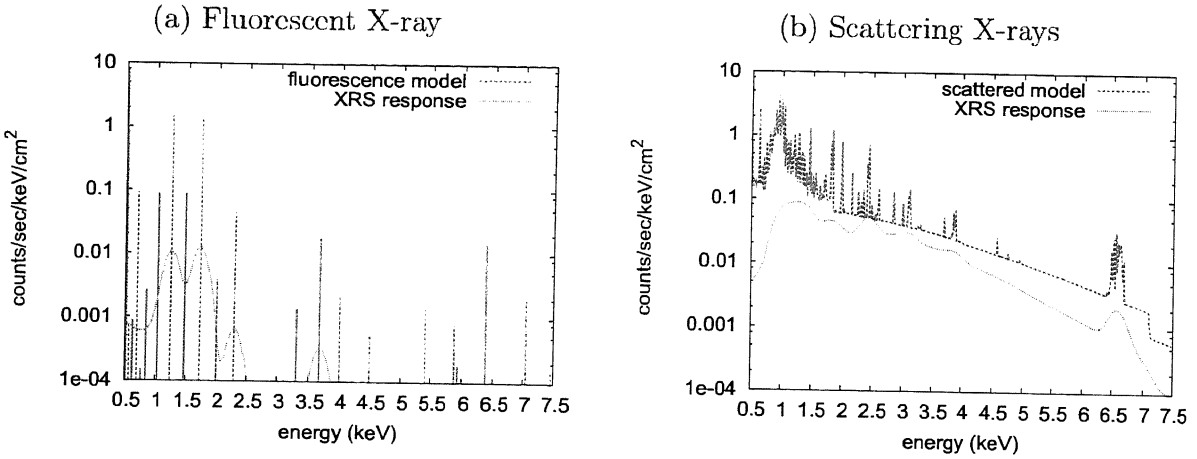

Figure 5.10: (a) X-ray fluorescence spectra convolved by the response function. (b) Scattering X-ray convolved by the response function. Green lines indicate incident spectra to XRS, and pink lines indicate the convolved response function spectra.

Chapter 6

Performance of XRS in Cruising Tests

In this chapter, the sensor performances of XRS in the cruising phase are described. Here, only the effective data, such as the data of the standard sample observation during the occurrence of a solar flare, and X-ray background observation, are analyzed.

6.1 Overview of sensor performance of XRS

The XRS observed X-ray backgrounds every week in order to verify the response function and the X-ray models. Figure 6.1 shows forward pointing of XRS (solid line) in the equatorial coordinate system (J2000). The crosses denote the brightest X-ray sources observed by XRS, such as Sco X-1, Kepler's SNR, Crab nebula, and IC443 (Arai *et al.*, 2004).

Although observations were carried out, observed spectra did not fit to the anticipated spectra, especially in the lower energy range. The main reason might be the increasing of dark current due to radiation damage (*e.g.*, Yamashita, 1995). The onboard reduction usually reduced the dark currents but background reduction logic did not operate in the period. The failures of dark current reduction made it hard to analyze the observation data. Fortunately, the failures were recovered by an upgrade of the onboard software as described in Appendix A.

Fortunately, X-ray spectrum of the standard sample in a solar flare condition was obtained, and thus it was used to verify the response function and X-ray models. Also, cosmic X-ray backgrounds were observed, and the model was constructed, which were used in the analysis of Itokawa spectra.

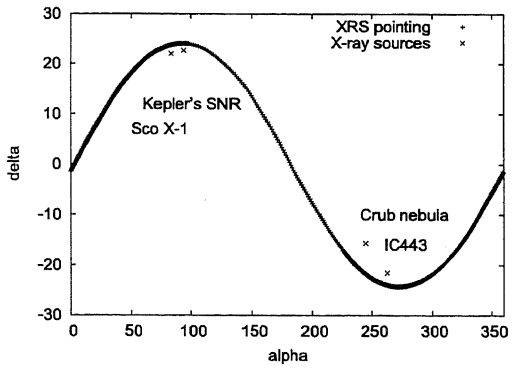

Figure 6.1: XRS pointing coordinate in the equatorial coordinate system (J2000) in cruising phase. The solid line denotes the pointing forward, mostly filled with cosmic X-ray backgrounds. The cross points indicate observed X-ray sources such as, Sco X-1 (16h19m55s, -15h38m25s), Kepler SNR (17h30m41s,-21h29m11s), Crab nebula (05h34m32s,22h00m52s) and IC443 (06h18m03s,22h39m36s).

6.2 Measurement of solar X-rays with standard sample

There is no confirmed model for the solar X-rays, and thus it is necessary to evaluate known solar X-ray models whether they are usable or not. On May 29, 2003, solar flares occurred, and then XRS measured the X-ray emission from the standard sample. In order to verify the X-ray models, the model spectrum was fitted to the observed spectrum by least squares-fit, where parameters for plasma temperature and emission measure were required. These values can be calculated by the Feldman *et al.*, (1996) 's formula in Equation 4.1. The initial values of parameters were assumed to be the observed values of GOES X-ray flux (GOES web site). Solar flare events and relatively smaller flare events are found in Figure 6.2.

The best-fit solar X-ray models for the observed spectrum of the standard sample are shown in Figure 6.3. Since χ^2 of the blend of two MEKAL models was smaller than that of one MEKAL model, the former model as the blend of two MEKAL models were used for the analysis of the Itokawa observation.

(a) GOES X-ray flux

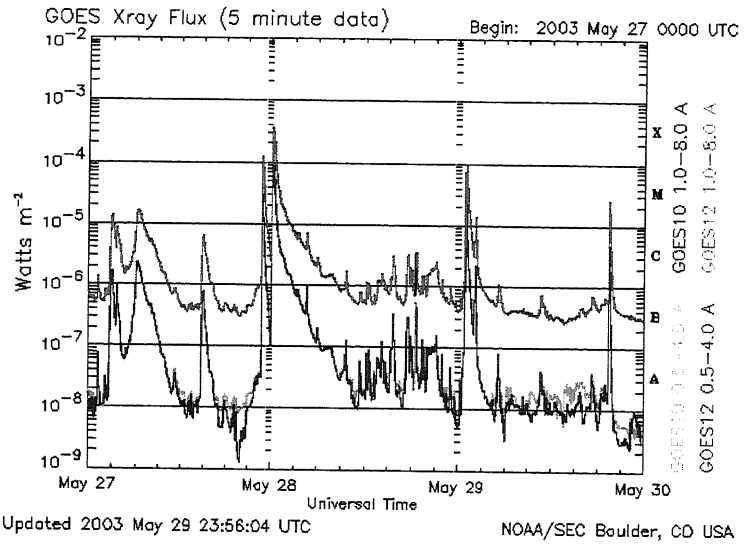

(b) GOES X-ray image

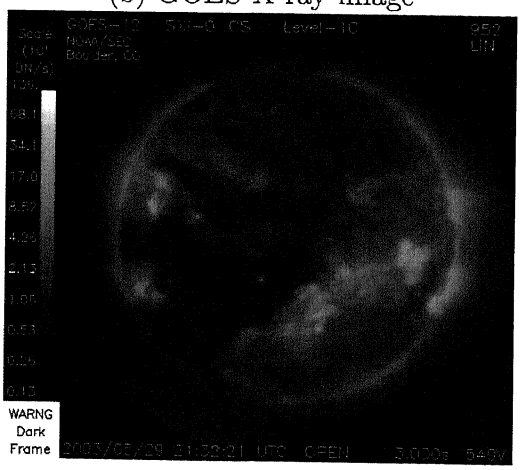

Figure 6.2: GOES X-ray flux (May 29, 2003). (a) X level flares occurred on May 29, 2003. (b) GOES X-ray image obtained from NOAA web site.

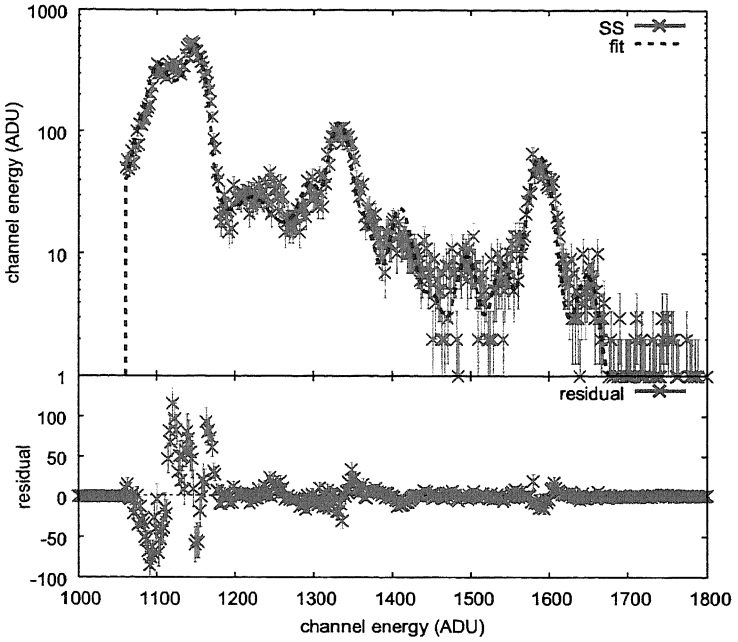

Figure 6.3: Best-fit the model of two MEKAL blends to the observed spectrum..

6.3 Measurement of X-ray backgrounds

Major X-ray backgrounds (XRB) are the thermal X-ray emissions from our galaxy produced by disk accretion, space radiations, charge exchange between electrons, and so on (Ishisaki, 1996). These X-rays are absorbed in interstellar objects and this effect is given as a function of interstellar cross section. In this absorption model, the Morrison and McCammon model (1983) were used as shown in Figure 6.4. The X-ray backgrounds include cosmic X-ray backgrounds and non X-ray backgrounds.

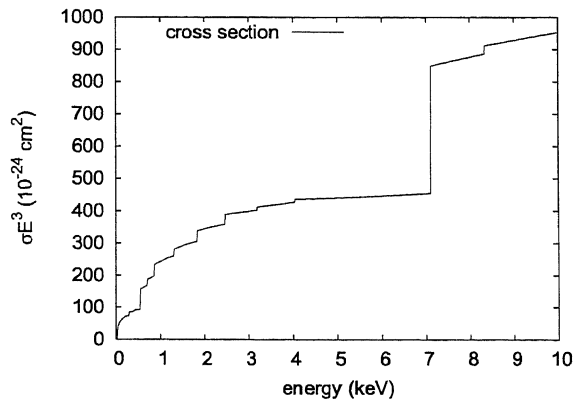

Figure 6.4: Photoelectric absorption cross section obtained by Morrison and McCammon (1983). X-ray emission from all sky will be affected by this attenuation. The XRS will evaluate the space abundance from the features of absorption to resolve the observed spectrum. A large jump at about 0.5 keV is O, and about 7 keV is Fe.

6.3.1 Cosmic X-ray backgrounds

Space is filled with X-rays called cosmic X-ray background (CXB). It is composed of many X-ray sources. For example, soft X-ray energy range is dominated by a thermal X-ray radiation, such as supernova remnants in our galaxy, and hard X-ray energy range is dominated by high energy X-ray generators, such as X-ray binaries, and active galactic nuclei (Ishisaki, 1996). The CXB has been studied by Ishisaki (1996) and Yamashita (1999) with the X-ray astronomical satellite, ASCA. The X-ray model spectrum was assumed to be given as power-law (soft X-ray region) and absorbed power-law (hard X-ray region) as follows,

$$I_{\rm CXB} = N_{\rm hard} E^{-1.378} + N_{\rm soft} E^{-6.0} \times \exp(-\sigma n_H) \tag{6.1}$$

where $N_{\rm hard}$ and $N_{\rm soft}$ are the proportionality constants for the hard X-ray component and for the soft X-ray component, respectively, σ is an interstellar cross section ($\rm cm^2$) (Morrison and McCammon, 1983), and n_H ($\rm g/cm^3$) is the hydrogen column density. The flux of soft X-rays was assumed to be 5.83×10^8 $\rm erg/s/cm^2/str$ (0.5–2.0 keV), and the flux of hard X-rays was assumed to be 1.33×10^8 $\rm erg/s/cm^2/str$ (2.0–10.0 keV), and n_H is assumed to be 1.0×10^{20} $\rm cm^{-2}$. These values have been estimated by Yamashita (1999) for SA57 near the galactic polar region. Figure 6.5a shows the model of CXB given by Equation 6.1 and Figure 6.5b shows the anticipated spectrum of XRS. This anticipated spectrum of CXB is used for the analysis of Itokawa as a background spectrum.

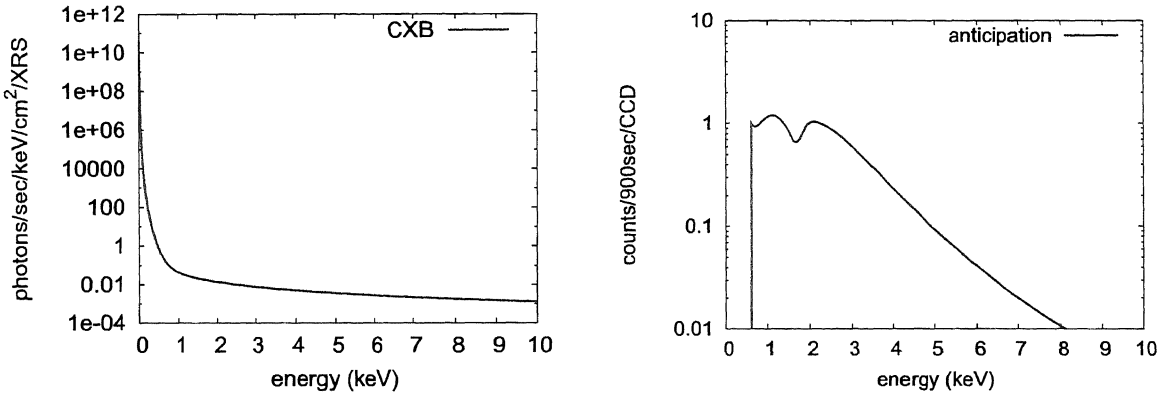

(a) Cosmic X-ray backgrounds (b) anticipated spectrum (900sec)

Figure 6.5: Cosmic X-ray back ground (CXB) model which is coming from all over the sky (Ishisaki, 1996). The model was obtained from ASCA/GIS Large Sky Survey. (a) Incident spectrum to XRS. (b) Anticipated spectrum of XRS.

6.3.2 Non X-ray background

Particle radiations often cause X-ray events called non-X-ray back ground (NXB). High energy particles hitting the detector disperse in many pixels of CCD, and these empirically make a constant spectrum in the whole energy range. It has been measured by the X-ray astronomical satellite, ASCA. In observations of XRS, anticipated intensities of radiation events were larger than those of the ASCA night earth observation, ~0.001 counts/sec/keV/$\rm cm^2$ (HEASARC's web page) because radiation intensity was larger under interplanetary conditions than at the low Earth orbit. The anticipated intensity for XRS was about 16 times larger than for ASCA/SIS because the effective area of XRS was 4 times as large as that of ASCA/SIS, and the flux of space radiation was about 3 or 4 times as large as that of ASCA. If so the anticipated intensity of NXB for XRS was assumed to be 0.012 (counts/sec/keV/CCD). Figure 6.6a shows

the incident model spectrum of NXB which was a constant spectrum in all energy ranges. Also, Figure 6.6b shows the anticipated spectrum for XRS which was used in the analysis of Itokawa as background spectrum.

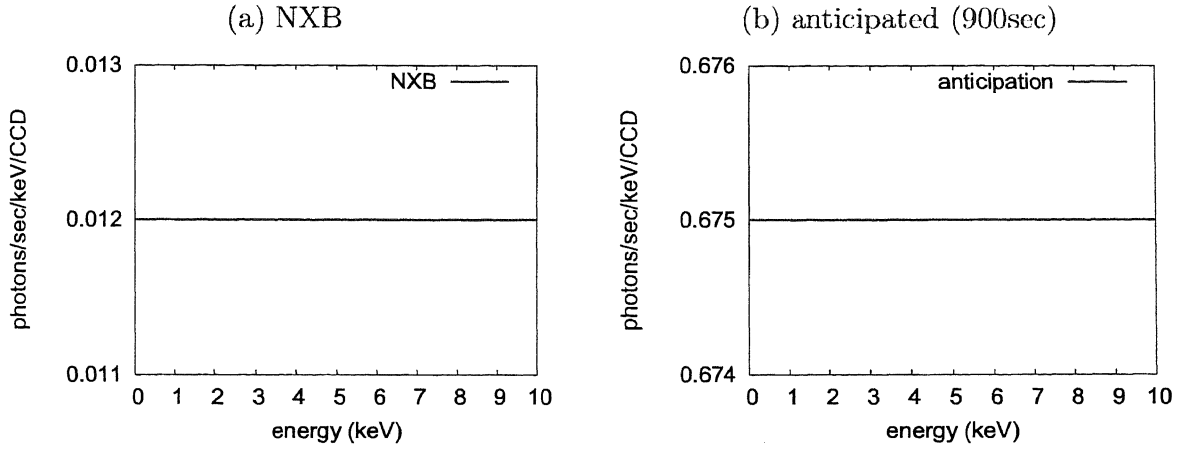

Figure 6.6: Non X-ray background (NXB) model obtained from ASCA night Earth observation data.

6.3.3 Observation of X-ray backgrounds

The X-ray background observation is important for sensor calibration. The XRS observed X-ray backgrounds every week. Figure 6.7 shows an example of the observation spectra. Continuum spectrum is shown in this figure but it appears to be discrete spectra due to short time integration due to temperature changes of sensor caused by turn ON or OFF of the ion thruster of the Hayabusa. Although the observed data is noisy, observed X-ray intensities are roughly consistent with the anticipated spectra (Figures 6.5 and 6.6). Figure 6.8a shows the results ROSAT/PSPC which observed space near the ecliptic plane, and the flux observed by XRS is shown in Figure 6.8b. They resemble each other though the data of XRS included hot-pixels as instrumental noises (see Appendix A).

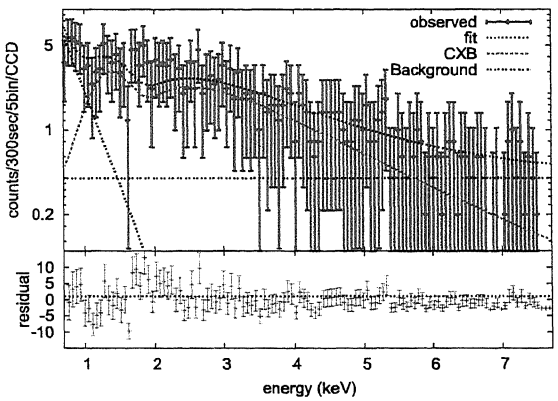

Figure 6.7: Observed X-ray background spectrum and X-ray models (Jun 1, 2005, 4:17:05, 300 seconds integration (5 channels bin), heliocentric coordinates (231.52, 33.92). Since the integration time was short, the observed spectrum included large counting statistics errors (*e.g.*, Knoll, 2000). Although the errors were large, the observed spectrum resembled the XRB model spectrum.

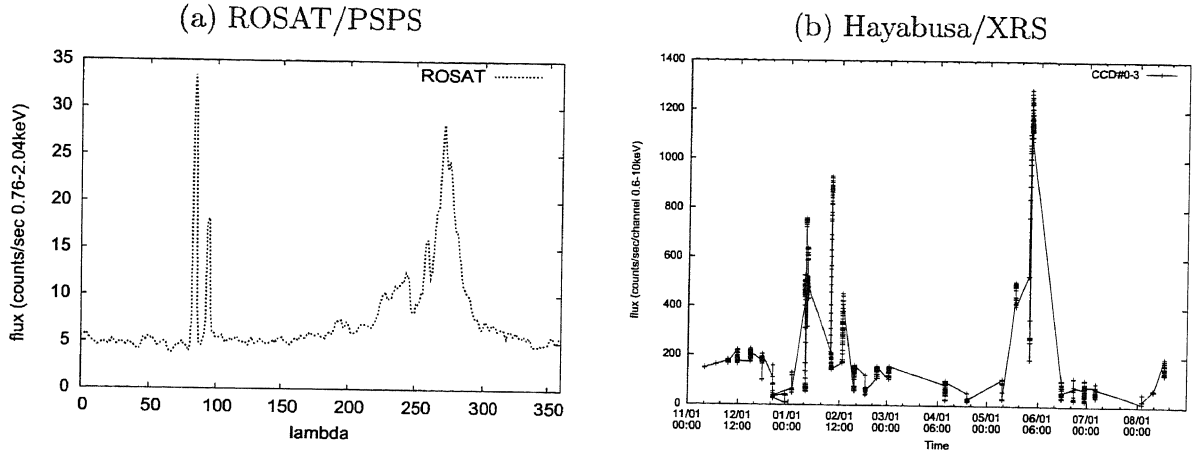

Figure 6.8: (a) ROSAT/PCPS observation near the ecliptic plane, which is taken from the ROSAT All Sky Survey (HEASARC's web site). Time of observation is different from that of XRS observation. (b) XRS observed flux during 1 year observation (4 CCDs integration). These time variations show similar temporal patterns with the results of ROSAT.

Chapter 7

X-ray Observation of Itokawa

In this chapter, observation of Itokawa with the XRS is described. During the Itokawa observation, failure of reaction wheels of Hayabusa caused the following consequences, (1) XRS could not maintain long time continuous pointing to Itokawa, and (2) frequent thermal changes of XRS caused degradation of energy resolution. Regrettably, (3) Solar activity was relatively low in the observation period.

7.1 Overview of XRS observation

During September to November in 2005, XRS observed the surface materials of Itokawa from a distance of 20 km to 0 km. Science observation was carried out in the phase of gate position, home position, tour, and touch down. The tour was performed from October 8 to 28, where the Hayabusa spacecraft moved from the eastern side to the western side of Itokawa. Unfortunately, two reaction wheels used as attitude controllers were broken in late July and early October, and thus XRS could not maintain long time continuous pointing to Itokawa. Navigation guidance tests were performed on November 9, 2005. The sampling of surface material was performed on November 19 (TD#1) and November 26 (TD#2), 2005. Fortunately, some obtained data were sufficiently good to determine the elemental composition of Itokawa when solar flares occurred.

The observed areas of XRS, limited by the mechanical collimator, are calculated by the SPICE kernel. Unfortunately XRS did not always point to Itokawa because the attitude of Hayabusa is unstable due to failure of reaction wheels. Total pointing times are 2% of total observation periods. Therefore, XRS observed not only Itokawa but also backgrounds such as cosmic X-ray backgrounds or space radiation as shown schematically in Figure 7.1. The observation areas and distance are shown in Figure 7.2.

Solar activity was relatively high in the first-touchdown and away (TD#1) operation, aiming at a sample collection on November 19, 2005. The altitude of Hayabusa was controlled by pulse jets of thrusters. The altitude accuracy for pointing diagonal forward is $\pm 1.25°$, and X and Y forward is $\pm 0.88°$.

In order to obtain statistically significant data, high solar activities were required. In the middle of November, 2005, solar activity became relatively enhanced, according to the observed X-ray flux of GOES 10 and 12 satellites, as shown in Figure 7.3. Although Itokawa and the XRS were located in backside of the flare region, the XRS detected high signals for observed spectrum of the standard sample. Thus the solar X-ray model was derived by using the observed spectra of the standard sample. Also the SOHO solar X-ray imager has observed solar flare events in the west side of the Sun. It implies that solar actively was also high at the Itokawa location.

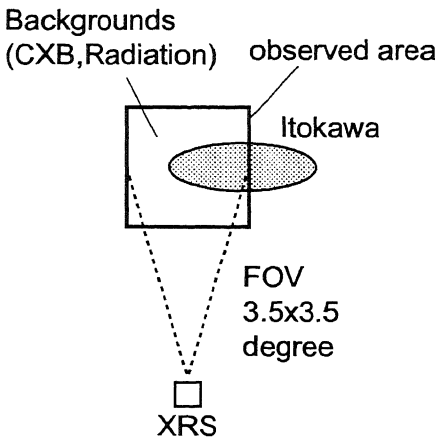

Figure 7.1: XRS observed not only Itokawa but also backgrounds such as cosmic X-ray backgrounds or space radiation. The ratios of backgrounds in FOV ($3.5^\circ \times 3.5^\circ$) of XRS are calculated by the SPICE kernel.

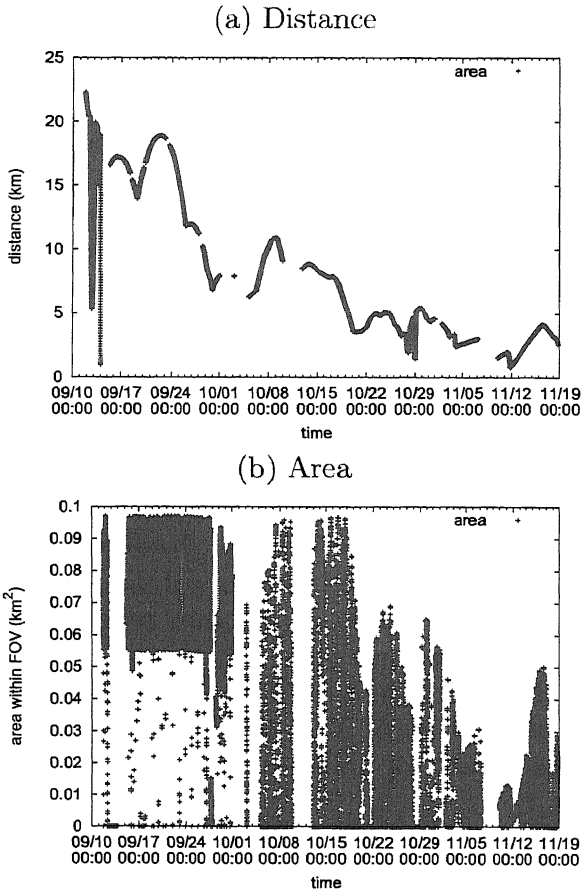

Figure 7.2: (a) Observation area. (b) Observation distance (Itokawa center–XRS)

(a) X-ray flux level observed by GOES

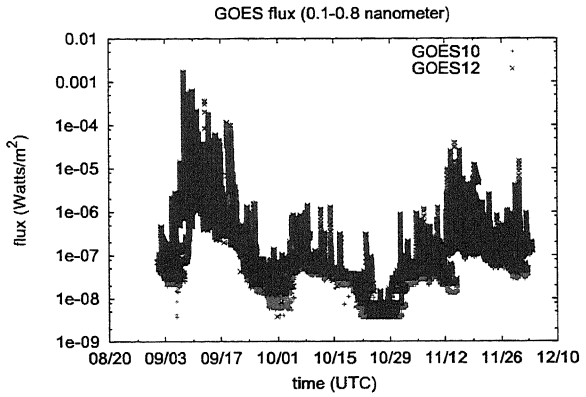

(b) UV image of the Sun observed by SOHO

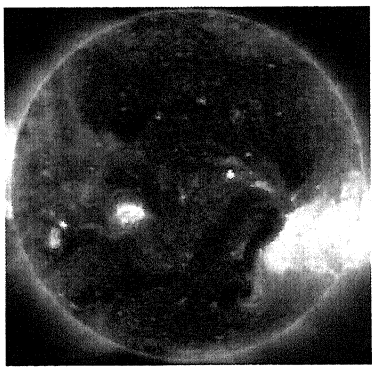

Figure 7.3: GOES flux *vs.* time during the Itokawa observation period obtained from NOAA web site. In the middle of November, 2005, solar activity was high, as observed by the GOES 10 and 12 satellites, (b) An X-ray flare image by SOHO Extreme ultraviolet Imaging Telescope (EIT) in 195 Å. A solar flare burst occurred in west side of sun. This image implies that solar activity became enhanced at the Itokawa location. (NOAA web site).

7.2 Status of XRS

The CCDs were cooled with a peltier cooler, and they were controlled at the temperatures of -52 ± 2 degrees Celsius during this period. This temperature enables a good energy resolution but the data during landing on Itokawa were noisy due to increase of dark current, accompanied with an increasing temperature of the CCDs. Therefore, only the data obtained during the decent phase of Hayabusa were analyzed.

The temperatures of CCDs in all observation period are shown in Figure 7.4a. The temperatures of CCDs were increasing in the approach to Itokawa, and dark current was also increasing. In order to reduce the dark current, active cooling with peltier device was performed from October 20, 2005 to the end of observation. The temperature of the pre-amplifier in the all observation periods are shown in Figure 7.4b.

The total numbers of spectra packets were amounted to 12611 during September. 8, 2005 (2:13:50) (TI:8C980056) to November 24, 2005 (22:18:01) (TI:996BCBBC). Table 7.1 shows the observation mode and observed data sets, including mode #ID, background update duration, integration time, compress ON/OFF, grade, and observed number of packets.

(a) CCD temperature *vs.* time

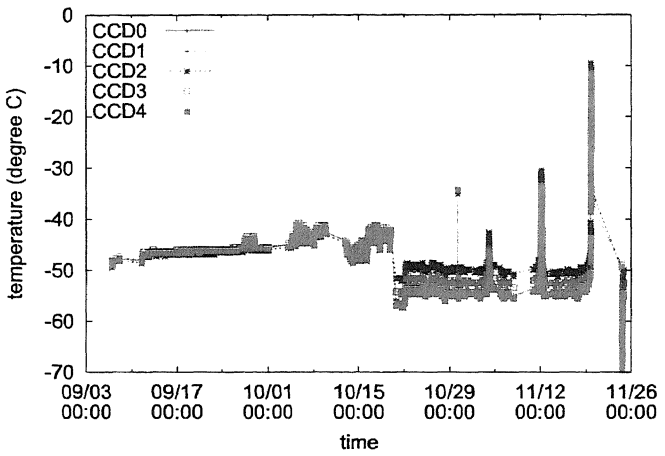

(b) Pre-amplifier temperature *vs.* time

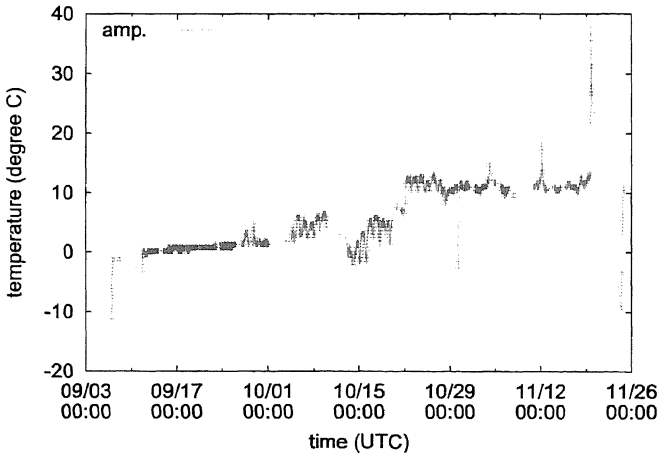

Figure 7.4: (a) **The temperature of CCDs,** (b) **The temperature of pre-amplifier. In order to reduce the dark current, active cooling with peltier device was performed from October 20, 2005 to the end of observation.**

Table 7.1: Observation mode and observed data sets.

Mode	BG time	Integ.time	Background	Compress	Grade	Observed packets
00	30	30	PIX1	OFF	Grade-0	380
44	30	300	PIX1	ON	Grade-0	330
A4	60	60	PIX1	ON	Grade-0	153
C4	60	300	PIX1	ON	Grade-0	9236
D4	60	300	PIX12	ON	Grade-0	1106
D7	60	300	PIX12	ON	change Grade	9
DC	60	300	AVE	ON	Grade-0	1395
DD	60	300	AVE	ON	Grade-All	2

7.3 Solar activity

Solar activity varies in about 11 year's cycle. Solar X-rays are roughly proportional to solar activity, and thus it is a critical factor for remote X-ray fluorescence observation. Figure 7.5a shows the number of sun-spots which represents solar activity. Figure 7.5b shows the number of solar flare events observed by GOES satellites. Unfortunately, in the Itokawa observation phase in 2005 the sun was in quiet condition.

(a) The number of sunspot

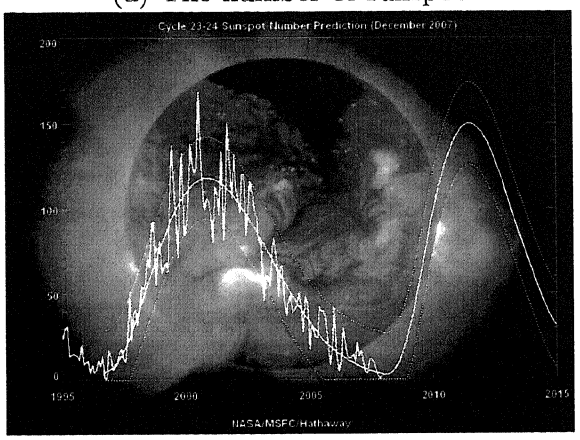

(b) The number of flare events

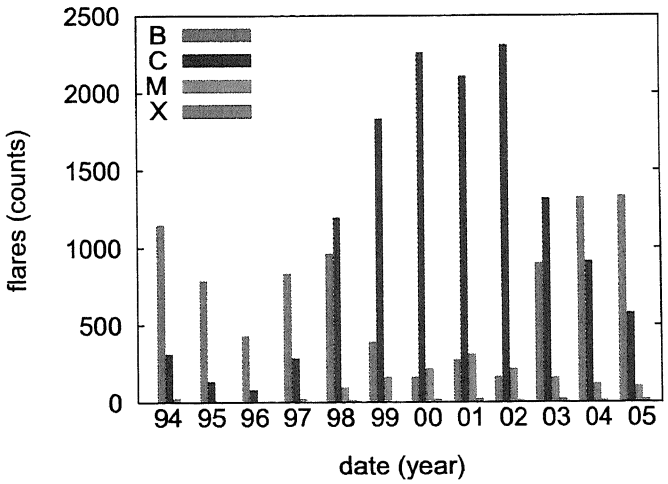

Figure 7.5: (a) The number of sunspots (average number for month). Solar flare occurs in breaks of magnetic field lines in sunspots, obtained by http://solarscience.msfc.nasa.gov/. (b)The number of solar flare events observed by GOES satellite (http://www.lmsal.com/SXT/).

7.4 Critical problems during observation

Failure of reaction wheels caused critical problems. In particular, pointing time of Itokawa was reduced. Also, energy resolution degraded due to thermal changes of sensor. They were caused by changes in dark currents. Also, fluctuation of dark currents caused peak shifts in energy spectrum as shown in Figure 7.6. This figure shows that the offset shift was a few channels (1 channel $\sim$ 10 eV), and thus the peak corrections were required in analysis.

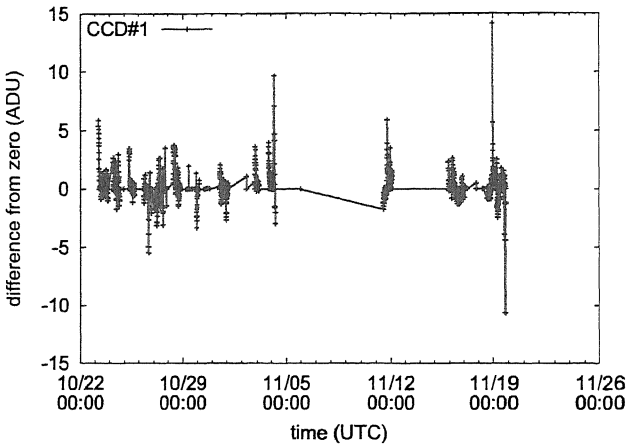

Figure 7.6: Peak offset shifts of observed spectra. Peak offset mainly varied due to dark currents. Regrettably, thermal changes were caused by attitude changes of spacecraft due to failure of reaction wheels.

Chapter 8

Analysis of Globally Observed Spectra

In this chapter, analysis methods and results for the global analysis of Itokawa spectra by XRS are described, where average abundance of the surface materials of Itokawa, such as the elemental ratios of Mg, Al, Si, S, Ca, and Fe, are estimated.

8.1 Method of analysis

In order to estimate the elemental mass fractions of Itokawa, least squares-fits were used for comparing the observed spectrum with the model spectrum. The elemental mass fractions as elemental abundances were assumed to be the parameters of the models, and thus the best-fit model spectrum to the observed spectrum indicated the best-fit elemental mass fractions of Itokawa. The algorithms of the fitting were a simplex method (Press *et al.*, 2001a) and a Levenberg-Marquardt method (Press *et al.*, 2001b). The simplex method performed well but error could not be estimated. In contrast, the Levenberg-Marquardt method often resulted in no convergence but errors could be estimated. Therefore, the simplex method was used for the initial-fits, and then standard errors were determined by Levenberg-Marquardt method. Here, the standard sample was not used for comparative analysis (Masuda, 2001; Okada *et al.*, 2006) but for the solar X-ray monitor because the elemental composition of the standard sample was probably not similar to that of Itokawa (see Tables 3.1 and 8.3).

The attitude of Hayabusa was unstable due to the failure of reaction wheels as an attitude controller as described in Chapter 7. This led to a decrease in pointing time to Itokawa and to an increase in the dark current or the number of flickering pixels due to thermal changes of CCDs. Therefore, it required selection of effective data in persuit of low noise and flare events. The detail analysis methods are described bellow.

8.2 Analysis of observed spectra

In order to estimate the elemental mass fractions of Itokawa, backgrounds of observed spectra were subtracted, and least squares-fit of the model spectrum and the observed spectrum were performed. Figure 8.1 shows the flow of this analysis. This figure indicates the following: (1) The background spectra were estimated by analysis of the spectra with Itokawa out of view of XRS, and effective data were selected by analysis of these background spectra. (2) The solar X-ray model was estimated by the analysis of the observed spectra of the standard sample. (3) The elemental mass fraction of the surface materials of Itokawa were estimated by using the observed spectra of Itokawa.

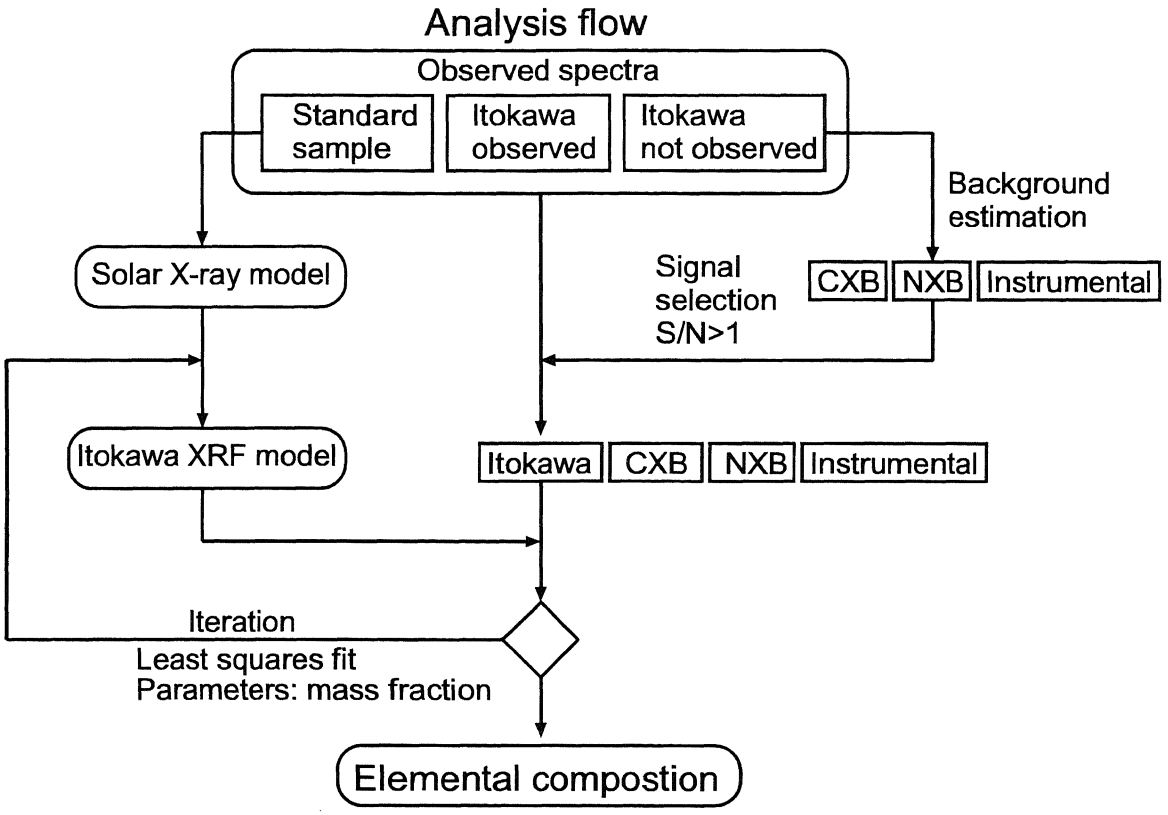

Figure 8.1: **Analysis flow for deducing observed spectra of the standard sample and Itokawa. (1) The backgrounds in the observed spectra were estimated by using the spectra with Itokawa out of view of XRS, and effective data were selected by using these background spectra. (2) The solar X-ray model was estimated by analysis of the observed spectra of the standard sample. (3) The elemental mass fraction of the surface materials of Itokawa were estimated by using the observed spectra of Itokawa.**

8.2.1 Estimation of backgrounds and selection of effective spectra

In order to estimate the backgrounds in the observed spectra of Itokawa, five points were checked within the integrated times every 300 seconds whether Itokawa was within the field of view of XRS or not for the polygon faces of Itokawa (Demura *et al.*, 2006) for every integrated spectrum.

Figure 8.2 shows a background spectrum with Itokawa out of view of XRS, for integrated time of 150000 seconds, where the background included the X-ray events of CXB and NXB as described in Chapter 6 (Figure 6.5 and 6.6). Since these two spectral backgrounds did not fit the background spectrum, three instrumental backgrounds, expressed by Gaussian, were assumed (BG1, BG2, and BG3). Table 8.1 shows the best-fit results of instrumental backgrounds. In the channel energy of 1100–1200, BG1 was far larger than other backgrounds. It caused a critical noise in the energy of X-ray fluorescence peaks such as Mg, Al, and Si. The possible cause for these backgrounds were fake events due to fluctuations of dark current or hot-pixels, and instrumental noise (see Appendix A).

In order to extract the effective spectra to obtain most representative data for the elemental abundance of Itokawa, the data selection were performed as following:

(1) The observed spectra were extracted only when CCD was cooled with the peltier device, because the dark current was decreasing due to relatively lower temperature of CCDs during the observation period (Figure 7.4).

(2) The observed spectra were extracted only when sun light illuminated the standard sample because it is necessary to estimate the incident solar X-rays for quantitatively analysis of the observed spectra of Itokawa. The angles of the Sun–standard sample–XRS in the Hayabusa coordinate system are shown in Figure 8.3. Thus, only the sun-lit data were extracted when the sun was in the quadrant with X>0 and y>0 in the Hayabusa coordinate system (see Figure 3.2) because the other quadrants have not sunlit due to the shade of the Hayabusa spacecraft.

(3) The observed spectra were extracted only when the flux of X-ray signals was larger than the flux of backgrounds, that is, when the flux of observed spectra was larger than the flux of three σ of BG1 in the channel energy. The background ratios of CXB in FOV were calculated by using the SPICE kernel, and thus the selected spectra should mostly include effective events such as solar flare events. The correlation coefficient for selected spectra between the solar X-ray events from the standard sample and the X-ray events from Itokawa was 0.57. It implies that the standard sample and observed Itokawa spectra were mostly correlated but they included some noises. The integration time of selected data, plotted on the shape model of Itokawa (Demura *et al.*, 2006), are schematically shown in Figure 8.4. The variations in the incident and emission X-ray angles were caused by changes of the geometry of the surface on Itokawa, where observed faces were calculated by the SPICE kernel. The sunlit areas were selected under a condition that the angle was less than 90° between the normal vector of a polygon face and the positional vector of the Sun (Itokawa coordinate) of polygon mesh (triangle).

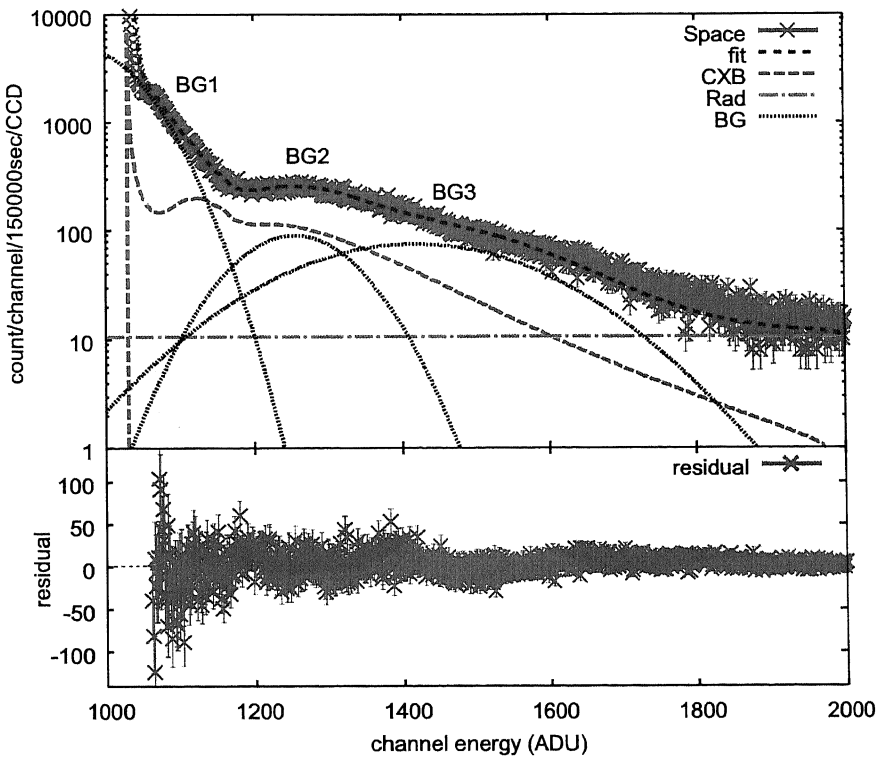

Figure 8.2: The integrated spectrum taken when Itokawa was out of view of XRS (150000 seconds). The backgrounds were assumed to be X-ray events as a sum of CXB and NXB, and assumed to be instrumental backgrounds expressed as Gaussians (BG1, BG2, and BG3). The possible cause of these backgrounds were fake events due to fluctuations of dark current or hot-pixels, and instrumental noise.

Table 8.1: **The best-fit results of instrumental backgrounds.**

Background	Intensity count/sec/CCD	Peak center (channel)	standard deviation (channel)
BG1	6.670 ± 0.007	1003.8 ± 0.3	86.5 ± 0.1
BG2	0.156 ± 0.001	1255.5 ± 0.4	104.273975 ± 0.1
BG3	0.277 ± 0.001	1418.4 ± 0.8	222.371174 ± 0.1

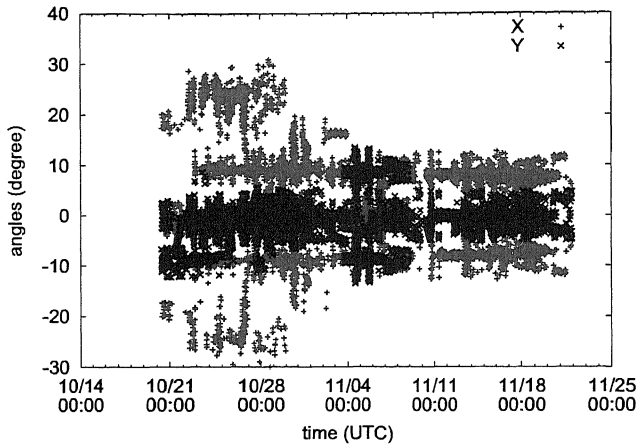

Figure 8.3: The Sun angles in the Hayabusa coordinate system (see also Figure 3.2). This figure indicates angles between the standard sample and the Sun. The effective data were the data in the quadrant X>0 and Y>0 in the Hayabusa coordinate system.

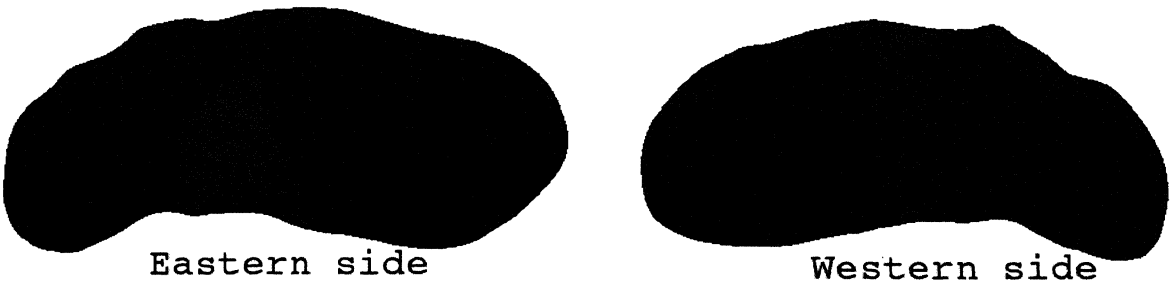

Figure 8.4: Observed areas of XRS plotted on the shape model of Itokawa called Aizu 5.04 (Demura et al., 2006). Red colored points indicate points with long integration times. For example, the reddest points have the longest observation time of 9300 seconds

8.2.2 Estimation of Solar X-rays

In order to estimate incident solar X-rays, the spectra of the standard sample were analyzed. The observed spectra of the standard sample were simultaneously obtained with the observed spectra of Itokawa. The X-ray models were described in Chapter 4. They were analyzed by the models of solar X-ray, fluorescent X-ray, and scattering X-ray. Since solar activity varied in time, one MEKAL model could not fit to the observed spectrum in the all energy range. Thus the blend model of two MEKAL models was used as a soft energy spectrum $J_1(E)$ and a

hard energy spectrum $J_2(E)$, and then solar X-ray spectrum J in Equations 4.3 and 4.4 were rewritten as $J = n_1 J_1 + n_2 J_2$, where n_1 and n_2 were proportionality constants used as free parameters for the fitting.

The free parameters for the fitting were the intensities and temperatures of solar X-rays for two MEKAL models (four parameters). The intensities, peak centers, and standard deviations of three instrumental backgrounds were free parameters (3 Gaussians: 9 parameters). Also, intensity of NXB was a free parameter (constant: one parameter). In contrast, the fixed parameters were the elemental mass fractions of the standard sample (Table 3.1).

The initial values for free parameters of the plasma temperatures and intensities were estimated by the data of GOES X-ray flux levels as shown in Figure 7.3. They were used in Equation 4.1 for the GOES flux and transformed to the plasma temperatures for a solar flare condition and a typical quiet condition during observation period. Also, the initial values for free parameters of the backgrounds were the same as the background values, estimated in previous section.

Figure 8.5 shows the best-fit model spectrum for the observed spectrum of the standard sample. Shown are the observed spectrum together with counting statistics errors (*e.g.*, Knoll, 2000), the best-fit fluorescence line spectra convolved with the response function of XRS, the best-fit scattering continuum spectrum convolved with the response function of XRS, best-fit NXB spectrum as backgrounds, and the best-fit three instrumental backgrounds. The best-fit results of solar X-ray model for the observed spectrum of the standard sample are shown in Table 8.2.

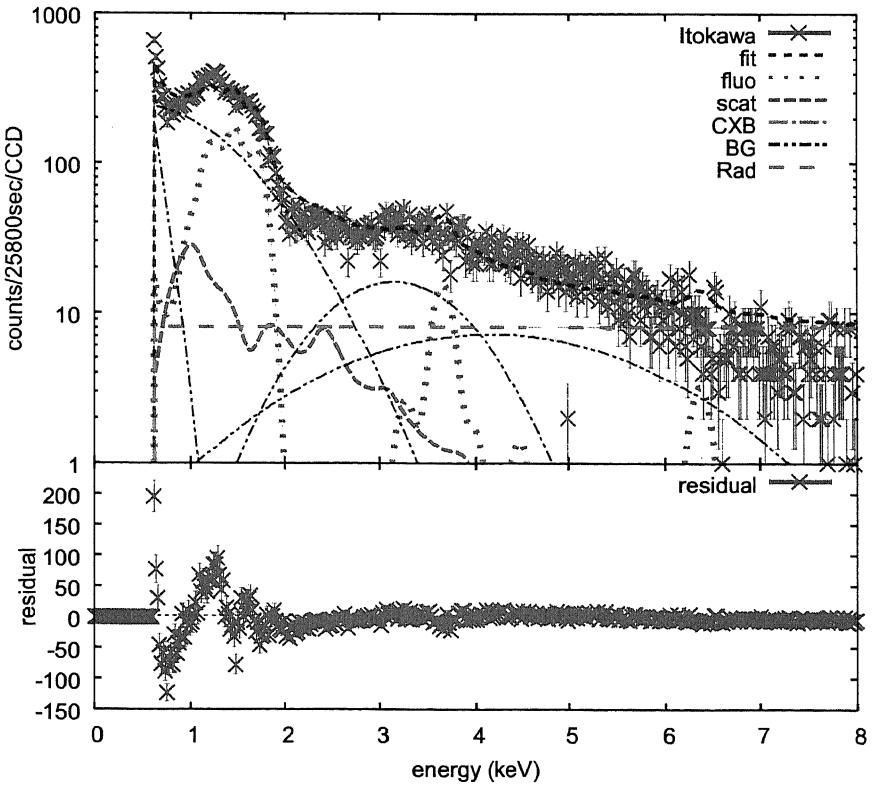

Figure 8.5: The best-fit model spectrum for the observed spectrum of standard sample. Shown are the observed spectrum together with counting statistics errors, the best-fit fluorescence line spectra convolved with the response function of XRS, the best-fit scattering continuum spectrum convolved with the response function of XRS, best-fit NXB spectrum as backgrounds, and the best-fit three instrumental backgrounds.

Table 8.2: **Results of fitting to observed solar X-ray spectrum.**

intensity ratios	Temperature (MK)	
	Soft	Hard
0.0160 ± 0.006	6.23 ± 0.04	16.90 ± 0.07

8.2.3 Estimation of elemental composition of Itokawa

The procedure for the analysis of Itokawa data is basically the same as the estimation of solar X-ray model as given in previous section except one free parameter and one background.

Free parameters for the fitting are elemental mass fractions, $w_{\rm Mg}$, $w_{\rm Al}$, $w_{\rm Si}$, $w_{\rm S}$, $w_{\rm Ca}$, and $w_{\rm Fe}$ (6 parameters). Also, the parameters of NXB and three instrumental backgrounds lead to ten free parameters (1+9 parameters) like in the estimation of solar X-rays. The ratios of CXB in the observed spectra were calculated by the SPICE kernel. The fixed parameters are the plasma temperatures estimated in the previous section. The elemental mass fractions of other elements were fixed to averages for ordinary chondrites. Elemental mass fraction for all the elements were normalized and recalculated during the fitting iteration as follows,

$$\sum w_i = 100\%.$$

Also, the mass fraction of $w_{\rm O}$ was complemented with oxide ratios, using the atomic ratios of MgO, Al_2O_3, SiO_2, CaO, and FeO. Also a metallic Fe and FeO ratio was assumed and fixed to be $\sim$ 1:1 for low Iron groups by Urey–Craig relation (Urey and Craig, 1953).

Initial elemental mass fractions for the fitting of X-ray model of Itokawa were assumed to be average composition of ordinary chondrites (Jarosewich, 2006; Yanai and Kojima, 1995) as shown in Table 8.3, including the average values for 229 samples of H-chondrites, for those of 256 samples of L-chondrites, and for those of 83 samples LL-chondrites with each standard deviation.

Figure 8.6 shows the best-fit model spectrum for observed spectrum of Itokawa. Shown are the observed spectrum together with counting statistics errors, the best-fit fluorescence line spectra convolved with the response function of XRS, the best-fit scattering continuum spectrum convolved with the response function of XRS, CXB spectrum convolved with the response function of XRS as background, best-fit NXB spectrum as backgrounds, and the best-fit three instrumental backgrounds.

Table 8.3: Average elemental composition of ordinary chondrites (wt.%).

element	H (229)	L (256)	LL (83)
H	0.11 ± 0.09	0.04 ± 0.07	0.06 ± 0.11
C	0.03 ± 0.08	0.07 ± 0.19	0.04 ± 0.11
O	34.51 ± 1.68	36.96 ± 1.02	38.49 ± 1.27
Na	0.56 ± 0.08	0.66 ± 0.08	0.69 ± 0.08
Mg	14.13 ± 0.51	15.11 ± 0.42	15.39 ± 0.59
Al	1.19 ± 0.23	1.26 ± 0.20	1.37 ± 0.35
Si	16.55 ± 0.60	18.21 ± 0.49	18.58 ± 0.89
P	0.11 ± 0.05	0.12 ± 0.04	0.12 ± 0.05
S	2.10 ± 0.43	2.24 ± 0.41	2.10 ± 0.57
K	0.07 ± 0.02	0.08 ± 0.02	0.09 ± 0.02
Ca	1.17 ± 0.14	1.29 ± 0.11	1.34 ± 0.15
Ti	0.05 ± 0.02	0.06 ± 0.02	0.07 ± 0.02
Cr	0.30 ± 0.23	0.34 ± 0.24	0.33 ± 0.07
Mn	0.22 ± 0.05	0.25 ± 0.04	0.25 ± 0.04
Fe	27.28 ± 1.96	22.07 ± 1.28	20.12 ± 1.79
Co	0.06 ± 0.02	0.05 ± 0.02	0.03 ± 0.02
Ni	1.52 ± 0.23	1.15 ± 0.15	0.93 ± 0.27
total	99.96	99.96	100.00

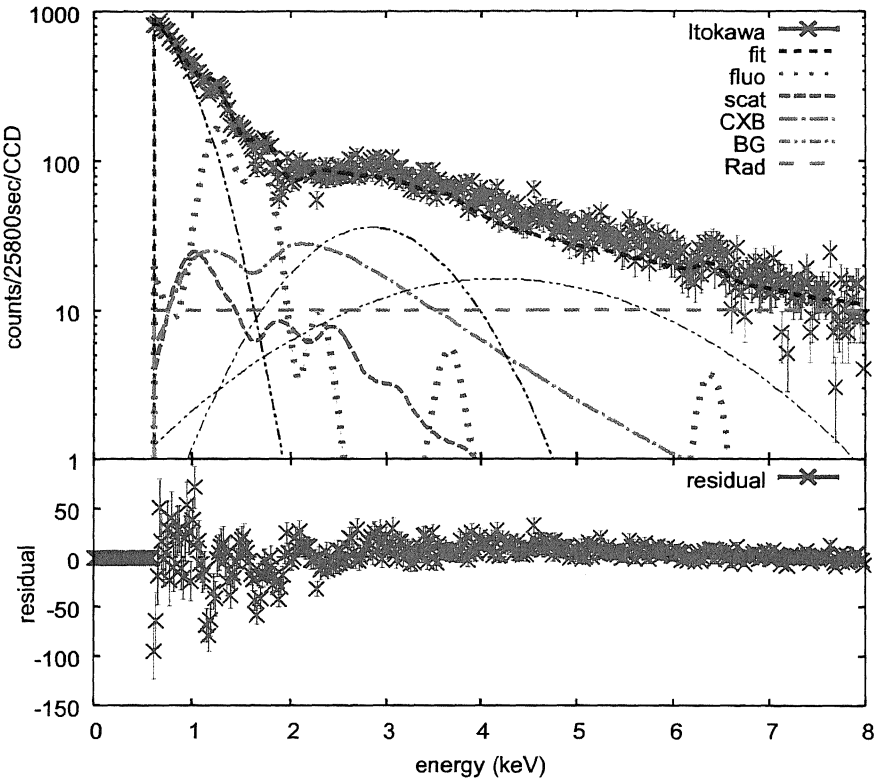

Figure 8.6: The best-fit model spectra for the observed spectrum of Itokawa. Showni are the observed spectrum together with counting statistics errors, the best-fit fluorescent line spectra convolved with the response function of XRS, the best-fit scattering continuum spectrum convolved with the response function of XRS, CXB spectrum convolved with the response function of XRS as background, best-fit NXB spectrum as backgrounds, and the best-fit three instrumental backgrounds.

8.3 Results

There are three important points in our results, (1) calibration curve, (2) error propagations, and (3) the best fit-results, as described bellow.

8.3.1 Calibration curve

The calibration curve was calculated for the observed spectrum of Itokawa, comparing the observed peak center (channel) with the energy of X-ray fluorescence lines for Mg-Kα (1.25 keV), Si-Kα (1.74 keV), and Fe-Kα (6.40 keV) with liner curve fitting as follows,

$$\text{peak center} = \text{gain} \times \text{E} + \text{ offset},$$

where gain was a conversion factor from energy to digital unit and offset was a correction constant. The best-fit value of offset was shifted to a lower energy compared to pre-launch tests (at -53$\pm$1 degree Celsius) as shown in Table 8.4. The cause of offset shift is probably degradation of CTE (charge transfer efficiency) which causes the loss of charges (X-ray signal).

Table 8.4: **Calibration curve of pre-launch and the Itokawa observation data.**

	pre-launch (-53±1 deg C)	the Itokawa observation (-52±2 deg C)
gain (channel/keV)	100.75 ± 0.44	101.14 ± 0.27
offset (channel)	997.79 ± 1.68	994.53 ± 1.04

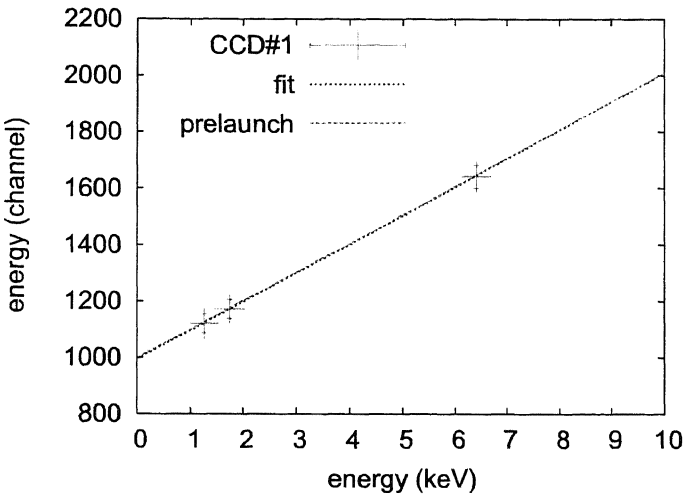

Figure 8.7: Calibration curve, Mg-Kα (1.25 keV), Si-Kα (1.74 keV), and Fe-Kα (6.40 keV) line peaks were found in the observed spectrum of Itokawa. The measured offset was lower than that of pre-launch test (at -53±1 degree Celsius) probably due to degradation of charge transfer efficiency.

8.3.2 Error propagations

The best-fit elemental mass fractions did not include instrumental systematic errors (Table 5.6) and solar X-ray estimation errors as shown in Table 8.5. The systematic errors Δs_i for element i and the solar X-ray estimation error ΔJ as a function of energy are written as the errors for X-ray intensities with Equation 4.3 as follows,

$$I_i \pm \Delta I_i^{\rm sys} = (s_i \pm \Delta s_i)\frac{\Omega S}{4\pi}\int \frac{\omega_i p_i j_i t_i w_i \tau_i(E) J}{\sum_j \left(w_j \mu_j(E) + w_j \mu_j(E_i^{\rm f})\frac{\cos\phi_1}{\cos\phi_2}\right)} dE, \tag{8.1}$$

also, the error of solar X-ray estimation is written as follows,

$$I_i \pm \Delta I_i^{\rm sol} = \frac{\Omega S}{4\pi}\int \frac{\omega_i p_i j_i t_i w_i \tau_i(E)(J \pm \Delta J)}{\sum_j \left(w_j \mu_j(E) + w_j \mu_j(E_i^{\rm f})\frac{\cos\phi_1}{\cos\phi_2}\right)} dE. \tag{8.2}$$

If two kinds of errors are assumed to be independent of each other, the total error ΔI_i for element i is propagated as follows,

$$\Delta I_i = \sqrt{(\Delta I_i^{\rm sys})^2 + (\Delta I_i^{\rm sol})^2}. \tag{8.3}$$

Since observed data do not directly represent the elemental mass fraction but the X-ray intensity, it is necessary to transform the errors of observed X-ray intensity ΔI_i for element i to

the errors of mass fraction Δw_i for element i by using the differential Equation 4.3 as follows,

$$\Delta I_i \sim \sum_j \frac{\partial I_i}{\partial w_j} \Delta w_j, \tag{8.4}$$

where w_i is the observed mass fraction, and Δw_i is the error of observed mass fraction for element i. This equation can be solved by using a matrix inversion (6×6 matrix). Table 8.5 shows the solar X-ray estimation errors for each element. Here, the errors of secondary fluorescent X-rays are neglected because these errors for each element are less than 1%.

Table 8.5: Solar X-ray estimation errors (%)

Element	Mg	Al	Si	S	Ca	Fe
Error of solar X-ray	3.4	3.8	3.6	4.4	5.2	5.9

8.3.3 Elemental mass fractions of Itokawa

Table 8.6 shows the best-fit elemental mass fractions of Itokawa (Global). The errors indicate the standard error for the fitting, including the errors of counting statistics and the errors of models. Also, Table 8.7 shows the error propagation results, including solar X-ray estimation errors measured in previous section (random error) and estimation errors for instrumental characteristics (systematic error). These results resemble the average elemental composition of ordinary chondrites (Table 8.3) within the errors but the ratio of Fe appears to be a little rich.

Table 8.6: The results of best-fit elemental ratio of Itokawa (Global).

Mg (wt%)	Al (wt%)	Si (wt%)	S (wt%)	Ca (wt%)	Fe (wt%)
15.31 ± 0.32	1.79 ± 1.02	17.99 ± 0.68	2.44 ± 1.06	2.41 ± 1.29	25.13 ± 1.18

Table 8.7: The results of best-fit elemental ratio of Itokawa (error propagated)

Error	Mg (wt%)	Al (wt%)	Si (wt%)	S (wt%)	Ca (wt%)	Fe (wt%)
Random	15.31 ± 0.99	1.79 ± 1.03	17.99 ± 1.35	2.44 ± 1.08	2.41 ± 1.31	25.13 ± 2.92
Random & Systematic	15.31 ± 1.53	1.79 ± 1.04	17.99 ± 2.53	2.44 ± 1.12	2.41 ± 1.33	25.13 ± 4.76

Chapter 9

Analysis of Locally Observed Spectra

In this chapter, analysis methods and results for the major elemental composition at the local areas of Itokawa are described, and the major elemental compositions, such as Mg, Al, Si, S and their regional variations are estimated.

9.1 Method of analysis

In order to estimate the elemental mass fractions of Itokawa, least squares-fits were used to compare the observed spectrum with the model spectrum in the same way as in the global analysis described in Chapter 8.

Unfortunately, solar activity was low throughout the observation period and XRS did not carry out long time pointing to Itokawa due to failure of reaction wheels. Fortunately, during the early time of TD#1 phase, solar flare events were observed by the GOES 10 and 12 satellites, and then the solar monitor of XRS also sensed solar flare events. This indicates that solar activity was relatively enhanced at Itokawa, the opposite side of the Sun from the Earth. This period is the decent phase, and then the spectral background is relatively large due to increasing of dark current.

9.2 Analysis of observed spectra

In order to estimate the elemental mass fractions of Itokawa, backgrounds of observed spectra were assumed, and least squares-fit of the model spectrum and the observed spectrum were performed as follows: (1) The backgrounds in observed spectra were assumed. (2) The solar X-ray model was estimated by analysis of the observed spectra of the standard sample. (3) The elemental mass fraction on the surface materials of Itokawa were estimated by using the observed spectra of Itokawa.

9.2.1 Assumption of spectral backgrounds

The same spectral background used in Chapter 8 for the global analysis of observation except for the absence of CXB events as backgrounds. The local observation data included Itokawa within the view of XRS in all times, and thus the X-rays from CXB were not observed. This observation period was the decent phase to Itokawa when thermal changes of CCDs occurred (November 19, 2005 in Figure 7.4) and caused the increasing of dark current. Thus the background in this period is larger than the typical background estimated for global observation in Chapter 8. The spectral backgrounds were assumed to be not Gaussian but an exponential function. The event counts of instrumental backgrounds are relatively low compared to global estimation in

Chapter 8 due to short integration times. The event counts included instrumental noises, such as the distribution of dark current, the distribution of hot-pixels, and background subtraction noise due to logic errors of hardware.

The Hayabusa spacecraft descended along the equatorial plane of Itokawa from west to east with Itokawa rotating with the period of 12 hours and the observed surface areas of Itokawa varied between 20386 m^2 and 6111 m^2 in the distance of 0.94 km to 0.38 km. The off-normal angle of the Sun to the standard sample was less than 10°, and then the off-normal angle of CCD#4 to the standard sample was fixed at 45°. Also the Sun-to-Itokawa-to-XRS was less than 10° but the incident and emission X-ray angles varied due to surface geometry for the observed planes between 0° and 90°. Table 9.1 shows observation start time, observed area, average incident and emission angles for 10 observed areas called a facet.

Temporal changes of the observed phase angle caused the apparent changes of the elemental composition ratio, which needs to be corrected by using a precise surface geometry. In addition, X-ray incident and emission angles also affect the spectral shape. These angles were calculated at each part of the asteroid surface by using the shape model of Itokawa (Demura *et al.*, 2006) by the SPICE kernel as shown in Figure 9.1.

The integration time was 1800 seconds for each spectrum in order to obtain statically significant counts of X-ray photons. Over 100 photons are needed to achieve 10% errors in counting statistics (Knoll, 2000).

Table 9.1: Observational condition for the standard sample and Itokawa

	standard sample			Itokawa				
Observation start time (UTC)	Area (cm^2)	Incident angle ϕ_1 (deg)	Emission angle ϕ_2 (deg)	Facet number	Lon. (deg)	Area (m^2)	Incident angle ϕ_1 (deg)	Emission angle ϕ_2 (deg)
12:02:11		0.0		1	306.3	20386	31.0	-29.5
12:39:52		0.0		2	296.0	18683	27.6	-27.5
13:17:30		-0.2		3	285.3	17939	27.2	-29.8
13:55:12		-7.4		4	272.5	17962	30.8	-36.6
14:32:53	14.76	0.1	-45.0	5	259.9	16408	42.2	-49.1
15:10:37		-0.2		6	251.6	13985	56.0	-62.6
15:48:20		2.6		7	237.6	9595	67.2	-73.8
16:26:04		0.1		8	221.3	8606	46.6	-53.3
17:03:48		-2.7		9	184.8	7429	21.3	-25.4
17:41:32		0.1		10	168.9	6111	43.1	-36.2

(a) The Sun angle for the standard sample

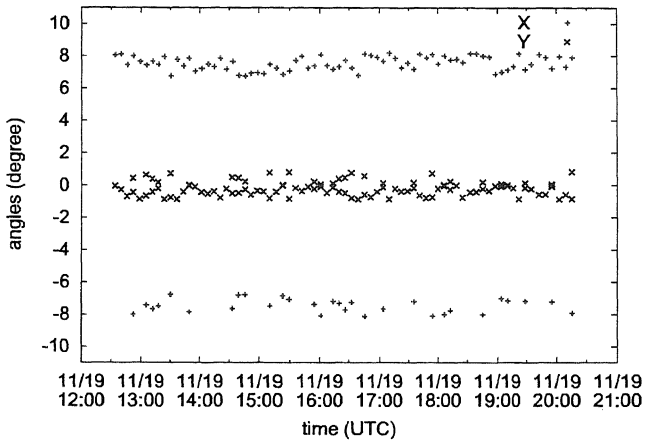

(b) phase angle of the Sun–XRS–Itokawa

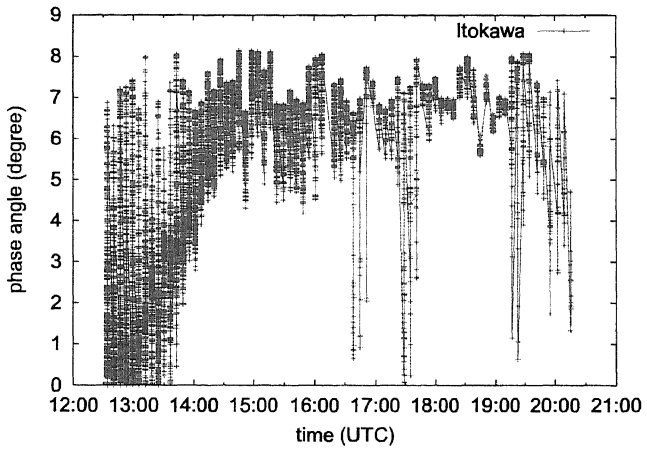

Figure 9.1: (a) The Sun angle for the standard sample in the Hayabusa coordinate system obtained from the SPICE kernel. (b) Phase angle of the Sun–XRS–Itokawa obtained from the SPICE kernel.

9.2.2 Estimations of solar X-rays

In order to estimate solar X-rays, the model fitting was performed by using the fitting function of fluorescent and scattering X-rays in Equations 4.3 and 4.4, respectively, and then these functions were convolved with the response function. Since solar activity varied from time to time, a single MEKAL model could not fit well to the observed spectrum in the all energy range. Thus, the blend model of two MEKAL models was used as a sum of a soft energy spectrum $J_1(E)$ and a hard energy spectrum $J_2(E)$, and then solar X-ray spectrum J are rewritten as $J = n_1 J_1 + n_2 J_2$, where n_1 and n_2 are proportionality constant used as a free parameter for fitting.

Elemental composition of the standard sample was fixed in this calculation as shown in Table 3.1. The sulfur abundance of the standard sample is almost equal to zero because it was vaporized in the manufacturing process.

The incident angle ϕ_1 and emission angle ϕ_2 in Equations 4.3 and 4.4 are shown in Table 9.1 (only average angles for 1800 seconds observation are indicated). Free parameters were n_1, n_2, solar coronal temperatures of the MEKAL models, and standard deviation of Gaussian-like response function. Also, the proportional constants and exponential backgrounds were free

parameters.

Since the standard sample is a glass plate whose composition is almost homogeneous, apparent changes of X-ray intensities due to surface roughness or mineral composition are negligible.

The example of the best-fit X-ray model for the observed spectrum of the standard sample is shown in Figure 9.2. The peaks of Mg-Kα (1.25 keV) and Si-Kα (1.74 keV) were found but those of Al-Kα (1.49 keV) and S-Kα (2.31 keV) were not found due to lower composition ratio in the standard sample. Also, an unexplained peak was found at the energy of 2.1 keV. This peak is near the P-Kα (2.01 keV) line or the Au-Mα (2.12 keV) line. The abundance of P on the standard sample is too low to be detected (see Table 1) for this solar condition or this integration time. Although Au is not present in the standard sample, it is used for a meshed support frame of the beryllium X-ray window (the optical shield). Since the X-ray intensities from P-K or Au-M, excited by X-rays from Itokawa, are faint, this peak is probably instrumental noise. The instrumental noise is described in Chapter A.

In this observation period, solar temperature fluctuated between 3.9 MK and 4.5 MK in the soft energy range, and between 13.5 MK and 15.7 MK in the hard energy range. The maximum temperature was equivalent to the solar flare levels of C2 (GOES's web site), estimated with Equation 4.1. This flare level is high enough to estimate sulfur abundance to be less than 10% counting statistical errors. However, space radiation or instrumental background raises the level of noise, and thus the results include large errors.

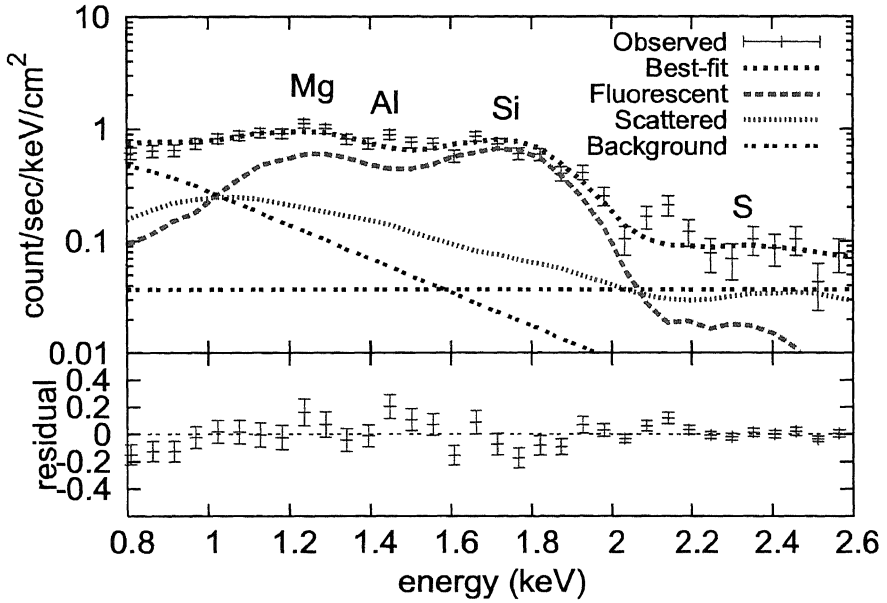

Figure 9.2: The observed X-ray spectra of the standard sample are shown together with the fitted spectra. The example of best-fit X-ray model spectra is compared to observed spectrum of the standard sample (facet #10). Red points indicate the observed spectrum with counting statistic errors. Blue line indicates the best-fit spectrum. Green line indicates X-ray fluorescence model spectrum and pink line indicates scattering X-rays model spectrum. Black lines indicate the background spectra of instrument and space radiation. All the model functions are convolved with Gaussian-like response of XRS. Fitted peaks are found in the energy of Mg-Kα (1.25 keV), Si-Kα (1.74 keV) but peaks of Al-Kα (1.49 keV) and S-Kα (2.31 keV) are not found due to faintness. Also, an unexplained peak is found at the energy of about 2.1 keV. In this period, the best-fit model to the solar plasma temperatures for observed spectra are to be between 13.5 and 15.7 MK in the hard energy.

Table 9.2: **Results of the analysis for standard sample and Itokawa.**

Facet	J_2 / J_1	plasma temperature (MK)	
number	intensity ratio	soft	hard
1	0.00106 ± 0.00002	4.56 ± 0.03	13.72 ± 0.03
2	0.00126 ± 0.00003	4.08 ± 0.06	13.53 ± 0.04
3	0.00107 ± 0.00004	3.92 ± 0.07	13.78 ± 0.02
4	0.00173 ± 0.00004	4.28 ± 0.06	14.35 ± 0.04
5	0.00160 ± 0.00001	4.41 ± 0.03	15.73 ± 0.02
6	0.00164 ± 0.00002	4.16 ± 0.03	15.26 ± 0.02
7	0.00172 ± 0.00002	4.50 ± 0.03	15.52 ± 0.02
8	0.00162 ± 0.00007	4.22 ± 0.11	14.11 ± 0.07
9	0.00182 ± 0.00002	4.37 ± 0.01	14.36 ± 0.02
10	0.00198 ± 0.00010	4.36 ± 0.06	14.88 ± 0.06

9.2.3 Estimations of elemental composition of Itokawa

The model of fluorescent and scattering X-rays from the surface materials of Itokawa is calculated with basically the same method as for the estimation of solar X-rays. Since the solar coronal temperatures could derive the best-fit results of solar X-ray estimation, an undetermined parameter is the elemental composition of Itokawa.

Initial elemental mass fractions for the fitting of the X-ray model of Itokawa were assumed to be the average elemental composition of ordinary chondrites in the same way as in the global analysis given in Chapter 8.

Free parameters for the fitting were elemental mass fractions of w_{Mg}, w_{Al}, w_{Si}, and w_{S}. Mass fractions of other elements were fixed to the average values of ordinary chondrites because observed peaks were faint, such as Ca, Fe, and ..., in this solar condition. All mass fractions for each element were normalized and recalculated during the fitting iteration as follows,

$$\sum w_i = 100\%.$$

Also, the ratio of w_{O} was complemented with oxide ratios, using atomic ratios of MgO, Al_2O_3, and SiO_2.

Variation of geometry apparently causes the intensity changes of X-rays. Figure 9.3 shows the X-ray intensity ratios calculated for fluorescent X-rays from polygon planes model compared to those from a single plane model in the sunlit areas for 10 facets. In particular, apparent changes for elemental abundance of Fe due to geometry variation are relatively large. Since almost all abundance of sulfur is in the form of Troilite (FeS) in asteroids, this geometry correction is important for sulfur estimation.

The example of the best-fit X-ray model for the observed spectrum of Itokawa is shown in Figure 9.4. An unexplained peak, found in the spectra of the standard sample, is also found in the spectra of Itokawa. Line peaks of Mg and Si are also found but intensities of these peaks are relatively small probably due to the condition of the surface materials, such as roughness. In general, a rough surface tends to decrease the intensities of X-ray emissions. Since the standard sample is the glass plate, X-rays from the standard sample are relatively large compared to those from the rough surface of Itokawa. Additionally, the instrumental backgrounds of the asteroid detector were large relative to the solar monitor. The exponential function as a spectral

background implies that the instrumental degradation due to space irradiation is increasing. Spectral backgrounds of these observed spectra were large, these peak heights of Al to Si and S to Si vary with 10 facets. Figure 9.5 and 9.6 show the best-fit spectra for 10 facets.

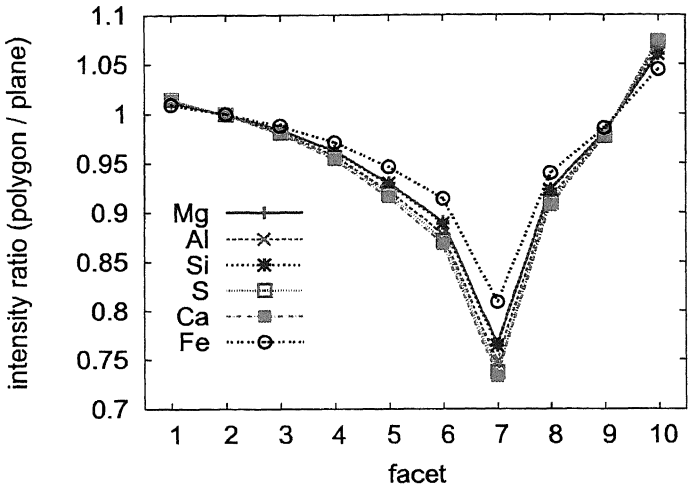

Figure 9.3: Intensity ratios of a polygon model to a plane model for X-ray fluorescence lines of Mg, Al, Si, S, Ca, and Fe at 10 facets. Fluorescent X-rays from polygon model are calculated by using the shape model of Itokawa (Demura *et al.*, 2006). The parameters were the incident and emission X-rays angles and areas of polygon faces. Also fluorescent X-rays from a single plane are calculated, assuming the same effective area as polygon model but incident and emission angles (0°) were fixed. In particular, the ratio of Fe varies largely relative to that of other elements. Since almost all abundance of sulfur is in the form of Troilite (FeS), the correction of geometry is important for the sulfur estimation.

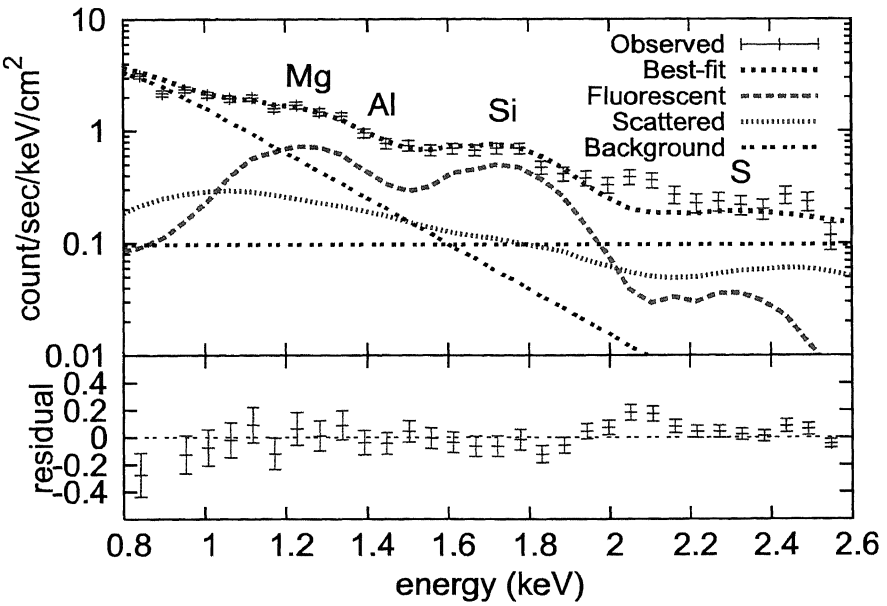

Figure 9.4: The observed X-ray spectra of Itokawa are shown together with the fitted spectra. It is the example of best-fit X-ray model spectra for the observed spectrum of Itokawa (facets #10). Same energy peaks are found as Figure 9.2. Al and S peaks of Itokawa are faint, and these X-ray intensities vary with the 10 facets. Since the backgrounds raise the level of spectral signals, the results include large errors.

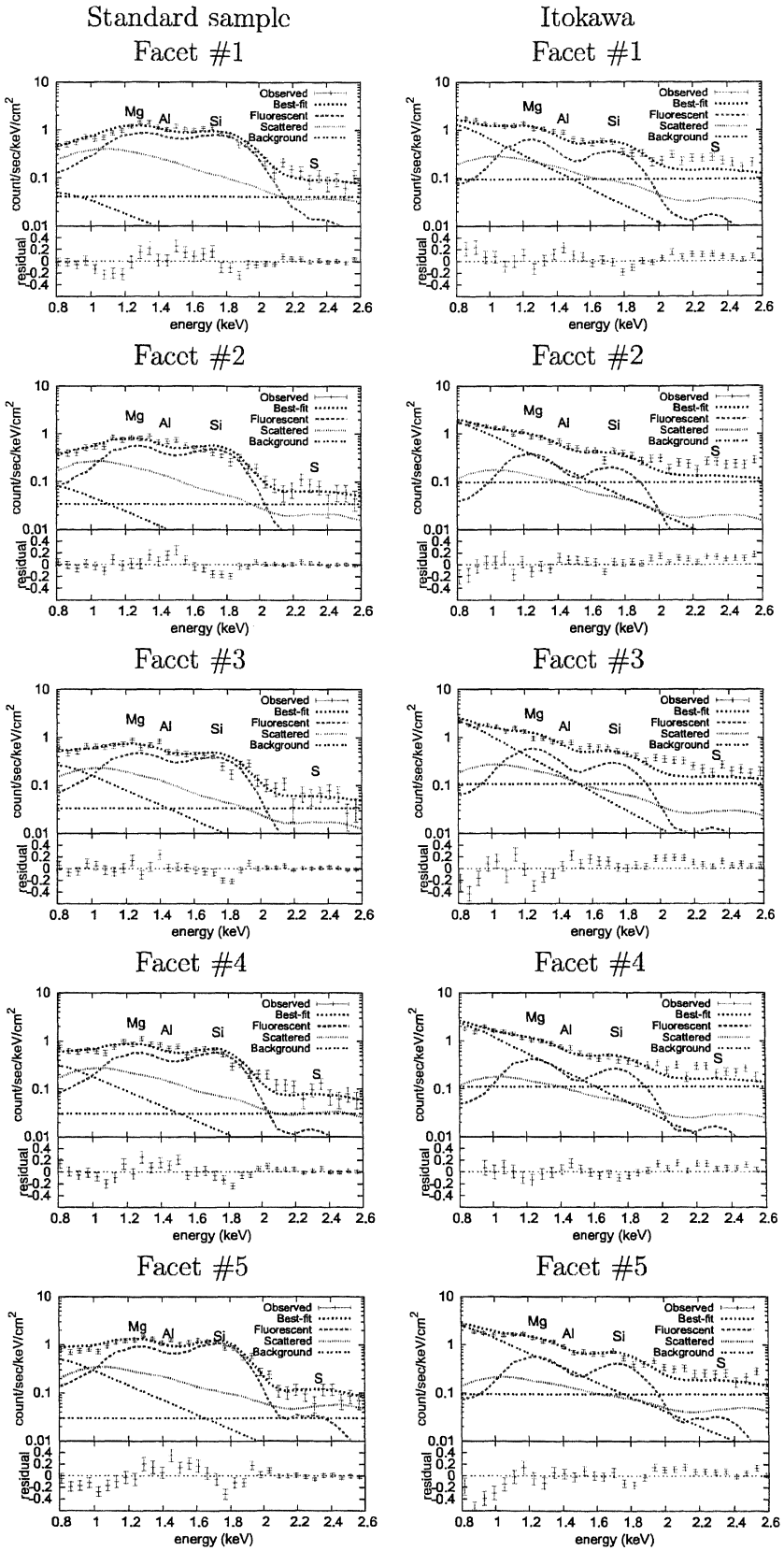

Figure 9.5: Best-fit model spectra to observed spectra in TD#1 (Facet #1-#5).

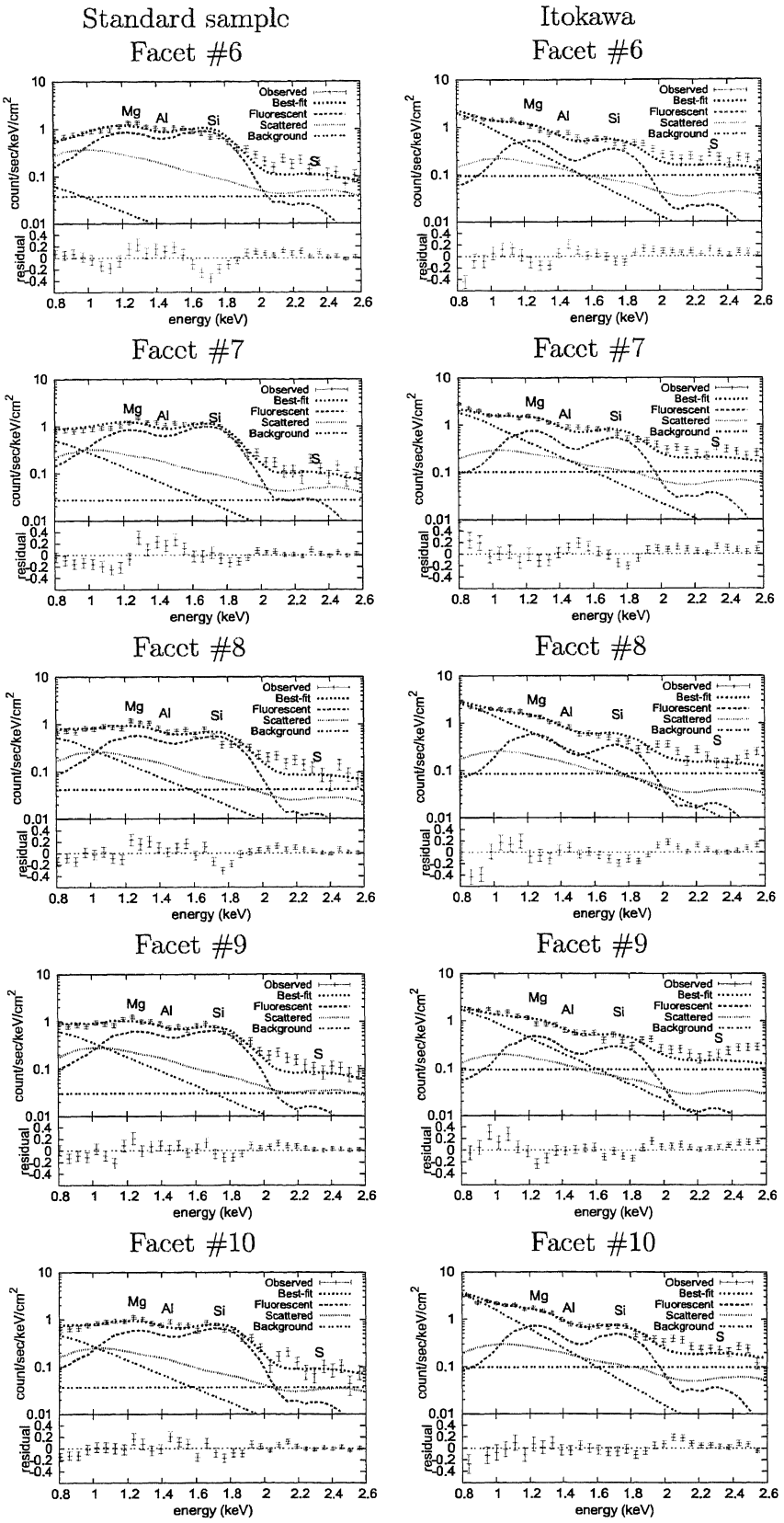

Figure 9.6: Best-fit model spectra to observed spectra in TD#1 (Facet #6-#10).

9.3 Results

The mass fraction of major elements, Mg, Al, Si, and S, on the surface of Itokawa at 10 local areas were estimated, where the temporal fluctuation of solar X-rays, geometry variation of local areas, and sensor response function were corrected for 10 spectra.

It is necessary to the systematic and random errors to the best-fit results. The same error propagation method used in Chapter 8 for the globally observed spectra was also used in this analysis. Table 9.3 shows solar X-ray estimation errors.

Table 9.4 shows best-fit mass fractions of Itokawa at 10 facets. The error propagated elemental mass fractions of Itokawa at 10 facets are shown in Table 9.5, including systematic and solar X-ray estimation errors. The mass fractions for Mg, Al, Si and S are shown with the standard errors propagated with model-fit errors, counting statistics errors, and estimation errors of solar X-rays.

The elemental mass fractions of Mg and Si appear to be regionally homogeneous but the best-fit elemental mass fractions of Al and S vary at local areas as shown in Figure 9.7. Also, the best-fit mass fractions of S are shown in Figure 9.8, plotted on the shape model of Itokawa (Demura *et al.*, 2006). The area with the lowest sulfur abundance is found at facet #9 accompanied with rich aluminum. This area is close to a large cratered area with many high albedo sites called Arcoona (*e.g.*, in Figure 3 of Demura *et al.*, 2006), the top of elongated asteroid. The color indicates the mass fractions of sulfur abundance between 1.8 and 2.6 (wt.%). Although the distribution of Mg and Si abundance is homogeneous (see Table 9.5), the best-fit sulfur abundances vary at local areas.

The elemental mass fractions of Mg and Si are similar to average elemental composition of ordinary chondrites. Although upper estimates of abundances for Al and S are far larger than average elemental composition of ordinary chondrites, this abundance is within that of mass variation of ordinary chondrites. Thus, the major elemental composition on the surface of Itokawa resembles that of ordinary chondrites.

Table 9.3: Solar X-ray estimation errors for each element.

facet number	Mg (%)	Al (%)	Si (%)	S (%)
1	0.8	1.8	0.8	3.1
2	1.5	2.3	1.5	4.5
3	1.1	1.9	1.2	3.7
4	2.0	2.9	2.1	4.0
5	1.2	4.5	1.4	1.8
6	1.5	2.2	1.5	2.7
7	0.7	5.7	0.8	1.3
8	1.1	7.6	1.3	2.3
9	1.3	1.2	1.3	4.7
10	1.2	1.8	1.1	1.5

Table 9.4: **Best-fit mass fractions of Itokawa together with 1σ errors.**

facet number	Mg (wt%)	Al (wt%)	Si (wt%)	S (wt%)
1	15.01 ± 0.04	1.75 ± 0.11	17.99 ± 0.05	2.40 ± 0.25
2	14.99 ± 0.08	1.71 ± 0.13	18.02 ± 0.09	2.40 ± 0.36
3	15.01 ± 0.06	1.83 ± 0.12	18.01 ± 0.07	2.13 ± 0.26
4	15.11 ± 0.10	1.48 ± 0.14	18.02 ± 0.13	2.45 ± 0.33
5	15.09 ± 0.06	1.49 ± 1.10	17.98 ± 0.08	2.54 ± 0.15
6	15.18 ± 0.07	1.59 ± 0.12	17.95 ± 0.09	2.24 ± 0.20
7	15.07 ± 0.03	1.98 ± 0.37	18.00 ± 0.05	2.34 ± 0.10
8	15.28 ± 0.06	1.64 ± 0.42	17.81 ± 0.08	2.44 ± 0.18
9	15.16 ± 0.07	2.43 ± 0.10	17.88 ± 0.08	1.86 ± 0.29
10	15.19 ± 0.06	1.59 ± 0.09	17.78 ± 0.07	2.54 ± 0.13

Table 9.5: Best-fit results of mass fractions for 10 facets (error propagated).

Error	facet number	Mg (wt%)	Al (wt%)	Si (wt%)	S (wt%)
Random	1	15.01 ± 0.54	1.75 ± 0.11	17.99 ± 1.12	2.40 ± 0.25
	2	14.99 ± 0.69	1.71 ± 0.14	18.02 ± 1.62	2.40 ± 0.36
	3	15.01 ± 0.57	1.83 ± 0.13	18.01 ± 1.33	2.13 ± 0.26
	4	15.11 ± 0.88	1.48 ± 0.15	18.02 ± 1.45	2.45 ± 0.33
	5	15.09 ± 1.36	1.49 ± 1.10	17.98 ± 0.65	2.54 ± 0.15
	6	15.18 ± 0.67	1.59 ± 0.13	17.95 ± 0.97	2.24 ± 0.20
	7	15.07 ± 1.72	1.98 ± 0.37	18.00 ± 0.47	2.34 ± 0.10
	8	15.28 ± 2.32	1.64 ± 0.42	17.81 ± 0.82	2.44 ± 0.18
	9	15.16 ± 0.37	2.43 ± 0.12	17.88 ± 1.68	1.86 ± 0.29
	10	15.19 ± 0.55	1.59 ± 0.10	17.78 ± 0.54	2.54 ± 0.13
Random and Systematic	1	15.01 ± 1.44	1.75 ± 0.22	17.99 ± 2.64	2.40 ± 0.37
	2	14.99 ± 1.50	1.71 ± 0.23	18.02 ± 2.90	2.40 ± 0.45
	3	15.01 ± 1.45	1.83 ± 0.24	18.01 ± 2.75	2.13 ± 0.35
	4	15.11 ± 1.60	1.48 ± 0.22	18.02 ± 2.80	2.45 ± 0.44
	5	15.09 ± 1.91	1.49 ± 1.11	17.98 ± 2.48	2.54 ± 0.32
	6	15.18 ± 1.50	1.59 ± 0.22	17.95 ± 2.58	2.24 ± 0.32
	7	15.07 ± 2.18	1.98 ± 0.43	18.00 ± 2.44	2.34 ± 0.28
	8	15.28 ± 2.69	1.64 ± 0.46	17.81 ± 2.51	2.44 ± 0.33
	9	15.16 ± 1.39	2.43 ± 0.29	17.88 ± 2.92	1.86 ± 0.36
	10	15.19 ± 1.45	1.59 ± 0.20	17.78 ± 2.43	2.54 ± 0.31

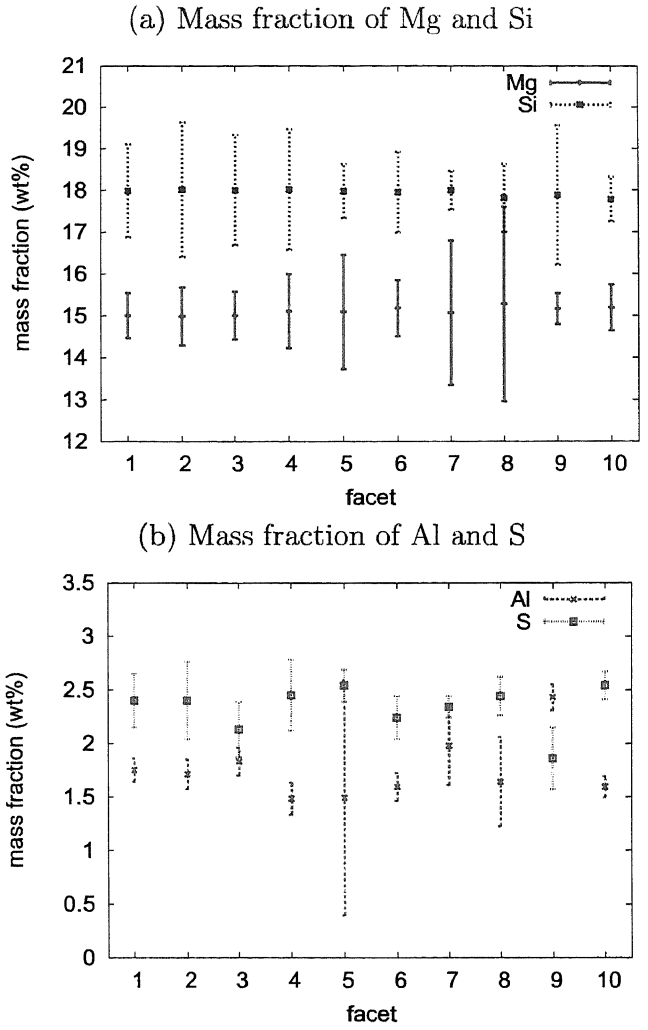

Figure 9.7: Best-fit mass fraction *vs.* facets relation. The abundance of Mg and Si appears to be regionally homogeneous but the best-fit mass fractions of Al and S vary at local areas.

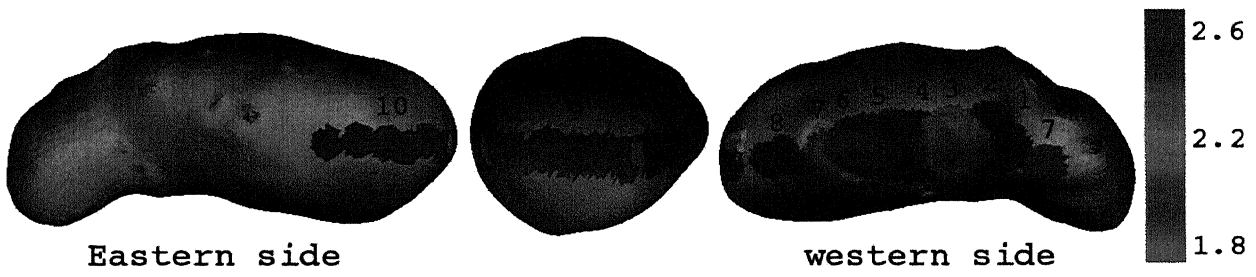

Figure 9.8: The best-fit mass fractions of sulfur, plotted on the shape model of Itokawa (Demura *et al.*, 2006). Numbers indicate observation areas called facet. Color map shows the mass fractions of sulfur abundance between 1.8 and 2.6 (wt.%). The abundances for duplicated observation areas are shown with average elemental composition. Although the distribution of Mg and Si abundance is homogeneous, the best-fit sulfur abundances vary at local areas. The lowest sulfur area #9 is close to large cratered area (*e.g.*, in Figure 3 of Demura *et al.*, 2006).

Chapter 10

Discussions

In previous chapters, results of our study indicated that the elemental composition of Itokawa resembles that of ordinary chondrites, and some features were found: (1) best-fit mass fraction of Fe is larger than that of average elemental composition of ordinary chondrites, (2) mass fractions of Mg and Si on the surface materials of Itokawa are globally homogeneous, (3) but mass fractions of Al and S vary varied at local areas.

In this chapter, the probable elemental composition of Itokawa and the reason for elemental variation of the surface are discussed, including compositional changes due to apparent effect and surface alteration. Also, the elemental relationship between Itokawa and meteorites is discussed, and the evolution and origin of Itokawa is speculated, such as (1) the reason for spectrally reddened and darkened feature, (2) compositional heterogeneity at local area, and (3) the parent body of Itokawa.

10.1 Influence of apparent effects

Our analysis has not considered apparent effects, *i.e.*, variation of the mass fractions due to a mineral mixing effect and a shadowing effect. The shadowing effect causes a decrease in the intensities of light scattering. This effect has been classically studied by Seelinger (1887) for light scattering. Recently, the shadowing effect for fluorescent X-rays has been studied by Okada and Kuwada (1997), and Maruyama *et al.* (2007). This effect will remarkably happen when the size of particles in the rough surface is as large as the transmission depth of fluorescent X-rays (<100 μm). The intensity of fluorescent X-rays varies in each characteristic energies, accompanied with phase angles (critical phase angle is over 60 degrees (Maruyama *et al.*, 2007)). The observation of XRS was carried out in low phase angles (<10°), and thus this effect did not remarkably affect results of this study. Therefore, this effect was neglected for analysis. However, the mineral mixing effect is not negligible as described bellow in details.

10.1.1 Correction with mineral mixing effects

The mineral mixing effect has not been considered in our analysis, either. It causes apparent changes for observed mass fraction. In particular, It is necessary to correct the matrix effects (Equation 4.2) for each mineral. The effect has been studied by Nittler *et al.* (2001) and Akagawa (2003). This effect depends on volume size of mineral and it apparently changes the observed elemental abundance. Here, the model of fluorescent X-rays in Equation 4.3 is rewritten as follows,

$$I^f(E_i^f) = \sum_k V_k \frac{\Omega S}{4\pi} \int \frac{\omega_i p_i j_i t_i w_i \tau_i(E) J(E)}{\sum_j \left(w_j \mu_j(E) + w_j \mu_j(E_i^f) \frac{\cos\phi_1}{\cos\phi_2} \right)} dE,$$

where V_k is the mineral volume of end member k.

The actual mineral volume on the surface of Itokawa is uncertain but the probable mass fractions with typical volume ratios of meteorites were estimated (Table 10.1). The correction factor of elemental ratios of a mineral mixing model for a homogeneous model, obtained from Nittler *et al.* (2001) and Akagawa (2003), are shown in Figure 10.1. These corrections are high Iron and low Iron correction. It is not complete correction and thus it includes uncertainty.

Table 10.2 shows the corrected results with mineral mixing effects. These imply that the results of analysis for S/Si ratios, assuming the homogeneous model, may result in an over-estimation by 30%, and also those for Fe may be 50% over estimation. Therefore, the actual abundance of sulfur on the surface of Itokawa may be smaller than the result obtained in this study and also that the actual abundance of Fe is larger than the result of our analysis. If so S may globally be depleted and the abundance of Fe is lower on the surface of Itokawa. Thus, the abundance of sulfur on the surface of Itokawa is almost equal to or even lower than that of average elemental composition of ordinary chondrites, and abundance of Fe may be the same as the average elemental composition of ordinary chondrites.

Table 10.1: X-ray fluorescence photon ratios for mineral mixing / homogeneous model.

Chondrite	Mg/Si	Al/Si	S/Si	Ca/Si	Fe/Si	Ref.
LL	0.95	1.32	0.78	0.93	0.78	Nittler *et al.*, (2001)
H	1.05	1.25	0.69	0.80	0.56	
LL	0.97	1.72	0.64	0.88	0.72	Akagawa (2003)
H	1.09	1.72	0.61	0.85	0.43	

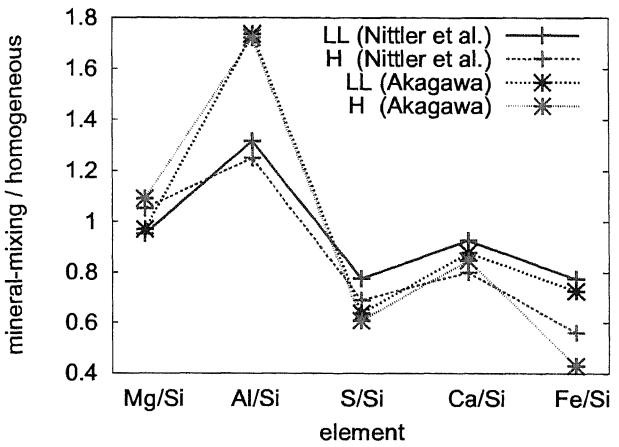

Figure 10.1: Elemental abundance ratios of the mineral mixing model for the homogeneous model, obtained from Nittler *et al.* (2001) and Akagawa (2003). The mass fractions of the mineral mixing model depend on volume ratios of minerals. Since the X-ray fluorescence model in Equation 4.3 does not contain mineral volumes, it is necessary to correct the mineral mixing effects. However, the actual volumes for minerals on the surface of Itokawa are uncertain. Therefore, the typical one was used here.

Table 10.2: Conversion with mineral mixing effect for the results.

-	Mg/Si	Al/Si	S/Si	Ca/Si	Fe/Si
No correction	0.85 ± 0.16	0.10 ± 0.10	0.14 ± 0.11	0.13 ± 0.13	1.40 ± 0.35
Low Iron correction	0.83 ± 0.15	0.17 ± 0.18	0.09 ± 0.07	0.12 ± 0.12	1.01 ± 0.26
High Iron correction	0.93 ± 0.17	0.17 ± 0.18	0.08 ± 0.07	0.11 ± 0.11	0.60 ± 0.15

10.2 Speculation of surface alteration

A possible surface alteration process on Itokawa is discussed below.

10.2.1 Influence of space weathering

Although some researchers have studied the space weathering on asteroids (*e.g.*, Pieters *et al.*, 2000; Hapke, 2001, Sasaki *et al.*, 2001), the derivation is an uncertain issue. Therefore, the surface alteration is discussed within the present knowledge.

In the observations of Itokawa, brightness and color variations on the surface have been found by using the AMICA (*e.g.*, Ishiguro *et al.*, 2006; Sasaki *et al.*, 2006) and the NIRS (Abe *et al.*, 2006). This surface heterogeneity might be caused by space weathering.

In X-ray fluorescence observation of S(IV) asteroid 433 Eros with X-ray spectrometer on-board NEAR-Shoemaker, Trombka *et al.* (2000) and Nittler *et al.* (2001) have reported that the ratio for S/Si on the surface is much lower than that of ordinary chondrites. Nittler *et al.* (2001) have suggested that the reason is impact-induced volatilization and/or photo- or ion-induced sputtering at the surface of the asteroid, or loss of FeS-rich material due to partial melting. Also, a sulfur volatilization process due to space weathering such as micro-meteorite impacts and/or energetic erosion due to solar wind sputtering has been proposed by Killen (2003), and Kracher and Sears (2005). Their timescale estimation for sulfur depletion in the uppermost layer of 10–100 μm due to space weathering is of the order of 10^6 years, so that sulfur on the surface can easily be evaporated from the uppermost layer.

The observation results also indicate low sulfur mass fraction and its regional variation. Here, the timescale of sulfur depletion on the uppermost surface of Itokawa is estimated. Since the escape velocity of Itokawa is very low (~0.2 m/sec), gas on the Itokawa is easy to escape away due to thermal diffusion as Jeans escape. Velocity distribution of ideal gas $f(v_x, v_y, v_z)$ can be expressed by Maxwell distribution as follows,

$$f(v_x, v_y, v_z) = \left(\frac{m}{2\pi k_B T}\right)^{3/2} \exp\left[-\frac{m(v_x^2 + v_y^2 + v_z^2)}{2k_B T}\right],$$

where m is mass of particle, k_B is Boltzmann constant, T is temperature of particle, and v is velocity of particle. Velocity distribution function $\tilde{f}(v)dv$, after the replacement $dv_x dv_y dv_z = 4\pi v^2 dv d\Omega$ (Ω:solid angle) is

$$\tilde{f}(v)dv = 4\pi \left(\frac{m}{2\pi k_B T}\right)^{3/2} v^2 \exp\left[-\frac{mv^2}{2k_B T}\right] dv, \tag{10.1}$$

where $v = \sqrt{v_x^2 + v_y^2 + v_z^2}$. The escape velocity of Itokawa is about 0.2 m/sec. For example, sulfur vapor gas acts on as shown in Figure 10.2, assuming the sulfur mass m_S is 32.06 g/mol, Avogadro's number N_A is 6.02× 10^{23} mol^{-1}, and Boltzmann constant k_B is 1.38× 10^{-23} J/K.

Kracher and Sears (2005) have indicated that the elements on asteroids vaporized by energetic erosion of solar wind sputtering. Here, the time-scale for mineral vaporization on the surface of asteroids was calculated by their method.

In this study, a finite volume model of a single mineral was assumed, eroded by solar wind sputtering as shown schematically in Figure 10.3. In order to vapor a block of mineral, the required dissociation energy (total enthalpy) is the sum of standard enthalpy of formation from the elements ΔH_f and enthalpy of conversion from element standard state to monatomic vapor $E_{\rm conv}$ as shown in Table 10.3. Here, the energetic erosion of finite minerals for LL chondrites as a function of time was calculated. The initial mass fraction was the average of mass fraction for LL chondrites (Table 8.3), and initial mineral volumes were the same as calculation of Akagawa (2003) as shown in Table 10.4. These typical mineral volume ratios were taken from the values of Onuma (1987). The flux of solar wind 2×10^8 ions/s/cm^2 at 1 AU was assumed, and energy conversion factor was assumed to be 0.001%.

Figure 10.4 shows erosion rate of volumes ratios of finite mineral blocks in time by solar wind sputtering. Also, Figure 10.5 shows energetic erosion in terms of mass fractions of LL chondrites. For the results of time scale estimation for energetic erosion of major elemental mass fractions, sulfur could evaporate on the uppermost surface layer with 10 million years. Therefore, the sulfur on the surface of asteroid may be easy to evaporate due to space weathering in a long time scale. However, the lifetime of near-Earth asteroids has been considered about 1 million years because asteroid will fall into the Sun in short time (*e.g.*, Yoshikawa and Michel, 2006). Also the lifetime of Itokawa may be probably short. Thus, sulfur evaporation by space weathering may not be significant.

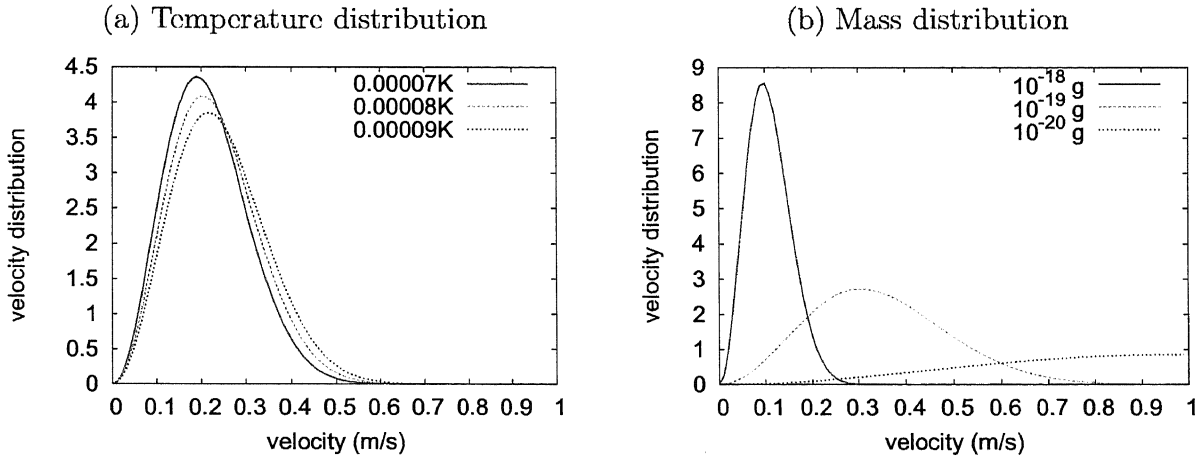

Figure 10.2: Distribution probability of Boltzmann velocity.

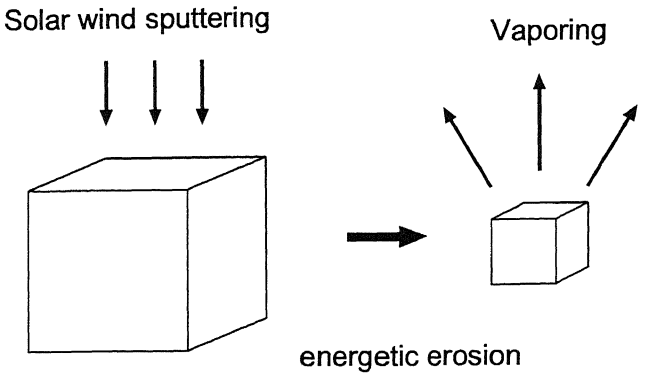

Figure 10.3: Energetic erosion by solar wind sputtering for finite blocks.

Table 10.3: Dissociation energy for vaporing of minerals.

Mineral	ΔHf kJ/mol	Econv kJ/mol	V_0 cm^3/mol	(ΔHf + Econv)/V_0 kJ/cm^3	Reference
Forsterite	2175.72	1740.92	43.79	89.44	Robie *et al.* (1979)
Fayalite	1478.17	2277.72	46.39	80.96	Robie *et al.* (1979)
Enstatite	1548.72	1344.64	31.28	92.50	Chernosky *et al.* (1985)
Ferrosilite	1193.45	1613.04	32.96	85.15	Sueno *et al.* (1976)
Wollastonite	1632.00	1375.34	39.83	75.50	Hemingway *et al.* (1982)
Orthoclase	3959.56	2082.44	108.28	55.80	Colville and Ribbe (1968)
Anorthite	4232.50	3731.24	100.79	79.01	Hemingway *et al.* (1982)
Albite	3929.86	3780.94	100.07	77.05	Robie *et al.* (1979)
Iron	-	415.50	7.09	58.59	Robie *et al.* (1979)
Troilite	101.000	692.67	18.17	43.69	King and Prewitt (1982)

Table 10.4: The example of initial volume ratios for minerals.

Mineral	Volume ratios (Vol%)
Forsterite	44.24
Fayalite	14.74
Enstatite	15.24
Ferrosilite	3.98
Wollastonite	2.85
Orthoclase	0.47
Anorthite	1.29
Albite	11.11
Iron	2.04
Troilite	4.05

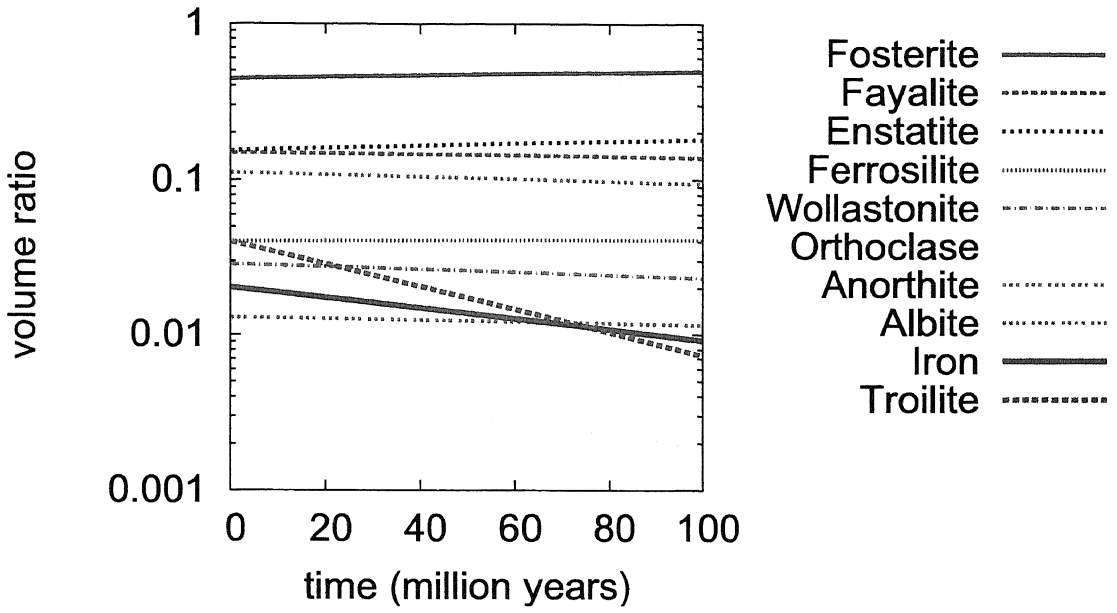

Figure 10.4: Erosion rate of volumes ratios of finite mineral blocks in time by solar wind sputtering. The volume ratios was assumed to be that of LL chondrites-analogues (Onuma, 1987).

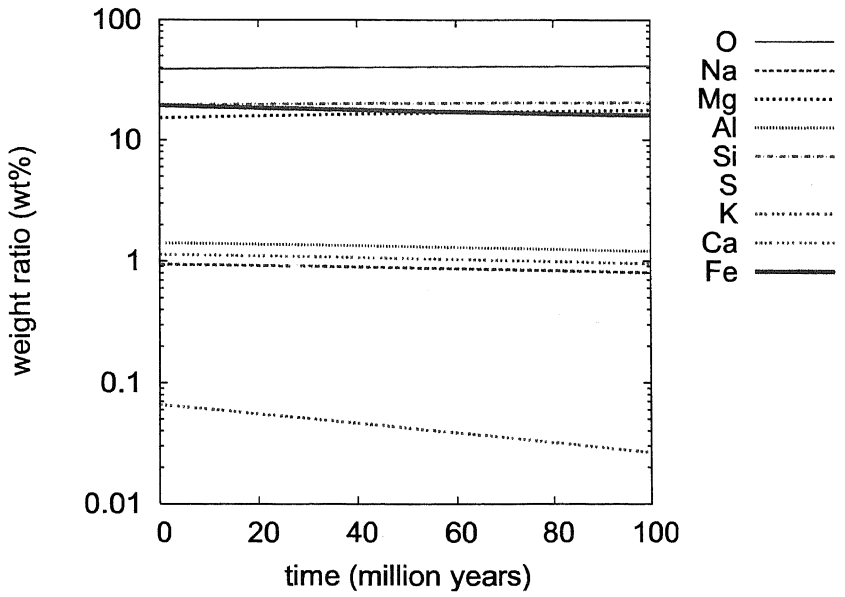

Figure 10.5: Elemental ratio caused by energetic erosion. Major elements, Na, Al, S, K, Ca, and Fe, may relatively cause to decrease by space weathering.

Impacts of micrometeorites

In general, a peak pressure of impact is larger for porous objects like Itokawa because thermal conduction is not effective in there. Impact heating of micrometeorites has been studied by Killen (2003). Her timescale estimation for sulfur depletion in the uppermost layer of 10–100 μm due to space weathering is of the order of 10^6 years, so that sulfur on the surface can easily be evaporated from the uppermost layer.

Resurfacing

Michel and Yoshikawa (2005) have shown that the probability for the collision of with the Earth is high within 10^6 years, so that planet encounter with Itokawa might occur. Sasaki *et al.* (2006) have suggested that the resurfacing process on Itokawa may be caused by seismic destruction due to impacts or tidal stress due to planet encounters, and thus the portion of exposed material on the surface may be little altered by space weathering. The geometric albedo of Itokawa ~30% (*e.g.*, Lederer *et al.*, 2005) is brighter than that of 433 Eros ~25% (*e.g.*, Li *et al.*, 2004), and also color variation on the surface of Itokawa was found with the AMICA (*e.g.*, Ishiguro, 2006).

Since our result did not indicate global depletion of sulfur, sulfur may be fresh at local areas due to the resurfacing process compared to highly altered materials by space weathering. Thus, the sulfur variation founds in this study may reflect the heterogeneity of the surface, altered by space weathering.

Impacts

The lowest sulfur abundance area is facet #9, close to large cratered area. This area may have experienced a heating process due to impacts, and thus the sulfur was vaporized. Also, aluminum enrichment is found at facet #9. One possible cause for it is a meteoritic impact of Al-enriched material. Although a high-speed impact explodes and ejects the surface objects, a low-speed impact leaves a portion of surface objects on the surface. The candidates for aluminum-rich and chondritic materials are carbonaceous chondrites. The black boulder on the surface of Itokawa at longitude of 0° (see below of Figure 1.6) may be a remnant of low-speed impactor such as C-class asteroids. Thus the aluminum enrichment and sulfur depletion deduced from our analysis may support the idea that aluminum-rich impact occurred on the surface of Itokawa.

10.2.2 Influence of partial melting

Since Itokawa is small (535×294×209 m^3), and is probably composed of rubble-piles (Fujiwara *et al.*, 2006), partial melting would not be effective after formation of Itokawa. However, fractionation of minerals might have occurred on the parent body of Itokawa.

A correlation coefficient (*e.g.*, Bevington and Robinson, 2003) for 10 ratios for Mg/Si *vs.* Al/Si, Al/Si *vs.* S/Si, and S/Si *vs.* Mg/Si are 0.03, -0.92, and 0.09, respectively. The negative correlation of Al/Si and S/Si imply that depletion of sulfur is correlated to enrichment of aluminum, and vice versa, and it appears to be a partial melting feature. Partial melting may induce the sulfur evaporation whose temperature is 1261 K on the parent body of Itokawa. It may also induce enrichment in aluminum because aluminum appears in first melt of chondritic material at sulfur evaporation temperature. The best-fit mass fractions Al and S vary at local areas.

Portions of partial melting features have been found on Itokawa in about 2 micron absorption band of the NIRS and in the Earth-based observations (Abell *et al.*, 2006). This result has

indicated that a portion of Itokawa is more enriched in Olivine than that of primitive ordinary chondrites. Thus, results of this study on the rich aluminum and lower sulfur features may also support the idea that partial melting events occurred on the parent body of Itokawa.

10.2.3 Influence of minor elements

The mass fraction of Minor elements were assumed to be that of average of ordinary chondrites, and then the total amount of minor elements was less than 4 wt% (see Table 8.3 and Appendix B). They did not cause large unsertainty for the observation results of XRS.

The mass fractions of O were not estimated because X-ray intensities of O K-α line (0.52 keV) were less than the detection limits of XRS. Thus, the mass fractions were assumed to be the ratios of metallic Fe and FeO $\sim$ 1:1 for L groups, given by the Urey–Craig relation. This assumption causes large errors but Si normalized values should reduce the errors.

Since the observation results of XRS are represented by mass fraction, they did not represent the net abundance of Itokawa. If the elemental composition of Itokawa is totally homogeneous, the observation results of XRS represent the bulk abundance of Itokawa. The elemental composition of Itokawa may be basically homogeneous because Itokawa is probably a rubble-pile structure that is rather primordial and not evolved inside, and thus the observation results of XRS may be equal to bulk abundance of Itokawa.

10.3 Relationship between Itokawa and meteorites

The observation results of XRS indicate that the surface materials on Itokawa are like chondritic composition. Here, the relationship between Itokawa and meteorite-analogues is determined in terms of major elemental composition. Since the observation results of XRS are represented by the elemental mass fraction, net abundance on the surface of Itokawa is uncertain. Thus, the relationship between asteroids and meteorites should be determined by Si normalized values such as Mg/Si, Al/Si, S/Si, Ca/Si, and Fe/Si.

Figures 10.6 – 10.18 show the results of global and local observation for elemental mass ratios, Mg/Si *vs.* Al/Si, Mg/Si *vs.* S/Si, Mg/Si *vs.* Ca/Si, Mg/Si *vs.* Fe/Si, Al/Si *vs.* S/Si, Al/Si *vs.* Ca/Si, Al/Si *vs.* Fe/Si, S/Si *vs.* Ca/Si, S/Si *vs.* Fe/Si, and Ca/Si *vs.* Fe/Si, together with those of major meteorites (Jarosewich, 2006; Yanai and Kojima, 1995; Mittlefehldt, 1998). These meteorites include candidates for the S-class asteroids such as ordinary chondrites including H, L, and LL chondrites, primitive achondrites including Acapulcoites, Winonaites, and Brachinites, iron meteorites including IAB (Gaffey *et al.*, 1993).

Here, the numbers of cases with consistent elemental mass ratios between meteorites and Itokawa are defined by the following rule: Group A: the elemental mass ratios of meteorite-analogues are consistent within 1σ error of the observed results of XRS. Group B: the elemental mass ratios of meteorite-analogues are consistent in 1σ to 3σ errors of the observed results of XRS. Group C the elemental mass ratios of meteorite-analogues are consistent over 3σ error of the observed results of XRS. Both of the corrected and non-corrected mass ratios with mineral mixing effect as shown in Table 10.5 – 10.13. Also, Tables 10.14 – 10.16 show the groups that have the largest number of consistency counts for elemental mass ratios of meteorites and Itokawa.

Angrites are basaltic meteorites with substantial amounts of calcium, making them clearly different from Itokawa. Pallasites and Mesosiderites are the mixtures of rock and metallic iron, and their composition is far from that of Itokawa. Ureilites are complicated carbon-bearing rocks that appear to be the residues from partial melting of an asteroid. Their compositions, especially their high Mg/Si, rule them out as candidates for Itokawa. Those meteorites can be

ruled out on compositional grounds. This result means that Itokawa did not undergo a global melting event. Differentiated meteorites, formed by melting on their parent body, are far from the composition of Itokawa. The HED meteorites (Howardites, Eucrites, and Diogenites) are basalt lava flows (Eucrites), coarse-grained igneous rocks (Diogenites), or mixtures of two (Howardites).

The comparison of the elemental classification between the major mass ratios of Itokawa and those of meteorite-analogues, such as Mg/Si, Al/Si, S/Si, Ca/Si and Fe/Si, indicates that Winonaites and IAB irons as metallic Fe-rich meteorites are ruled out as the candidates for meteorite-analogues of Itokawa, which is an S(IV) subtype asteroids classified, by Gaffey *et al.* (1993). This implies that Itokawa does not appear to be a metallic Fe-rich asteroid. Also most probable candidates for Itokawa are ordinary L or LL chondrites, EL chondrites, or Brachinites, Acapulcoites or Winonaites as primitive achondrites, in terms of the elemental mass ratios of Mg/Si *vs.* Fe/Si.

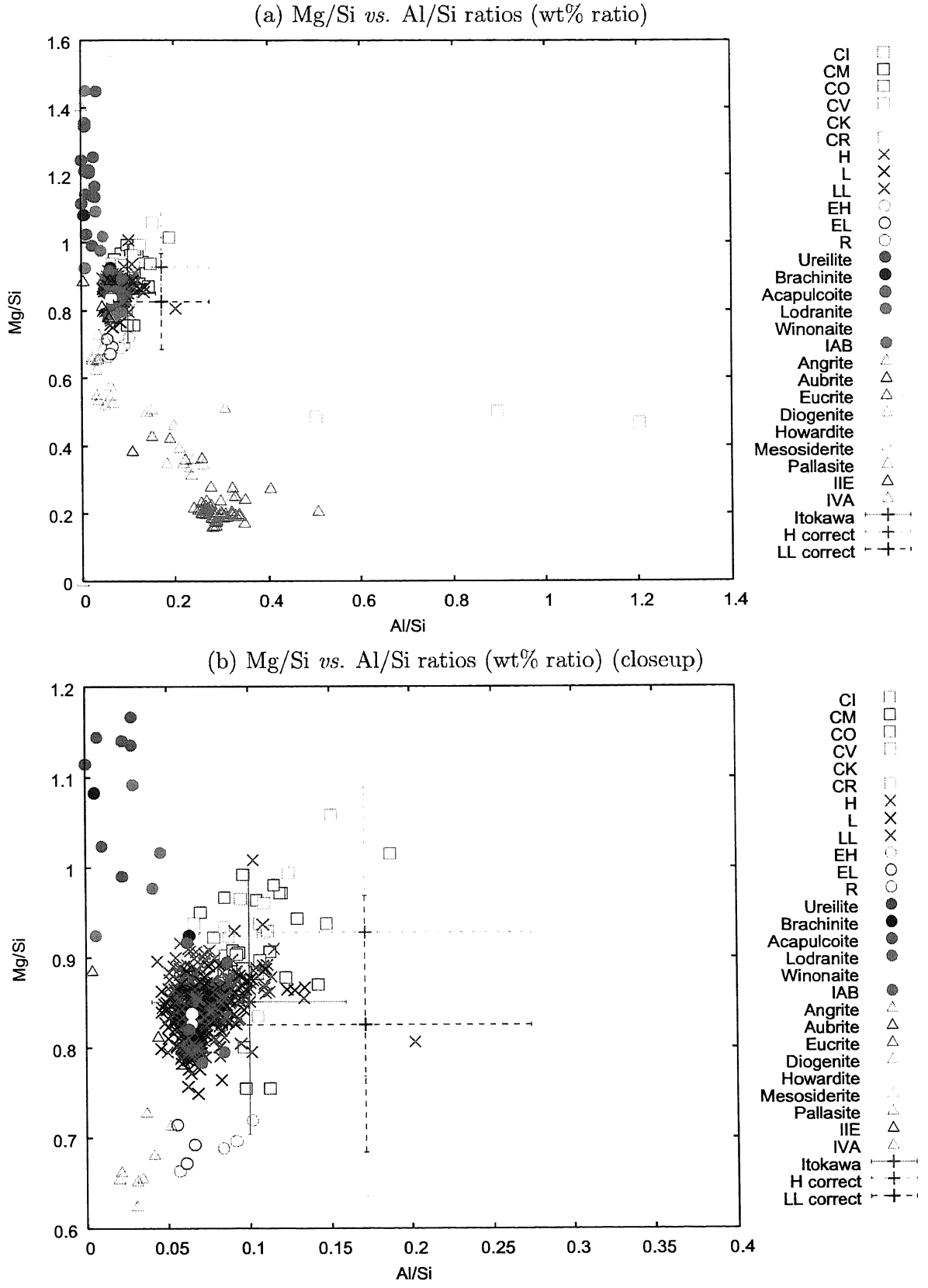

Figure 10.6: **The elemental mass ratios of Itokawa and meteorites for Mg/Si *vs.* Al/Si. Red crossed indicates no mineral mixing correction, green crossed point indicates mineral mixing correction with high Iron, and blue crossed point indicates mineral mixing correction with low Iron (Global).**

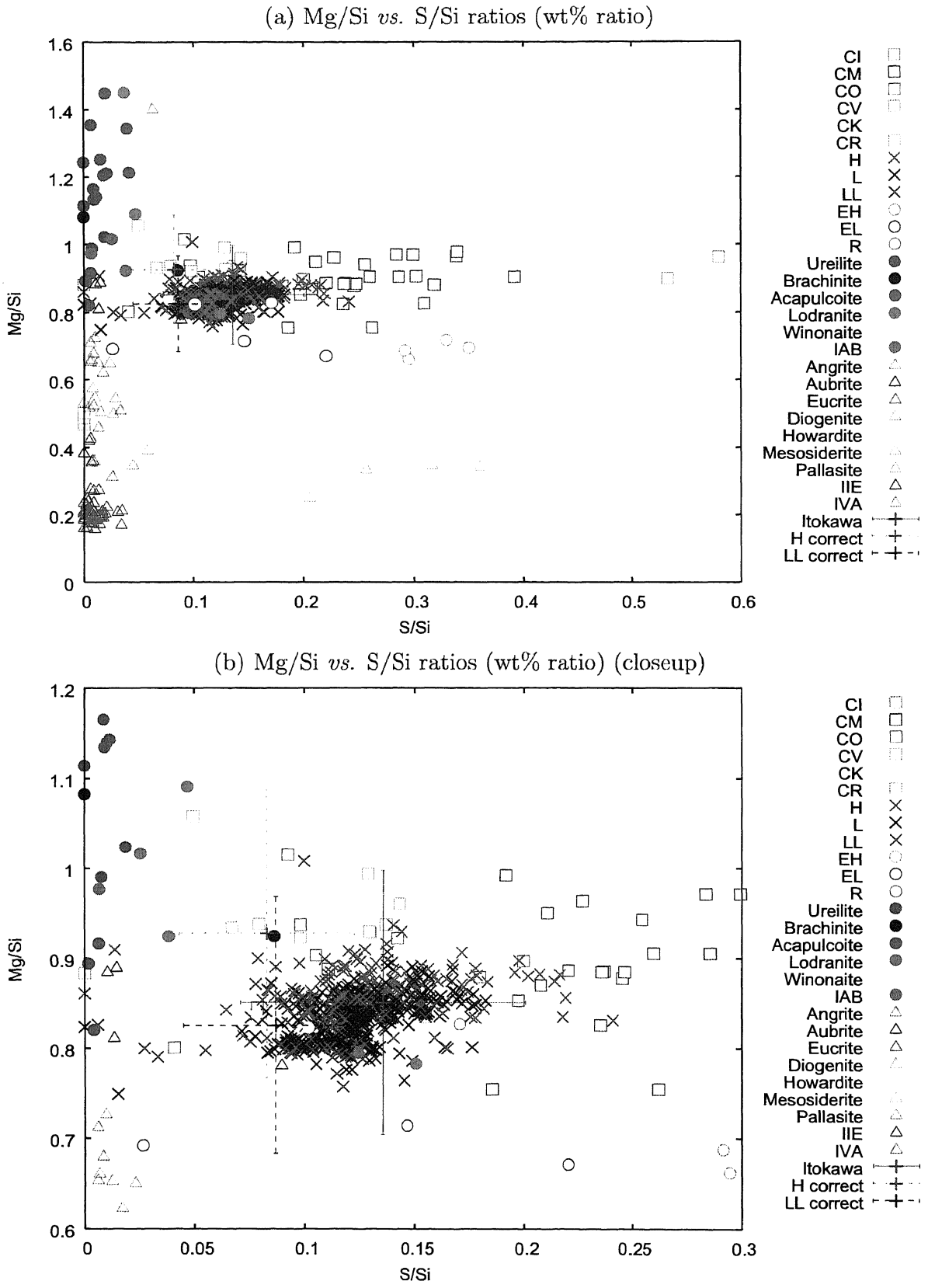

Figure 10.7: The elemental mass ratios of Itokawa and meteorites for Mg/Si *vs.* S/Si. Red crossed indicates no mineral mixing correction, green crossed point indicates mineral mixing correction with high Iron, and blue crossed point indicates mineral mixing correction with low Iron (Global).

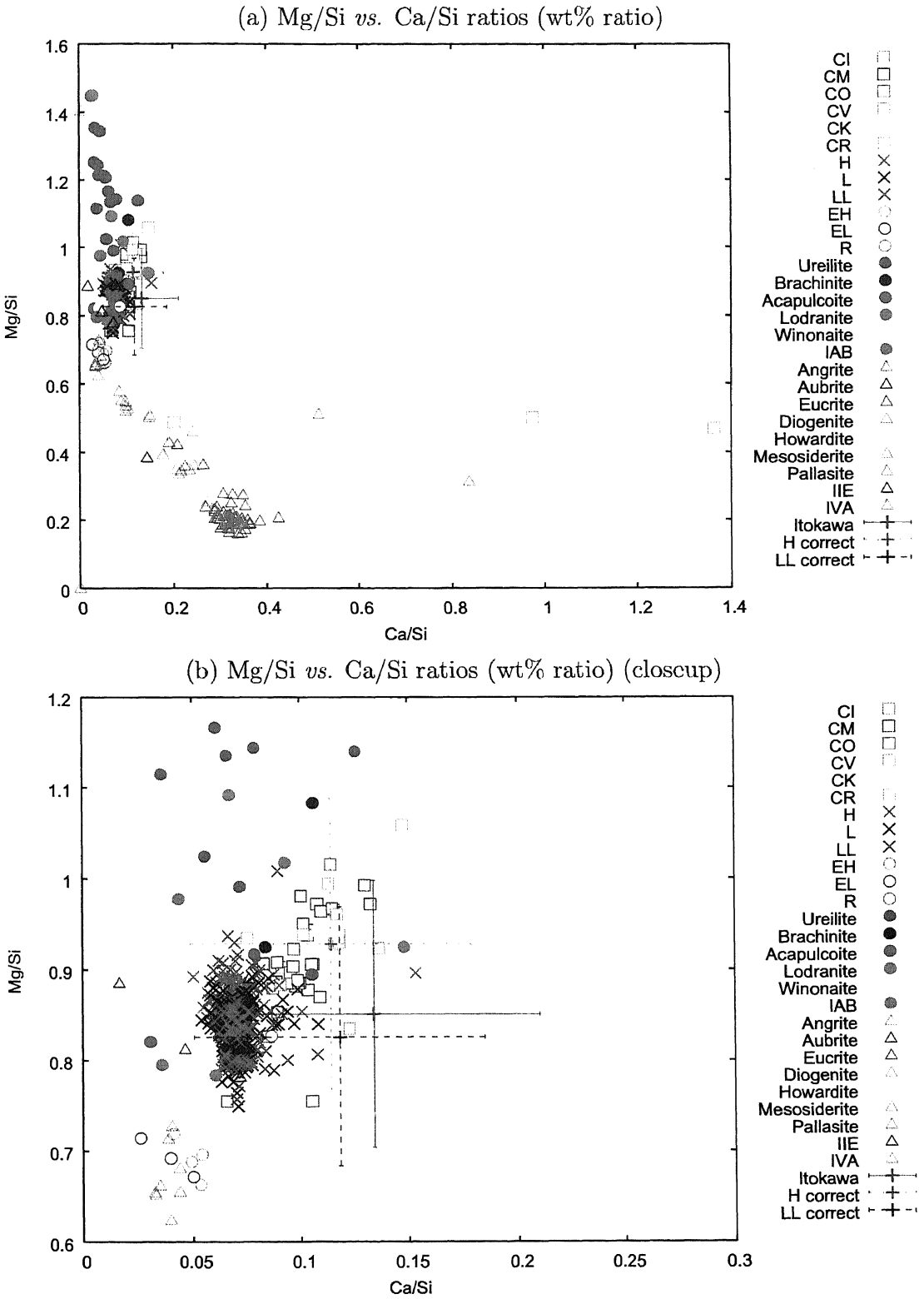

Figure 10.8: The elemental mass ratios of Itokawa and meteorites for Mg/Si *vs.* Ca/Si. Red crossed indicates no mineral mixing correction, green crossed point indicates mineral mixing correction with high Iron, and blue crossed point indicates mineral mixing correction with low Iron (Global).

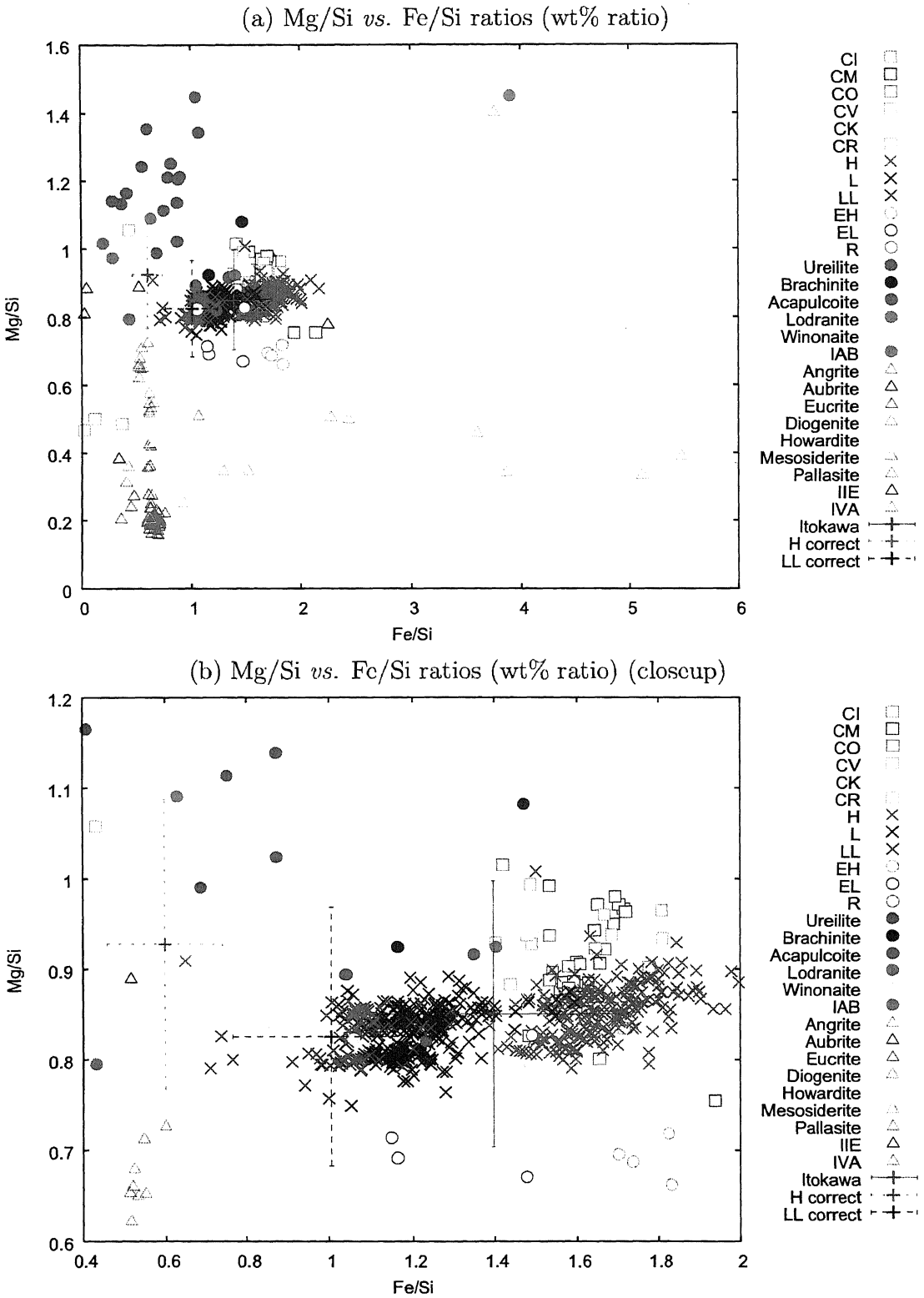

Figure 10.9: The elemental mass ratios of Itokawa and meteorites for Mg/Si *vs.* Fe/Si. Red crossed indicates no mineral mixing correction, green crossed point indicates mineral mixing correction with high Iron, and blue crossed point indicates mineral mixing correction with low Iron (Global).

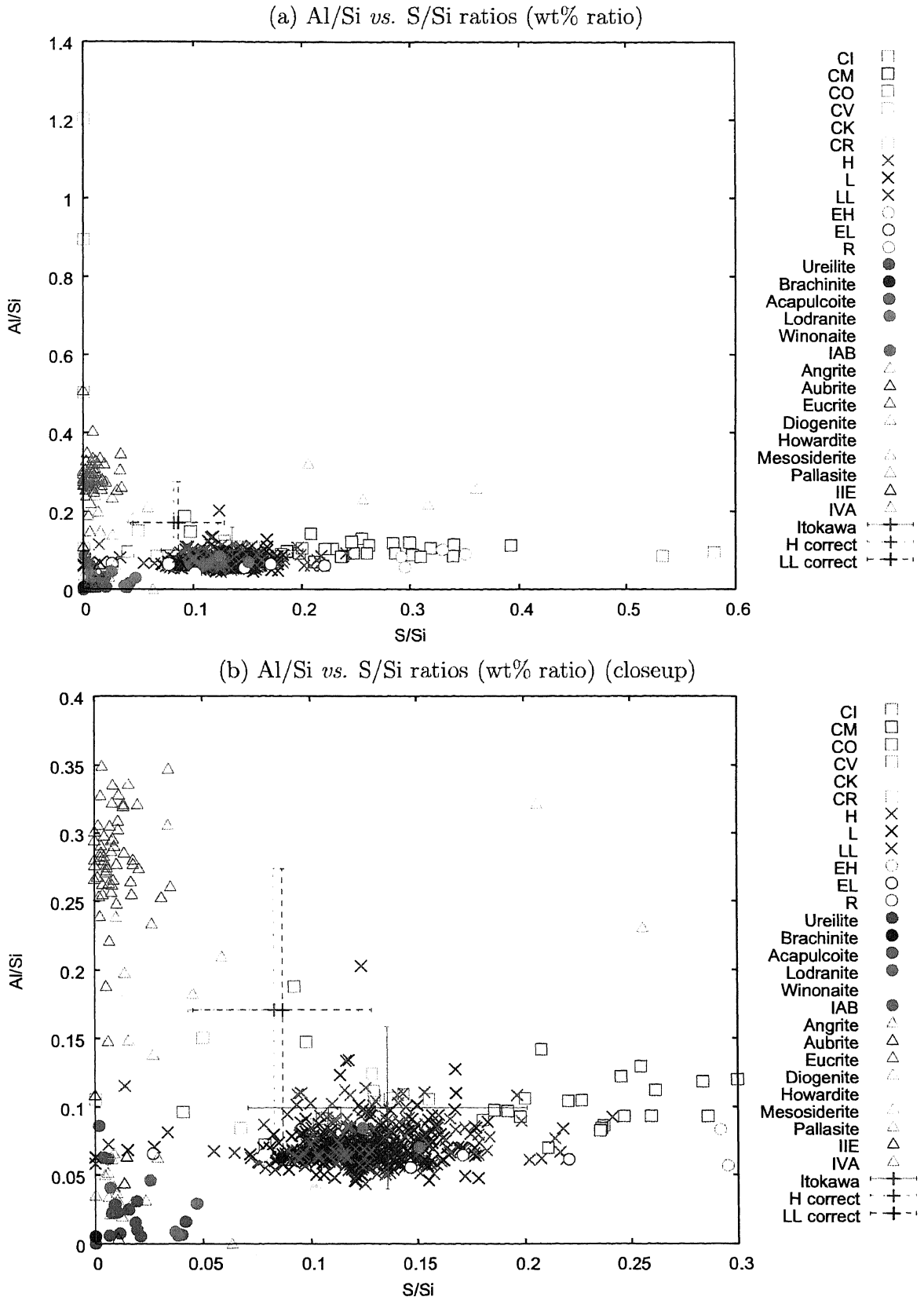

Figure 10.10: **The elemental mass ratios of Itokawa and meteorites for Al/Si *vs.* S/Si. Red crossed indicates no mineral mixing correction, green crossed point indicates mineral mixing correction with high Iron, and blue crossed point indicates mineral mixing correction with low Iron (Global).**

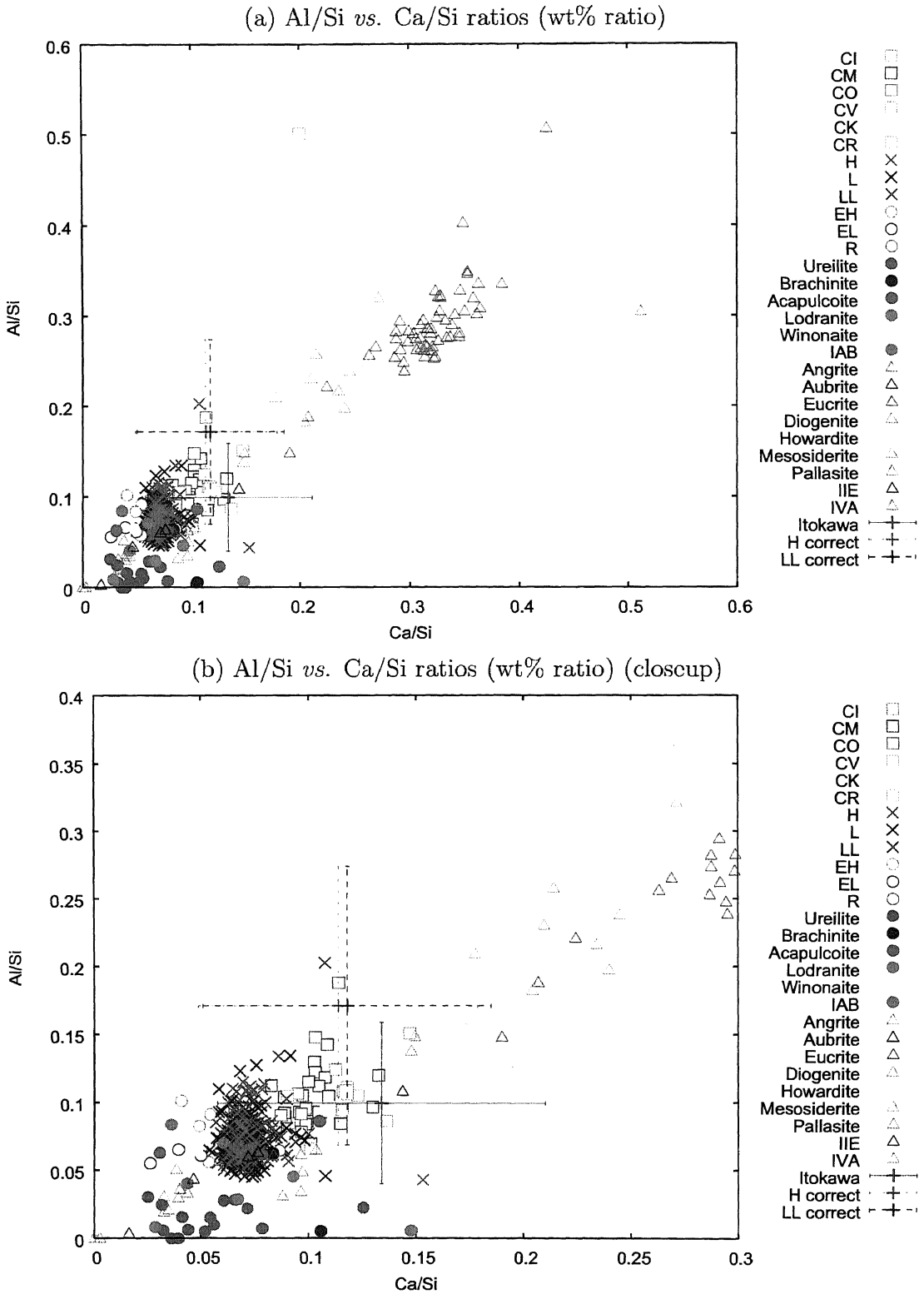

Figure 10.11: The elemental mass ratios of Itokawa and meteorites for Al/Si *vs.* Ca/Si. Red crossed indicates no mineral mixing correction, green crossed point indicates mineral mixing correction with high Iron, and blue crossed point indicates mineral mixing correction with low Iron (Global).

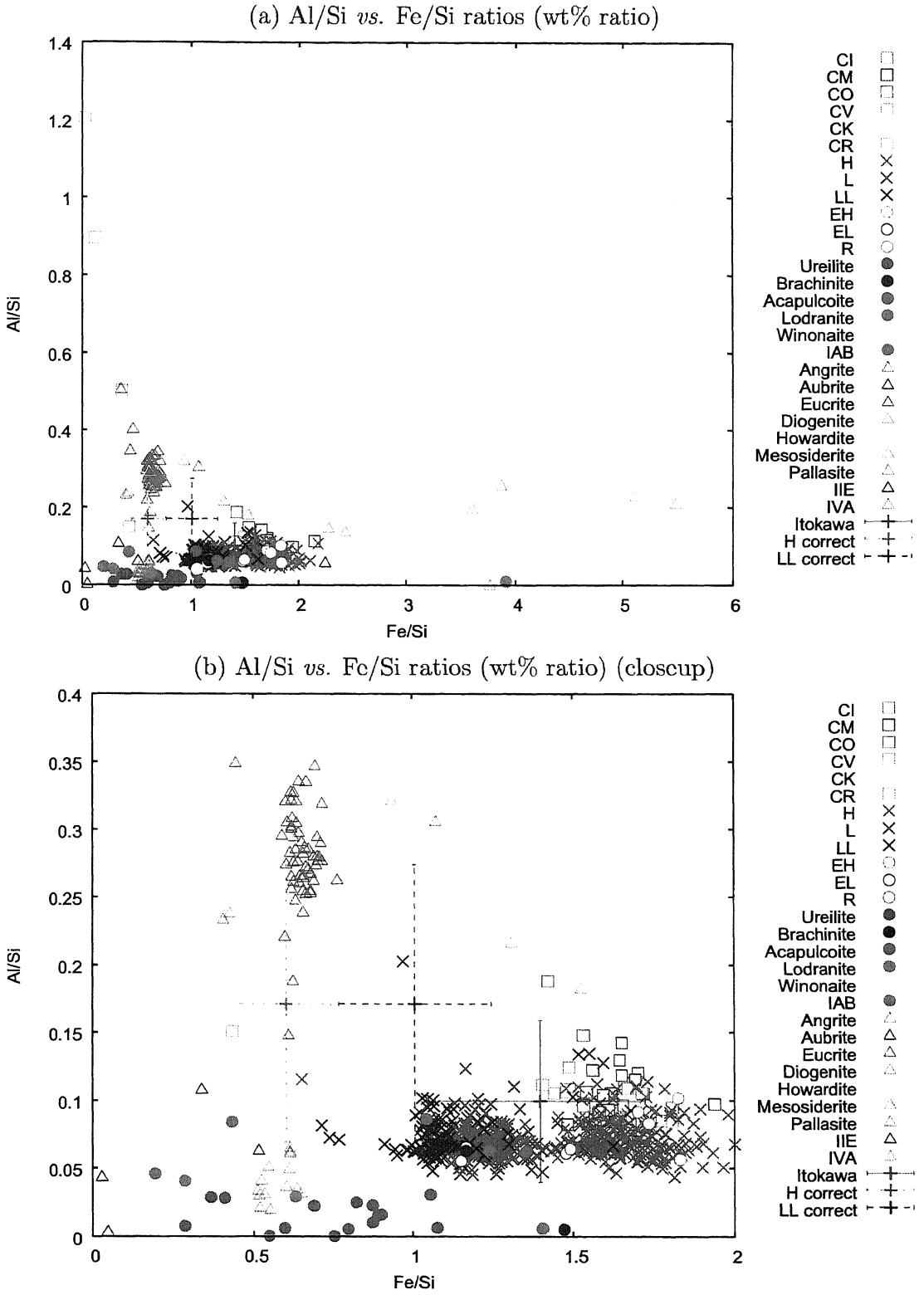

Figure 10.12: **The elemental mass ratios of Itokawa and meteorites for Al/Si *vs.* Fe/Si. Red crossed indicates no mineral mixing correction, green crossed point indicates mineral mixing correction with high Iron, and blue crossed point indicates mineral mixing correction with low Iron (Global).**

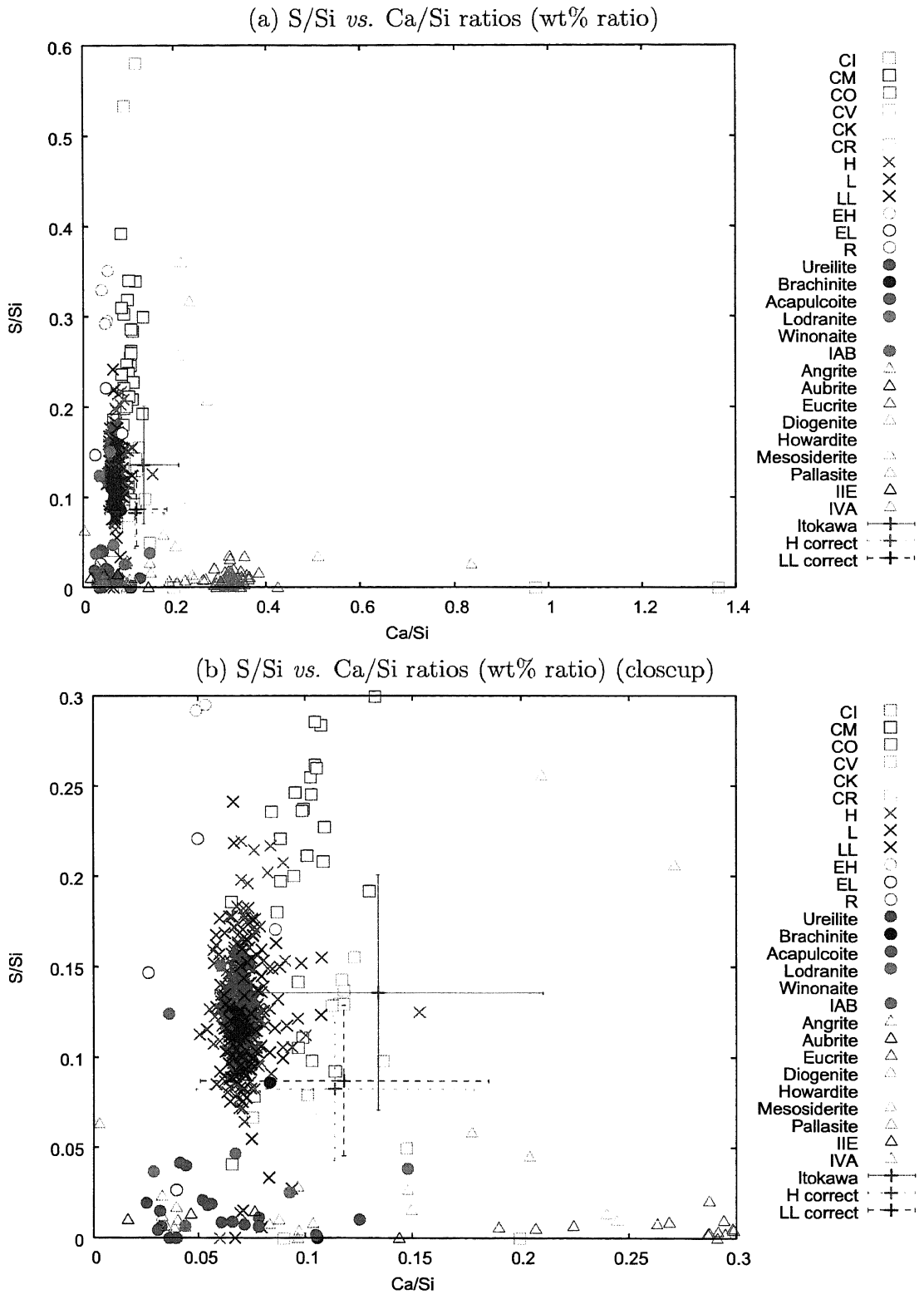

Figure 10.13: The elemental mass ratios of Itokawa and meteorites S/Si *vs.* Ca/Si. Red crossed indicates no mineral mixing correction, green crossed point indicates mineral mixing correction with high Iron, and blue crossed point indicates mineral mixing correction with low Iron (Global).

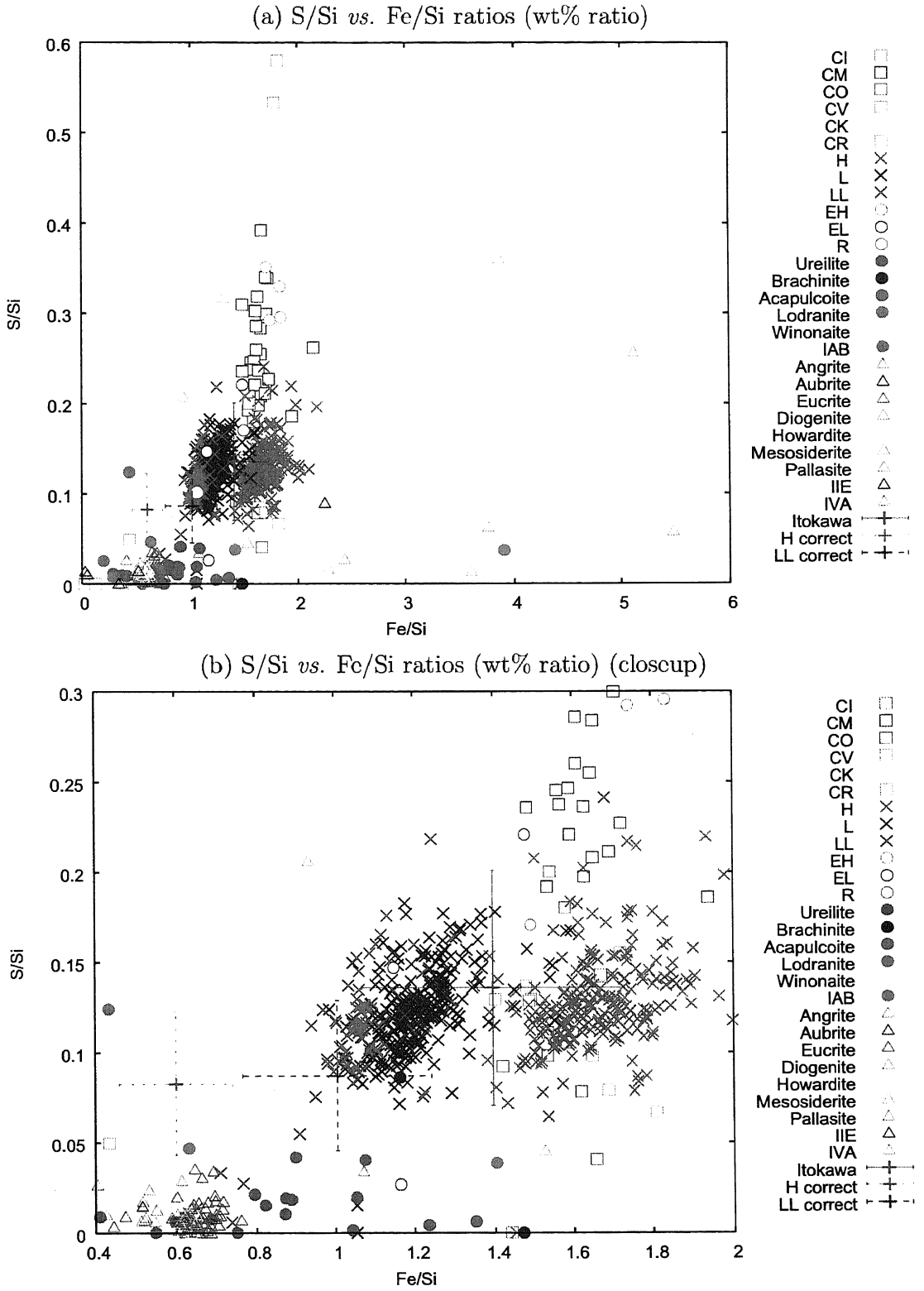

Figure 10.14: **The elemental mass ratios of Itokawa and meteorites for S/Si *vs.* Fe/Si. Red crossed indicates no mineral mixing correction, green crossed point indicates mineral mixing correction with high Iron, and blue crossed point indicates mineral mixing correction with low Iron (Global).**

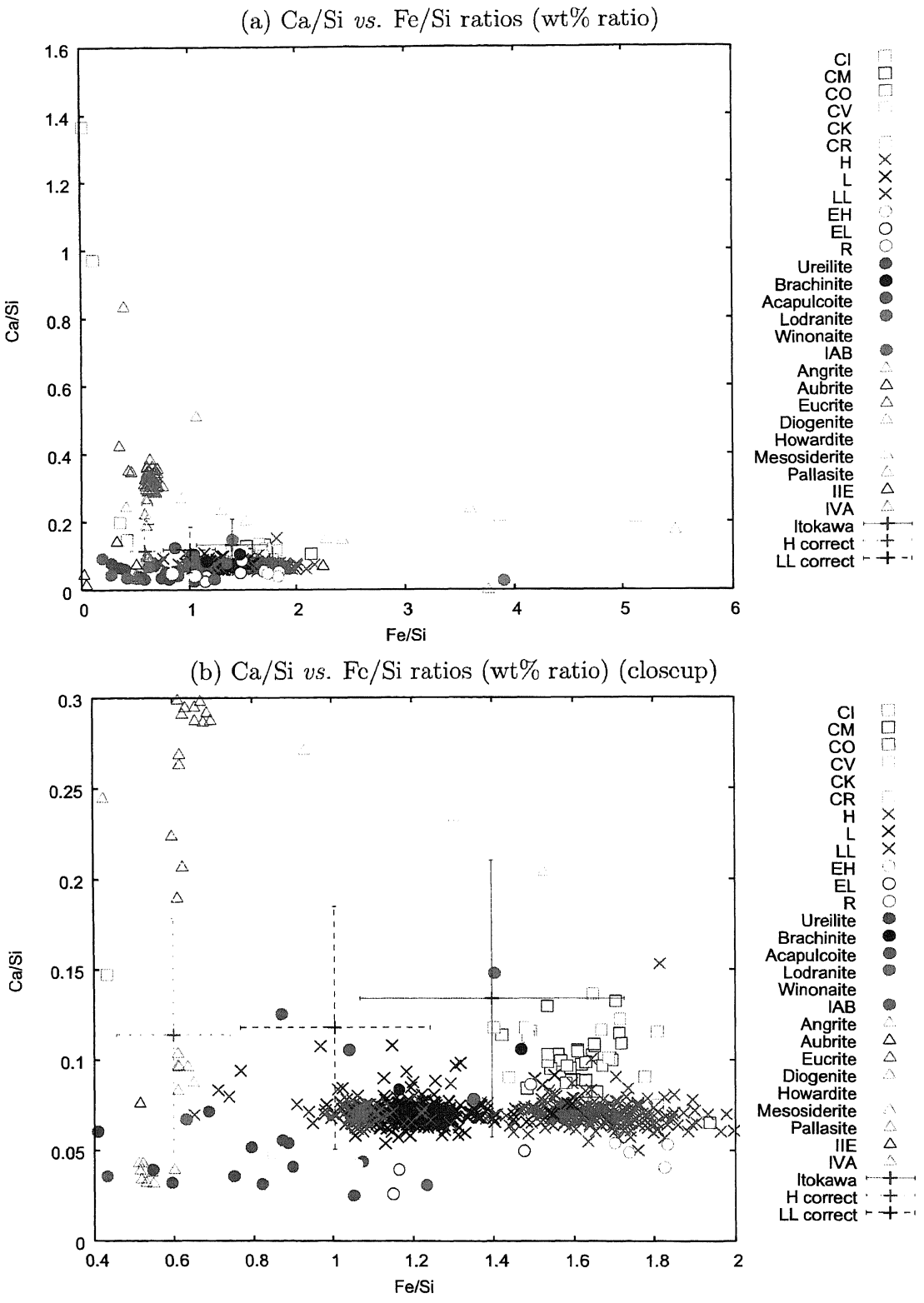

Figure 10.15: **The elemental mass ratios of Itokawa and meteorites for Ca/Si *vs.* Fe/Si. Red crossed indicates no mineral mixing correction, green crossed point indicates mineral mixing correction with high Iron, and blue crossed point indicates mineral mixing correction with low Iron (Global).**

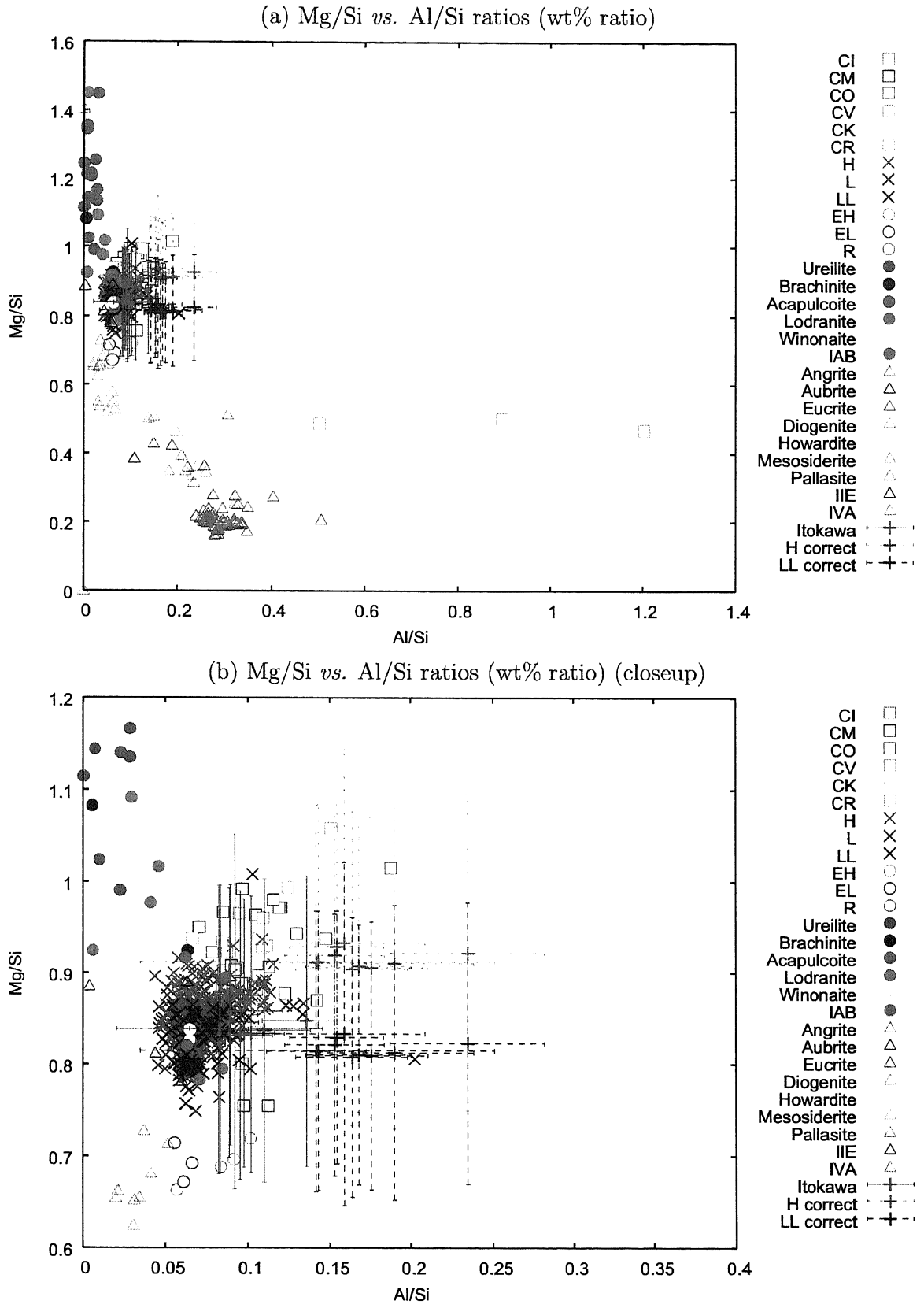

Figure 10.16: **The elemental mass ratios of Itokawa and meteorites for Mg/Si *vs.* Al/Si. Red crossed points indicate no mineral mixing correction, green crossed points indicate mineral mixing correction for H chondrites, and blue crossed points indicate mineral mixing correction for LL chondrites (Local).**

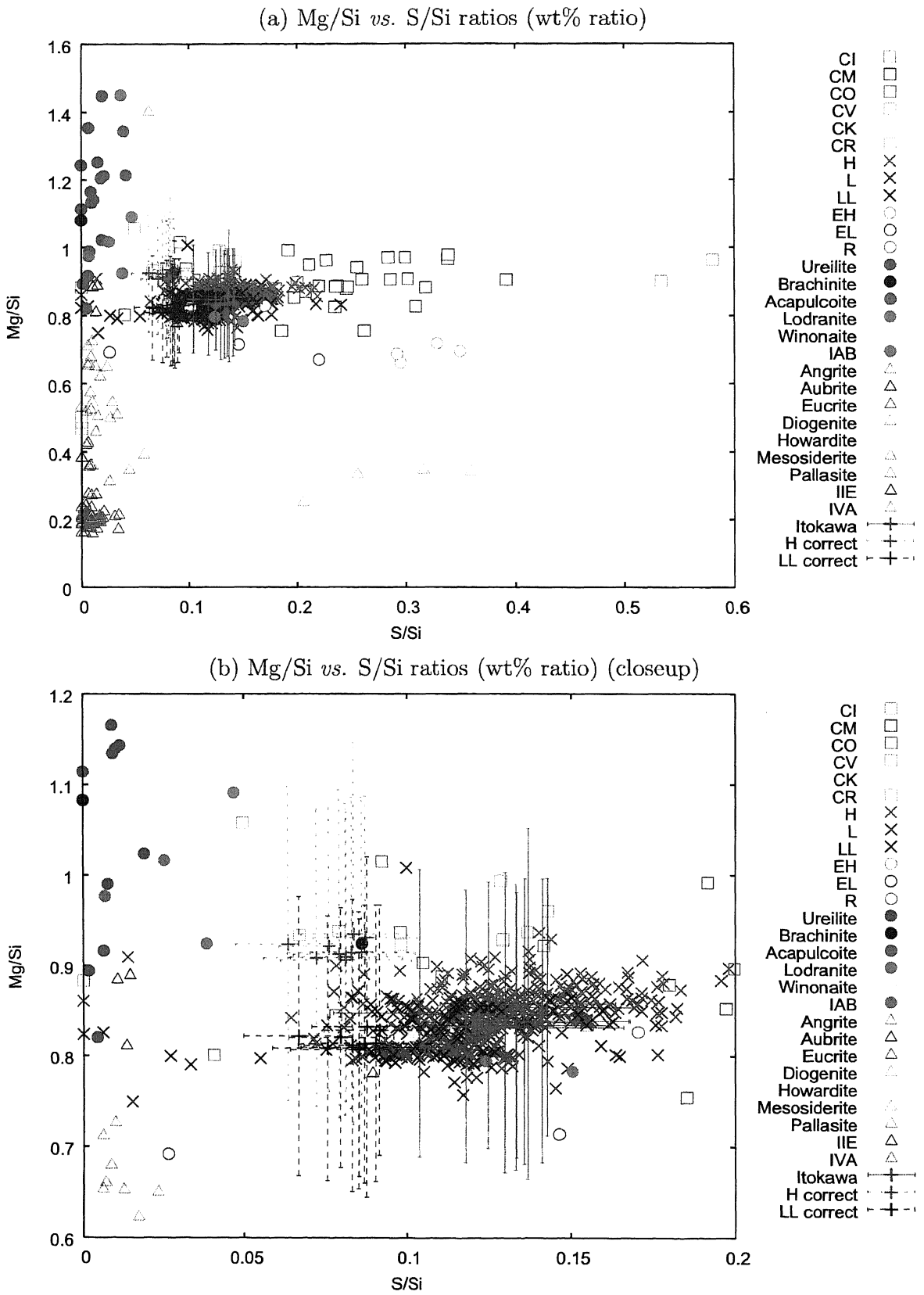

Figure 10.17: The elemental mass ratios of Itokawa and meteorites for Mg/Si *vs.* S/Si. Red crossed points indicate no mineral mixing correction, green crossed points indicate mineral mixing correction for H chondrites, and blue crossed points indicate mineral mixing correction for LL chondrites (Local).

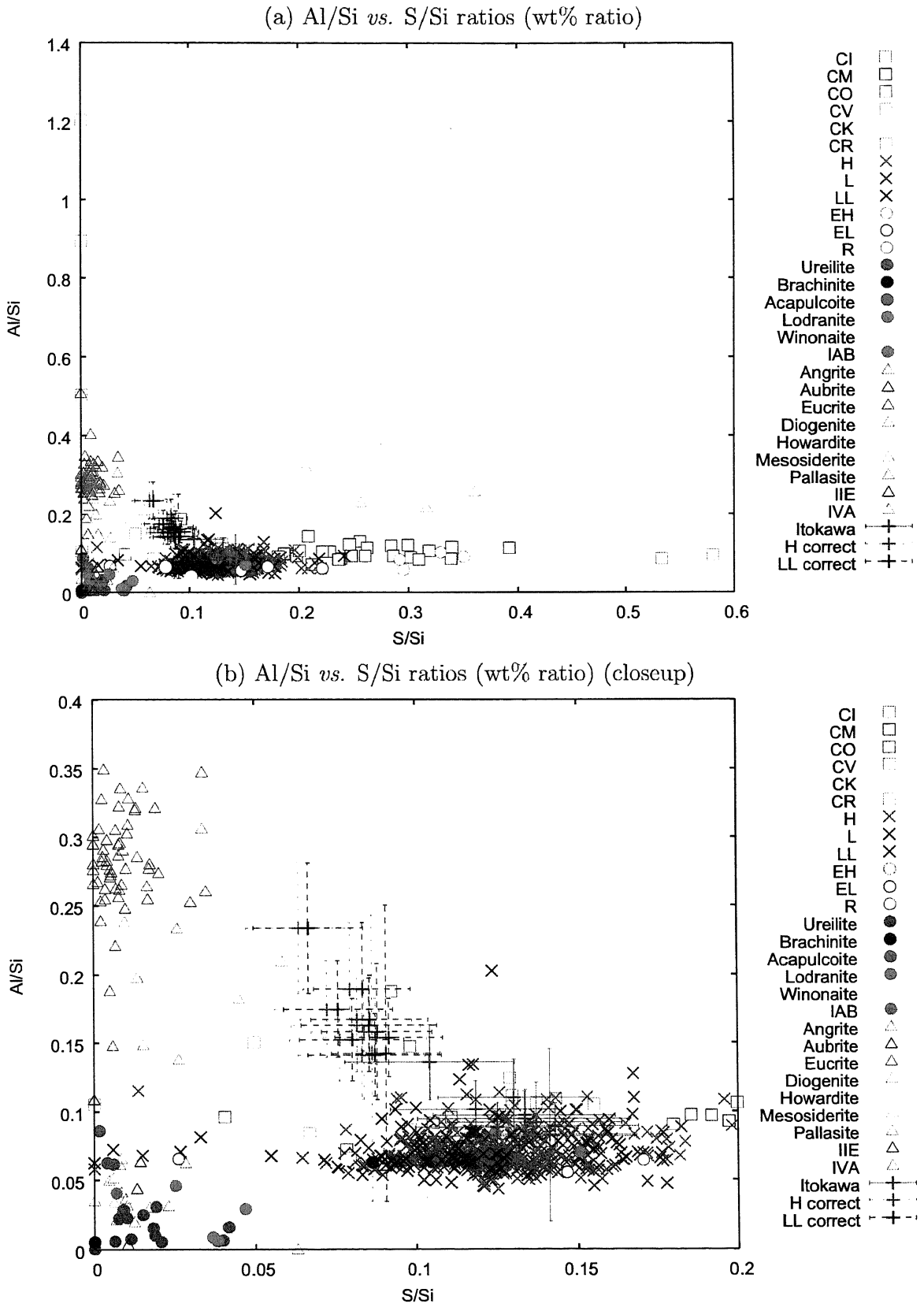

Figure 10.18: **The elemental mass ratios of Itokawa and meteorites. Red crossed points indicate no mineral mixing correction, green crossed points indicate mineral mixing correction for H chondrites, and blue crossed points indicate mineral mixing correction for LL chondrites (Local).**

Table 10.5: The number of group A (No correction).

	Mg/Si *vs.* Al/Si	Mg/Si *vs.* S/Si	Mg/Si *vs.* Ca/Si	Mg/Si *vs.* Fe/Si	Al/Si *vs.* S/Si	Al/Si *vs.* Ca/Si	Al/Si *vs.* Fe/Si	S/Si *vs.* Ca/Si	S/Si *vs.* Fe/Si	Ca/Si *vs.* Fe/Si	Number of Samples
CI	2	0	0	0	0	0	0	0	0	0	2
CM	24	3	1	22	3	1	22	1	2	0	24
CO	8	7	2	8	7	2	8	1	8	2	9
CV	8	7	0	8	7	0	8	0	7	0	12
CK	3	1	0	3	1	0	3	0	1	0	3
CR	2	1	1	1	1	1	1	0	1	0	2
H	229	221	199	160	221	199	160	195	156	138	229
L	256	254	227	245	254	227	245	225	245	217	256
LL	81	76	69	40	76	69	41	66	39	37	83
EH	1	0	1	0	0	4	1	0	0	1	4
EL	1	1	1	1	1	3	3	1	1	3	3
R	1	1	0	1	1	0	1	0	1	0	1
Ureilites	0	0	1	0	0	0	0	0	0	1	14
Brachinites	1	1	0	1	1	0	1	0	1	0	2
Acapulcoites	3	0	1	2	0	1	2	0	0	1	3
Lodranites	0	0	0	1	0	0	0	0	0	0	3
Winonaites	2	2	2	0	2	2	0	2	0	0	2
IAB	3	2	3	0	2	3	0	2	0	0	4
Angrites	0	0	0	0	0	0	0	0	0	0	2
Aubrites	1	0	2	0	0	1	0	0	0	0	2
Eucrite	0	0	0	0	0	0	0	0	0	0	57
Diogenites	1	0	2	0	0	2	0	0	0	0	13
Howardites	0	0	0	0	0	0	0	0	0	0	13
Mesosiderites	0	0	0	0	0	0	0	0	0	0	10
Pallasites	0	0	0	0	0	0	0	0	0	0	1
IIE	2	1	1	0	1	1	0	1	0	0	3
IVA	0	0	0	0	0	0	0	0	0	0	1

Table 10.6: The number of group B (No correction).

	Mg/Si *vs.* Al/Si	Mg/Si *vs.* S/Si	Mg/Si *vs.* Ca/Si	Mg/Si *vs.* Fe/Si	Al/Si *vs.* S/Si	Al/Si *vs.* Ca/Si	Al/Si *vs.* Fe/Si	S/Si *vs.* Ca/Si	S/Si *vs.* Fe/Si	Ca/Si *vs.* Fe/Si	Number of Samples
CI	2	0	2	2	0	2	2	0	0	2	2
CM	24	21	24	24	21	24	24	21	21	24	24
CO	9	9	9	9	9	9	9	9	9	9	9
CV	9	12	10	9	9	9	9	10	9	9	12
CK	3	3	3	3	3	3	3	3	3	3	3
CR	2	2	2	2	2	2	2	2	2	2	2
H	229	229	229	229	229	229	229	229	229	229	229
L	256	256	256	256	256	256	256	256	256	256	256
LL	83	83	83	83	83	83	83	83	83	83	83
EH	4	3	4	4	3	4	4	3	3	4	4
EL	3	3	3	3	3	3	3	3	3	3	3
R	1	1	1	1	1	1	1	1	1	1	1
Ureilites	12	12	12	10	15	15	13	15	13	13	14
Brachinites	2	2	2	2	2	2	2	2	2	2	1
Acapulcoites	3	3	3	3	3	3	3	3	3	3	2
Lodranites	2	2	2	2	3	3	2	3	2	2	2
Winonaites	2	2	2	2	2	2	2	2	2	2	1
IAB	4	4	4	1	4	4	1	4	1	1	4
Angrites	0	1	0	1	1	0	0	0	1	0	1
Aubrites	2	2	2	0	2	2	0	2	0	0	1
Eucrite	2	2	2	2	27	3	27	3	57	3	57
Diogenites	14	14	14	14	14	14	14	14	14	14	13
Howardites	7	7	7	7	13	10	13	10	14	10	13
Mesosiderites	3	3	2	1	8	6	4	5	5	2	9
Pallasites	0	0	0	0	1	1	0	1	0	0	1
IIE	2	2	2	2	3	3	2	3	2	2	3
IVA	0	0	0	0	0	1	0	0	0	0	1

Table 10.7: The number of group C (No correction).

	Mg/Si *vs.* Al/Si	Mg/Si *vs.* S/Si	Mg/Si *vs.* Ca/Si	Mg/Si *vs.* Fe/Si	Al/Si *vs.* S/Si	Al/Si *vs.* Ca/Si	Al/Si *vs.* Fe/Si	S/Si *vs.* Ca/Si	S/Si *vs.* Fe/Si	Ca/Si *vs.* Fe/Si	Number of Samples
CI	0	2	0	0	2	0	0	2	2	0	2
CM	0	3	0	0	3	0	0	3	3	0	24
CO	0	0	0	0	0	0	0	0	0	0	9
CV	3	0	2	3	3	3	3	2	3	3	12
CK	0	0	0	0	0	0	0	0	0	0	3
CR	0	0	0	0	0	0	0	0	0	0	2
H	0	0	0	0	0	0	0	0	0	0	229
L	0	0	0	0	0	0	0	0	0	0	256
LL	0	0	0	0	0	0	0	0	0	0	83
EH	0	1	0	0	1	0	0	1	1	0	4
EL	0	0	0	0	0	0	0	0	0	0	3
R	0	0	0	0	0	0	0	0	0	0	1
Ureilites	3	3	3	5	0	0	2	0	2	2	14
Brachinites	0	0	0	0	0	0	0	0	0	0	1
Acapulcoites	0	0	0	0	0	0	0	0	0	0	2
Lodranites	1	1	1	1	0	0	1	0	1	1	2
Winonaites	0	0	0	0	0	0	0	0	0	0	1
IAB	0	0	0	3	0	0	3	0	3	3	4
Angrites	2	1	2	1	1	2	2	2	1	2	1
Aubrites	0	0	0	2	0	0	2	0	2	2	1
Eucrite	56	56	56	56	31	55	31	55	1	55	57
Diogenites	0	0	0	0	0	0	0	0	0	0	13
Howardites	7	7	7	7	1	4	1	4	0	4	13
Mesosiderites	7	7	8	9	2	4	6	5	5	8	9
Pallasites	1	1	1	1	0	0	1	0	1	1	1
IIE	1	1	1	1	0	0	1	0	1	1	3
IVA	1	1	1	1	1	0	1	1	1	1	1

Table 10.8: The number of group A (High Iron correction).

	Mg/Si *vs.* Al/Si	Mg/Si *vs.* S/Si	Mg/Si *vs.* Ca/Si	Mg/Si *vs.* Fe/Si	Al/Si *vs.* S/Si	Al/Si *vs.* Ca/Si	Al/Si *vs.* Fe/Si	S/Si *vs.* Ca/Si	S/Si *vs.* Fe/Si	Ca/Si *vs.* Fe/Si	Number of Samples
CI	2	0	0	0	0	0	0	0	0	0	2
CM	22	0	0	0	0	0	0	0	0	0	24
CO	9	5	0	0	5	0	0	0	0	0	9
CV	9	2	0	0	2	0	0	0	0	0	12
CK	3	3	0	0	3	0	0	0	0	0	3
CR	1	2	0	0	1	0	0	0	0	0	2
H	111	100	41	1	47	19	1	12	0	0	229
L	100	128	34	0	41	14	0	14	0	0	256
LL	38	52	10	2	20	3	2	6	0	0	83
EH	0	0	0	0	0	3	0	0	0	0	4
EL	0	0	0	0	0	0	0	0	0	0	3
R	0	0	0	0	0	0	0	0	0	0	1
Urcilites	0	0	1	1	0	0	0	0	0	2	14
Brachinites	0	1	0	0	0	0	0	0	0	0	1
Acapulcoites	1	0	1	0	0	0	0	0	0	0	2
Lodranites	0	0	0	0	0	0	0	0	1	0	2
Winonaites	0	2	2	0	0	0	0	2	0	0	1
IAB	2	0	3	0	0	2	0	0	0	0	4
Angrites	0	0	0	0	0	0	0	0	0	0	1
Aubrites	0	0	2	0	0	0	0	0	0	0	1
Eucrite	0	0	0	0	0	0	20	0	0	0	57
Diogenites	0	0	0	0	0	0	0	0	0	8	13
Howardites	0	0	0	0	0	0	13	0	0	0	13
Mesosiderites	0	0	0	0	2	0	0	0	0	0	9
Pallasites	0	0	0	0	0	0	0	1	0	0	1
IIE	0	1	0	1	0	0	0	0	0	0	3
IVA	0	0	0	0	0	0	0	0	0	0	1

Table 10.9: The number of group B (High Iron correction).

	Mg/Si *vs.* Al/Si	Mg/Si *vs.* S/Si	Mg/Si *vs.* Ca/Si	Mg/Si *vs.* Fe/Si	Al/Si *vs.* S/Si	Al/Si *vs.* Ca/Si	Al/Si *vs.* Fe/Si	S/Si *vs.* Ca/Si	S/Si *vs.* Fe/Si	Ca/Si *vs.* Fe/Si	Number of Samples
CI	2	0	2	0	0	2	0	0	0	0	2
CM	24	3	24	0	3	24	0	3	0	0	24
CO	9	9	9	0	9	9	0	9	0	0	9
CV	9	12	9	2	9	9	1	9	2	1	12
CK	3	3	3	0	3	3	0	3	0	0	3
CR	2	2	2	0	2	2	0	2	0	0	2
H	229	224	229	1	224	229	1	224	1	1	229
L	256	256	256	3	256	256	3	256	3	3	256
LL	83	81	83	16	81	83	16	81	16	16	83
EH	4	0	4	0	0	4	0	0	0	0	4
EL	3	2	3	0	2	3	0	2	0	0	3
R	1	1	1	0	1	1	0	1	0	0	1
Ureilites	14	14	14	13	15	15	13	15	13	13	14
Brachinites	2	2	2	0	2	2	0	2	0	0	1
Acapulcoites	3	3	3	0	3	3	0	3	0	0	2
Lodranites	2	2	2	1	3	3	1	3	1	1	2
Winonaites	2	2	2	1	2	2	1	2	1	1	1
IAB	4	4	4	3	4	4	3	4	3	3	4
Angrites	1	1	0	0	2	0	1	0	1	0	1
Aubrites	2	2	2	0	2	2	0	2	0	0	1
Eucrite	0	0	0	0	57	1	57	1	58	1	57
Diogenites	14	14	14	14	14	14	14	14	14	14	13
Howardites	5	5	5	5	14	8	14	8	14	8	13
Mesosiderites	3	3	2	0	6	3	2	3	1	0	9
Pallasites	1	1	1	0	1	1	0	1	0	0	1
IIE	2	2	2	1	3	3	2	3	2	2	3
IVA	0	0	0	0	0	1	0	0	0	0	1

Table 10.10: The number of group C (High Iron correction).

	Mg/Si *vs.* Al/Si	Mg/Si *vs.* S/Si	Mg/Si *vs.* Ca/Si	Mg/Si *vs.* Fe/Si	Al/Si *vs.* S/Si	Al/Si *vs.* Ca/Si	Al/Si *vs.* Fe/Si	S/Si *vs.* Ca/Si	S/Si *vs.* Fe/Si	Ca/Si *vs.* Fe/Si	Number of Samples
CI	0	2	0	2	2	0	2	2	2	2	2
CM	0	21	0	24	21	0	24	21	24	24	24
CO	0	0	0	9	0	0	9	0	9	9	9
CV	3	0	3	10	3	3	11	3	10	11	12
CK	0	0	0	3	0	0	3	0	3	3	3
CR	0	0	0	2	0	0	2	0	2	2	2
H	0	5	0	228	5	0	228	5	228	228	229
L	0	0	0	253	0	0	253	0	253	253	256
LL	0	2	0	67	2	0	67	2	67	67	83
EH	0	4	0	4	4	0	4	4	4	4	4
EL	0	1	0	3	1	0	3	1	3	3	3
R	0	0	0	1	0	0	1	0	1	1	1
Ureilites	1	1	1	2	0	0	2	0	2	2	14
Brachinites	0	0	0	2	0	0	2	0	2	2	1
Acapulcoites	0	0	0	3	0	0	3	0	3	3	2
Lodranites	1	1	1	2	0	0	2	0	2	2	2
Winonaites	0	0	0	1	0	0	1	0	1	1	1
IAB	0	0	0	1	0	0	1	0	1	1	4
Angrites	1	1	2	2	0	2	1	2	1	2	1
Aubrites	0	0	0	2	0	0	2	0	2	2	1
Eucrite	58	58	58	58	1	57	1	57	0	57	57
Diogenites	0	0	0	0	0	0	0	0	0	0	13
Howardites	9	9	9	9	0	6	0	6	0	6	13
Mesosiderites	7	7	8	10	4	7	8	7	9	10	9
Pallasites	0	0	0	1	0	0	1	0	1	1	1
IIE	1	1	1	2	0	0	1	0	1	1	3
IVA	1	1	1	1	1	0	1	1	1	1	1

Table 10.11: The number of group A (Low Iron correction).

	Mg/Si *vs.* Al/Si	Mg/Si *vs.* S/Si	Mg/Si *vs.* Ca/Si	Mg/Si *vs.* Fe/Si	Al/Si *vs.* S/Si	Al/Si *vs.* Ca/Si	Al/Si *vs.* Fe/Si	S/Si *vs.* Ca/Si	S/Si *vs.* Fe/Si	Ca/Si *vs.* Fe/Si	Number of Samples
CI	2	0	0	0	0	0	0	0	0	0	2
CM	20	0	1	0	0	1	0	0	0	0	24
CO	8	4	1	0	5	1	0	0	0	0	9
CV	7	1	0	0	2	0	0	0	0	0	12
CK	3	3	0	0	3	0	0	0	0	0	3
CR	1	2	0	0	1	0	0	0	0	0	2
H	111	132	63	1	58	28	0	37	1	0	229
L	101	161	59	171	52	26	65	37	132	42	256
LL	37	63	18	73	23	7	30	15	60	16	83
EH	3	0	3	0	0	3	0	0	0	0	4
EL	0	0	2	2	0	0	0	0	0	2	3
R	0	0	0	0	0	0	0	0	0	0	1
Ureilites	0	0	0	0	0	0	0	0	0	7	14
Brachinites	0	1	0	1	0	0	0	0	1	0	2
Acapulcoites	1	0	1	2	0	0	1	0	0	1	3
Lodranites	0	0	0	0	0	0	0	0	0	0	3
Winonaites	0	2	2	2	0	0	0	2	2	2	2
IAB	2	1	2	0	1	2	0	1	0	0	4
Angrites	0	0	0	0	0	0	0	0	0	0	2
Aubrites	0	0	2	0	0	0	0	0	0	0	2
Eucrite	0	0	0	0	0	0	0	0	0	0	57
Diogenites	0	0	2	0	0	0	0	0	0	0	13
Howardites	0	0	0	0	0	0	0	0	0	0	13
Mesosiderites	0	0	0	0	2	0	0	0	0	0	10
Pallasites	0	0	0	0	0	0	0	1	0	0	1
IIE	0	1	0	0	0	0	0	0	0	0	3
IVA	0	0	0	0	0	0	0	0	0	0	1

Table 10.12: The number of group B (Low Iron correction).

	Mg/Si *vs.* Al/Si	Mg/Si *vs.* S/Si	Mg/Si *vs.* Ca/Si	Mg/Si *vs.* Fe/Si	Al/Si *vs.* S/Si	Al/Si *vs.* Ca/Si	Al/Si *vs.* Fe/Si	S/Si *vs.* Ca/Si	S/Si *vs.* Fe/Si	Ca/Si *vs.* Fe/Si	Number of Samples
CI	2	0	2	0	0	2	0	0	0	0	2
CM	24	5	24	21	5	24	21	5	4	21	24
CO	9	9	9	9	9	9	9	9	9	9	9
CV	9	12	10	10	9	9	9	10	10	10	12
CK	3	3	3	3	3	3	3	3	3	3	3
CR	2	2	2	1	2	2	1	2	1	1	2
H	229	226	229	159	226	229	159	226	159	159	229
L	256	256	256	256	256	256	256	256	256	256	256
LL	83	81	83	83	81	83	83	81	81	83	83
EH	4	0	4	1	0	4	1	0	0	1	4
EL	3	2	3	3	2	3	3	2	2	3	3
R	1	1	1	1	1	1	1	1	1	1	1
Ureilites	11	11	11	10	15	15	14	15	14	14	14
Brachinites	2	2	2	2	2	2	2	2	2	2	1
Acapulcoites	3	3	3	3	3	3	3	3	3	3	2
Lodranites	2	2	2	2	3	3	2	3	2	2	2
Winonaites	2	2	2	2	2	2	2	2	2	2	1
IAB	4	4	4	1	4	4	1	4	1	1	4
Angrites	1	1	0	1	2	0	2	0	2	0	1
Aubrites	2	2	2	0	2	2	0	2	0	0	1
Eucrite	2	2	1	2	57	1	57	1	58	1	57
Diogenites	14	14	14	14	14	14	14	14	14	14	13
Howardites	8	8	8	8	14	8	14	8	14	8	13
Mesosiderites	3	3	2	0	7	3	4	3	3	0	9
Pallasites	0	0	0	0	1	1	0	1	0	0	1
IIE	2	2	2	1	3	3	2	3	2	2	3
IVA	0	0	0	0	0	1	0	0	0	0	1

Table 10.13: The number of group C (Low Iron correction).

	Mg/Si *vs.* Al/Si	Mg/Si *vs.* S/Si	Mg/Si *vs.* Ca/Si	Mg/Si *vs.* Fe/Si	Al/Si *vs.* S/Si	Al/Si *vs.* Ca/Si	Al/Si *vs.* Fe/Si	S/Si *vs.* Ca/Si	S/Si *vs.* Fe/Si	Ca/Si *vs.* Fe/Si	Number of Samples
CI	0	2	0	2	2	0	2	2	2	2	2
CM	0	19	0	3	19	0	3	19	20	3	24
CO	0	0	0	0	0	0	0	0	0	0	9
CV	3	0	2	2	3	3	3	2	2	2	12
CK	0	0	0	0	0	0	0	0	0	0	3
CR	0	0	0	1	0	0	1	0	1	1	2
H	0	3	0	70	3	0	70	3	70	70	229
L	0	0	0	0	0	0	0	0	0	0	256
LL	0	2	0	0	2	0	0	2	2	0	83
EH	0	4	0	3	4	0	3	4	4	3	4
EL	0	1	0	0	1	0	0	1	1	0	3
R	0	0	0	0	0	0	0	0	0	0	1
Ureilites	4	4	4	5	0	0	1	0	1	1	14
Brachinites	0	0	0	0	0	0	0	0	0	0	1
Acapulcoites	0	0	0	0	0	0	0	0	0	0	2
Lodranites	1	1	1	1	0	0	1	0	1	1	2
Winonaites	0	0	0	0	0	0	0	0	0	0	1
IAB	0	0	0	3	0	0	3	0	3	3	4
Angrites	1	1	2	1	0	2	0	2	0	2	1
Aubrites	0	0	0	2	0	0	2	0	2	2	1
Eucrite	56	56	57	56	1	57	1	57	0	57	57
Diogenites	0	0	0	0	0	0	0	0	0	0	13
Howardites	6	6	6	6	0	6	0	6	0	6	13
Mesosiderites	7	7	8	10	3	7	6	7	7	10	9
Pallasites	1	1	1	1	0	0	1	0	1	1	1
IIE	1	1	1	2	0	0	1	0	1	1	3
IVA	1	1	1	1	1	0	1	1	1	1	1

Table 10.14: Groups of the best candidate meteorite-analogues to Itokawa (no correction)

	Mg/Si *vs.* Al/Si	Mg/Si *vs.* S/Si	Mg/Si *vs.* Ca/Si	Mg/Si *vs.* Fe/Si	Al/Si *vs.* S/Si	Al/Si *vs.* Ca/Si	Al/Si *vs.* Fe/Si	S/Si *vs.* Ca/Si	S/Si *vs.* Fe/Si	Ca/Si *vs.* Fe/Si
CI	A	C	B	B	C	B	B	C	C	B
CM	A	B	B	A	B	B	A	B	B	B
CO	A	A	B	A	A	B	A	B	A	B
CV	A	A	B	A	A	B	A	B	A	B
CK	A	B	B	A	B	B	A	B	B	B
CR	A	AB	AB	AB	AB	AB	AB	B	AB	B
H	A	A	A	A	A	A	A	A	A	A
L	A	A	A	A	A	A	A	A	A	A
LL	A	A	A	B	A	A	B	A	B	B
EH	B	B	B	B	B	A	B	B	B	B
EL	B	B	B	B	B	A	A	B	B	A
R	A	A	B	A	A	B	A	B	A	B
Ureilites	B	B	B	B	B	B	B	B	B	B
Brachinites	AB	AB	B	AB	AB	B	AB	B	AB	B
Acapulcoites	A	B	B	A	B	B	A	B	B	B
Lodranites	B	B	B	ABC	B	B	B	B	B	B
Winonaites	A	A	A	B	A	A	B	A	B	B
IAB	A	AB	A	C	AB	A	C	AB	C	C
Angrites	C	BC	C	BC	BC	C	C	C	BC	C
Aubrites	AB	B	A	C	B	AB	C	B	C	C
Eucrite	C	C	C	C	C	C	C	C	B	C
Diogenites	B	B	B	B	B	B	B	B	B	B
Howardites	BC	BC	BC	BC	B	B	B	B	B	B
Mesosiderites	C	C	C	C	B	B	C	BC	BC	C
Pallasites	C	C	C	C	B	B	C	B	C	C
IIE	A	ABC	ABC	B	B	B	B	B	B	B
IVA	C	C	C	C	C	B	C	C	C	C

Table 10.15: Groups of the best candidate meteorite-analogues to Itokawa (High Iron correction)

	Mg/Si *vs.* Al/Si	Mg/Si *vs.* S/Si	Mg/Si *vs.* Ca/Si	Mg/Si *vs.* Fe/Si	Al/Si *vs.* S/Si	Al/Si *vs.* Ca/Si	Al/Si *vs.* Fe/Si	S/Si *vs.* Ca/Si	S/Si *vs.* Fe/Si	Ca/Si *vs.* Fe/Si
CI	AC	B	ABC	B	C	B	ABC	B	ABC	B
CM	C	B	C	B	C	B	ABC	B	C	B
CO	AC	B	C	B	C	B	ABC	B	C	B
CV	AC	B	C	B	C	B	C	B	C	B
CK	AC	B	AC	B	C	B	ABC	B	AC	B
CR	C	B	AC	B	C	B	ABC	B	C	B
H	C	B	C	B	C	B	AC	B	C	B
L	C	B	C	B	C	B	C	B	C	B
LL	C	B	C	B	C	B	C	B	C	B
EH	C	B	ABC	B	C	B	ABC	B	ABC	B
EL	C	B	C	B	C	B	ABC	B	C	B
R	C	B	C	B	C	B	ABC	B	C	B
Ureilites	C	B	C	B	C	B	C	B	C	B
Brachinites	C	B	C	B	C	B	ABC	B	C	B
Acapulcoites	C	B	C	B	C	B	ABC	B	C	B
Lodranites	C	B	C	B	C	B	BC	B	C	B
Winonaites	C	B	AC	B	AC	B	C	B	C	B
IAB	C	B	C	B	C	B	C	B	C	B
Angrites	C	B	C	B	ABC	B	ABC	B	C	B
Aubrites	C	B	C	B	AC	B	ABC	B	C	B
Eucrite	ABC	B	B	B	ABC	B	ABC	B	C	B
Diogenites	C	B	C	B	C	B	C	B	C	B
Howardites	C	B	B	B	C	B	C	B	C	B
Mesosiderites	C	B	C	B	C	B	ABC	B	C	B
Pallasites	C	B	C	B	BC	B	ABC	B	C	B
IIE	C	B	C	B	C	B	AC	B	C	B
IVA	ABC	B	ABC	B	ABC	B	ABC	B	ABC	B

Table 10.16: Groups of the best candidate meteorite-analogues to Itokawa (Low Iron correction)

	Mg/Si *vs.* Al/Si	Mg/Si *vs.* S/Si	Mg/Si *vs.* Ca/Si	Mg/Si *vs.* Fe/Si	Al/Si *vs.* S/Si	Al/Si *vs.* Ca/Si	Al/Si *vs.* Fe/Si	S/Si *vs.* Ca/Si	S/Si *vs.* Fe/Si	Ca/Si *vs.* Fe/Si
CI	A	C	B	C	C	B	C	C	C	C
CM	A	C	B	B	C	B	B	C	C	B
CO	A	B	B	B	A	B	B	B	B	B
CV	A	B	B	B	B	B	B	B	B	B
CK	A	A	B	B	A	B	B	B	B	B
CR	AB	A	B	BC	AB	B	BC	B	BC	BC
H	B	A	B	B	B	B	B	B	B	B
L	B	A	B	A	B	B	B	B	A	B
LL	B	A	B	A	B	B	B	B	A	B
EH	A	C	A	C	C	A	C	C	C	C
EL	B	B	A	A	B	B	B	B	B	A
R	B	B	B	B	B	B	B	B	B	B
Ureilites	B	B	B	B	B	B	B	B	B	AB
Brachinites	B	AB	B	AB	B	B	B	B	AB	B
Acapulcoites	B	B	B	A	B	B	B	B	B	B
Lodranites	B	B	B	B	B	B	B	B	B	B
Winonaites	B	A	A	A	B	B	B	A	A	A
IAB	AB	B	AB	C	B	AB	C	B	C	C
Angrites	BC	BC	C	BC	B	C	B	C	B	C
Aubrites	B	B	A	C	B	B	C	B	C	C
Eucrite	C	C	C	C	B	C	B	C	B	C
Diogenites	B	B	B	B	B	B	B	B	B	B
Howardites	B	B	B	B	B	B	B	B	B	B
Mesosiderites	C	C	C	C	B	C	C	C	C	C
Pallasites	C	C	C	C	B	B	C	A	C	C
IIE	B	ABC	B	C	B	B	B	B	B	B
IVA	C	C	C	C	C	B	C	C	C	C

10.4 Comparison with the results of other instruments

Mineral composition has been estimated by the NIRS observation. The results of band absorption ratios (Abe *et al.*, 2006) are shown in Figure 10.19. This figure indicated the most similar meteorites or minerals to Itokawa are LL chondrites. These results support the results of our results.

The results of Olivine/(Olivine+Pyroxene) ratios by the NIRS are about 70%–80%. It implies that mineral composition of Itokawa is abundant of Olivine. This olivine rich feature implies that Itokawa may have experienced partial melting or impact heating before accretion. The partial melting feature has been reported by Abell *et al.*, (2006). The repeated impacts feature has been found in many meteorites. Folco *et al.* (2005) have reported that little melting feature due to impacts was found in LL ordinary chondrites rather than in H-ordinary chondrites. Thus, enrichment of Olivine feature of Itokawa may imply that the major composition of Itokawa is impact altered LL ordinary chondrites.

The material on the surface of Itokawa appears to be breccias. In many cases, a large fraction of meteorites samples are brecciated. For example, all CI chondrites, Mesosiderites, and Aubrites and over 80% of all HED meteorites are breccias of various kinds. Only four groups of stony meteorites lack clearly defined breccias: Angrites, Brachinites, Acapulcoites, and Lodranites. Thus the vast majority of coherent rocks in their parent bodies cannot be understood without an appreciation for the long history of impacts that were affected them.

Noguchi *et al.* (2007) have pointed out that the materials on the surface of Itokawa resemble brecciated rocks on the Itokawa in the closed up image of Itokawa, obtained by the AMICA. They suggest that close inspection of images of boulders revealed that 1/2 to 2/3 of them have morphology and texture similar to those of brecciated meteorites. The next abundant boulders ($\sim$1/3) display sharp crosscutting features which are probably shock veins. They are also coherent, monolithic boulders ($<$1/5). Also, Yano *et al.* (2006) have suggested that the surface of Itokawa favors brecciated rocks and/or a coarse-grain-filled surface because the thermal inertia (heat capacity $\times$ thermal diffusion length) of the materials on the Itokawa is $\Gamma = 10^2 \sim 10^3$ $\mathrm{Jm^{-2}s^{-0.5}K^{-1}}$ estimated by the thermometer on the XRS radiator (the surface temperature of 310 $\pm$ 10 K). Also the detailed results have been reported by Okada *et al.* (2006). These results have supported the ground based observation $\Gamma = 750$ $\mathrm{Jm^{-2}s^{-0.5}K^{-1}}$ (Müller *et al.*, 2005). Typical thermal inertia ($\mathrm{Jm^{-2}s^{-0.5}K^{-1}}$) has been summarized by Delbo *et al.*, (2007) in Table 10.17. Observation results indicate the materials of surface of Itokawa are like coarse sand or bare rock.

The brecciated features of Itokawa imply that Itokawa has experienced repeated impacts. In particular, many LL chondrites are breccias, and thus the composition of Itokawa may also LL chondrites.

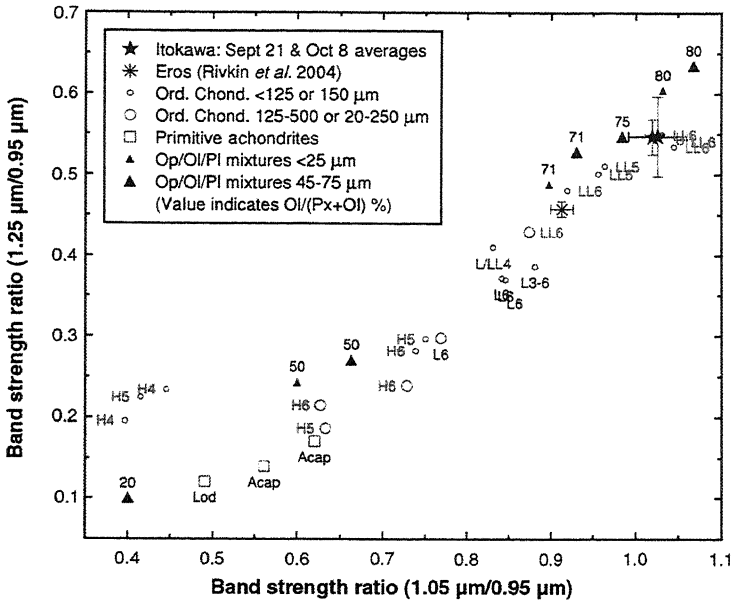

Figure 10.19: Natural log absorption strengths at 1.05 and 1.25 μm relative to that at 0.95 μm of average Itokawa spectra acquired by the NIRS in comparison with Eros (18), powder samples of ordinary chondrites, primitive achondrites Acapulcoites (Acap) and Lodranites (Lod), and orthopyroxene-olivine-plagioclase mixtures (15). This figure indicates that Itokawa has an olivine-rich mineral assemblage similar to LL5 and LL6 chondrites.

Table 10.17: Thermal inertia

Condition	Thermal inertia	ref.
Fine dust	$\sim$ 30	Putzig *et al.* (2005)
Lunar regolith	$\sim$ 50	Spencer *et al.* (1989)
Coarse sand	$\sim$ 400	Mellon *et al.* (2000); Christensen (2003)
Bare rock	$>$ 2500	Jakosky (1986)
Metal rich asteroidal fragments	$>$ 12000	Farinella *et al.* (1998)

10.5 Speculation for Origin of Itokawa

The origin of Itokawa is uncertain but the parent body of Itokawa can be pictured, and there are some hints: (1) Itokawa is a rubble-pile structure but rocks are difficult to assemble in small bodies as shown in Figure 10.20. (2) The observation results of XRS indicate that the surface major elemental composition is homogeneous. (3) The macroporosity of Itokawa is near that of near-Earth objects as shown in Figure 1.14.

The mass of Itokawa, measured by the orbits of Itokawa, is very small ($3.51\pm0.105\times10^{10}$ kg) and its density is also small. The macroporosity, corresponding with that of Itokawa, is not found in that of ever explored S-type asteroid. There are three general groups: (1) unaltered solid object, (2) macroporosities $\sim$20% (probably heavily fractured) and (3) macroporosities $>$30% (loosely consolidated "rubble-pile" structures).

Asteroid masses have been determined from asteroid–asteroid perturbation observing the trajectory deviation of another asteroid. Also, asteroid masses have been determined from

perturbation tracking the motion of a spacecraft in orbit by the doppler ranging. Volumes of asteroid are often mainly estimated by its shape observed with the Infrared Astronomical Satellite (IRAS). Also bulk density is estimated from these masses and volumes, including large uncertainties. Since the the AMICA onboard Hayabusa took close up images (Saito *et al.*, 2006), and made the detail shape model (Gaskell *et al.*, 2006), its density should be certain.

Porosity P, defined as a void ratio, is represented as volume ratios of bulk volume $V_{\rm bulk}$ and net volume $V_{\rm net}$ of rocks as follows,

$$P = 1 - \frac{V_{\rm net}}{V_{\rm bulk}} = 1 - \frac{\rho_{\rm bulk}}{\rho_{\rm net}}.$$

In order to estimate the porosity of asteroids, the density is assumed to be represented as typical density of meteorites (see Table 10.18). Thus, the porosity of asteroid P_A, called a macro-porosity, is written as follows,

$$P_A = 1 - \frac{\rho_A}{\rho_M}, \tag{10.2}$$

where ρ_A is the bulk density of asteroid, and ρ_M is the typical density of meteorite which is not grain density but average bulk density because the grain also has porosity itself.

The macroporosity of Itokawa can also be calculated as mentioned above. Table 10.19 shows the probable macroporosity of Itokawa. The density of Itokawa was assumed to be 1.9 ± 0.13 (g/cm^3). In order to determine the macroporosity of Itokawa, the average porosity was assumed to be the average value of ordinary chondrites in Table 10.18.

Typical grain density of a clay, mafic silicate pyroxene and olivine, and Ni-Fe, is 2.2–2.6, 3.2–4.37, and 7.3–7.7 (g/cm^3), respectively. The density, measured by spacecraft, is bulk density which is the mass of an object divided by its volume. The ratio between grain and bulk density represents the porosity. The mass of Itokawa is $3.51 \pm 0.105 \times 10^{10}$ kg. The mean density of Itokawa is 1.9 ± 0.13 g/cm^3. The porosity of Itokawa is calculated as follows,

$$1 - \frac{\rho_B}{\rho_B} = 1 - \frac{1.9}{3.2} = 0.41,$$

where typical densities of S-class asteroid were obtained (*e.g.*, Britt *et al.*, 2001). The macro-porosity of Itokawa appears to be similar to that of a rubble-pile asteroid in the main belt or near-Earth, where the density of ordinary chondrites or achondrites was assumed to be 3.23 ± 0.19 g/cm^3.

The stony asteroids might have experienced impact shocks (*e.g.*, Consolmagno and Britt, 2004) before accretion. These heating or melting features may teach us a thermal history on the parent body of asteroids. Petrologic types of 5 or 6, measured by the NIRS with 2 μm absorption band, are the evidence of heating alteration in Itokawa. Probably, many near-Earth objects have small mass and small density, and thus they may be composed of rubble-piles due to impacts.

McCoy *et al.* (2000) have suggested that reduction process, varied in the location of the solar system, may not be concerned with element ratios, *i.e.* average elemental composition of asteroids represent that of parent body. The observation results indicate that Mg and Si are compositionally homogeneous on the surface of Itokawa, and average compositions are like ordinary chondrites. Thus, the elemental composition of Itokawa may almost primitive composition as same as the early solar system.

About a decade ago, small bodies are considered igneous rock (*e.g.*, Bell *et al.*, 1989), and thus it is considered the portions of a differentiated small planet. However, results of this study indicate that the composition of Itokawa is primitive but surface is a little bit altered. Hence,

impact iteration may make small objects like Itokawa. In particular, chaotic kinetic force in Kirkwood gap will cause emigrant of ordinary chondrite to earth. In contrast large main belt asteroid is probably fractured coherent rocks like Eros.

Wilkison *et al.*, (2002) have summarized inner structure made for the parent body of asteroids in Figure 10.21. (A) The differentiated model. The asteroid is composed of undifferentiated chondritic material. (B) The onion shell model. The chondritic parent body exhibits successive layers of petrologic type 3 through 6. (C) The heterogeneously heated model. The different petrologic types of rocks dispersed randomly through the parent body due to heterogeneous heating. (D) The metamorphosed planetesimal model. Small unconsolidated chondrite planetesimal accreted into a larger parent body. (E) The differentiated model.

The mass and density of Itokawa are very small (mass: $3.51 \pm 0.105 \times 10^{10}$ kg, density: 1.9 ± 0.13 g/cm^3), and thus these imply that Itokawa is composed of rubble-piles. The observation results indicated the elemental abundance of Itokawa is like ordinary chondrites and elemental distribution appears to be globally homogeneous. It implies that Itokawa was assembled of elementally homogeneous rocks. However, the mass of Itokawa is too small to assemble the fractured portions by impacts (*e.g.*, Figure 10.20 as shown in Figure 10.20). Thus Itokawa may a portion of rubble-pile, structured the parent body, and then probably the inner structures is homogeneous, classified in (A) as shown in Figure 10.21.

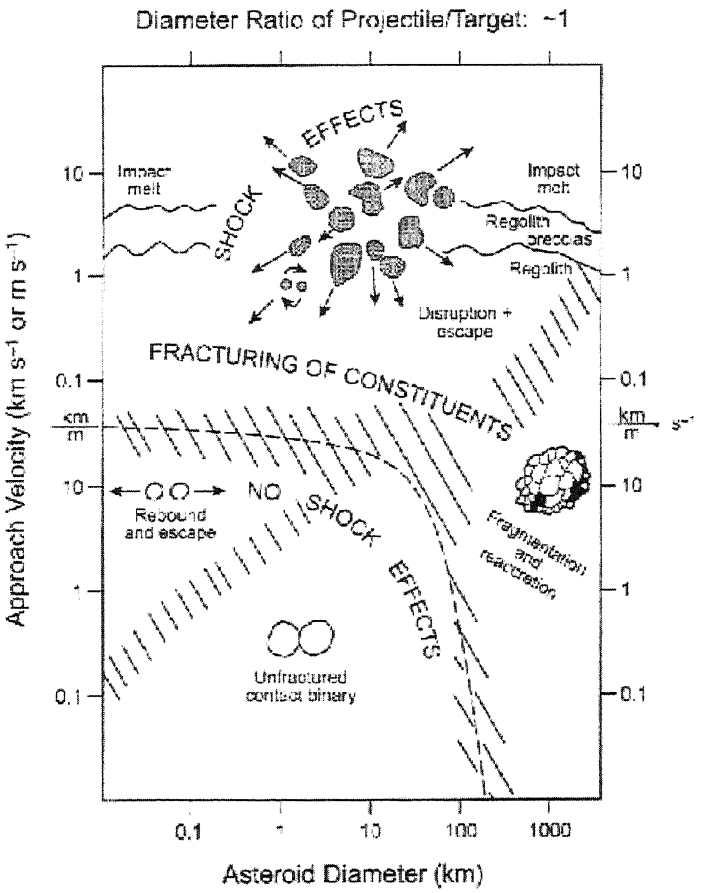

Figure 10.20: Bischoff *et al.*, 2006

Table 10.18: Typical densities of meteorites (Britt *et al.*, 2002).

Meteorite type	Grain density (g/cm^3)	Average bulk density (g/cm^3)	Average porosity (%)
H ordinary chondrites	3.84	3.40	11.5
L ordinary chondrites	3.75	3.34	10.8
LL ordinary chondrites	3.56	3.19	10.4
Achondrites	3.20	2.97	7.0
CI carbonaceous chondrites	2.27	2.12	11
CM carbonaceous chondrites	2.71	2.21	12
CR carbonaceous chondrites	3.11	3.15	6
CV carbonaceous chondrites	3.51	3.10	11
CO carbonaceous chondrites	3.69	3.11	16

Table 10.19: Probable macroporosity of Itokawa.

Candidate meteorites	Macroporosity of Itokawa (%)
H ordinary chondrites	44
L ordinary chondrites	43
LL ordinary chondrites	40
Achondrites	36

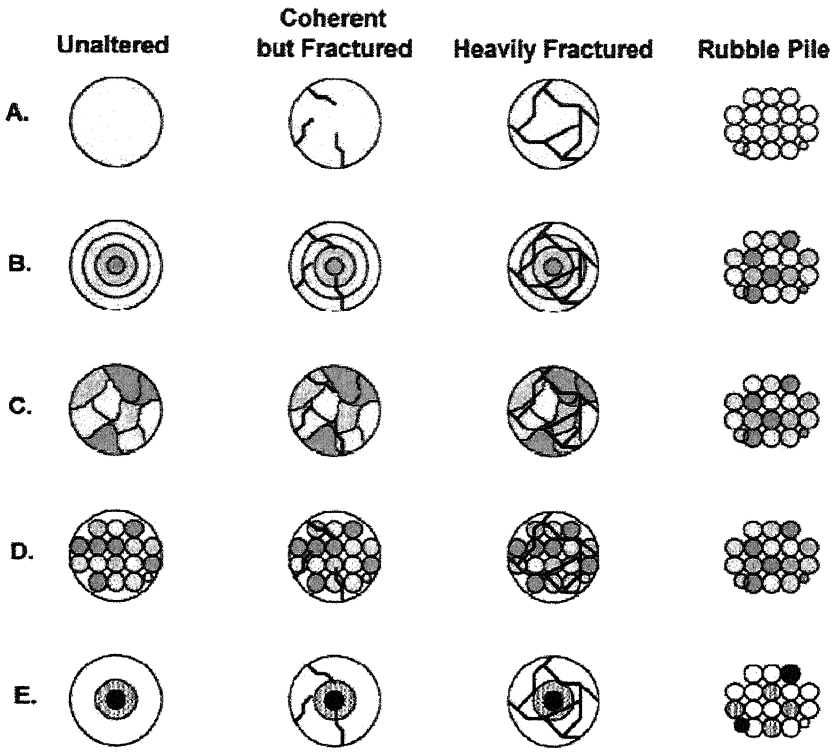

Figure 10.21: Cross section of an unaltered, fluctuated, rubble-pile asteroid schematically from Wilkison *et al.* (2002). Colors represent different ordinary chondrite petrologic types. Yellow represents petrologic type 3, red represents type 4, blue represents type5 and green represents type 6. (A) The differentiated model. The asteroid is composed of undifferentiated chondritic material. (B) The onion shell model. The chondritic parent body exhibits successive layers of petrologic type 3 through 6. (C) The heterogeneous heated model. The petrologic types dispersed randomly through the parent body due to heterogeneous heating. (D) The metamorphosed planetesimal model. Small unconsolidated chondrite planetesimals accrete into a larger parent body. (E) The differentiated model.

Chapter 11

Conclusions

In this paper, analysis of X-ray fluorescence observation of asteroid 25143 Itokawa with the X-ray fluorescence spectrometer onboard Hayabusa (XRS) was carried out. Major elemental mass fractions on the surface of Itokawa, such as Mg, Al, Si, S, Ca, and Fe were estimated and they were related to the possible meteorite-analogues. Also, the origin and evolution of Itokawa were discussed.

In this analysis, corrections are carefully carried out to the response function as sensor characteristics, the temporal fluctuation of incident solar X-rays, and the variation of surface geometry of Itokawa. Since the failure of reaction wheels of Hayabusa caused not only the decrease of observation duration but also the degradation of energy resolution due to frequent thermal changes of XRS, many observation data happened to include instrumental noises. Thus, only a small amount of significant data obtained under appropriate conditions were extracted to be analyzed from all the observation data.

The results of analysis indicate that major elemental composition of the surface materials of Itokawa resembles that of chondrite-analogues. In particular, the results indicate that the elemental mass ratios are a follows: (1) The lemental mass ratio of Fe/Si is larger than that of average composition of ordinary chondrites but the result of the correction with mineral mixing effect indicates that the Fe/Si ratio is nearly equal to that of average ratios of ordinary chondrites. (2) The lemental mass ratio of Mg/Si is globally homogeneous on the surface of Itokawa. (3) The lemental mass ratios of Al/Si and S/Si may slightly vary at local areas, and the corrected results with mineral mixing effect indicate elemental mass ratio of S/Si is less than, or same as that of average composition of ordinary chondrites in terms of the best-fit results. (4) Although estimation errors are large, the elemental mass ratios of Al/Si and Ca/Si appear to be larger than those of average composition of ordinary chondrites.

The results of elemental classifications for elemental mass ratios of Mg/Si, Al/Si, S/Si, Ca/Si and Fe/Si indicate that IAB irons as metallic Fe-rich meteorites are ruled out as the candidates of meteorite-analogues of Itokawa, an S(IV) subtype asteroids of the classification by Gaffey *et al.* (1993). It implies that Itokawa is not a metallic Fe-rich asteroid. Also most probable candidates for Itokawa are ordinary L or LL chondrites, EL chondrites, or primitive achondrites such as Brachinites, Acapulcoites or Winonaites when elemental mass ratios of Mg/Si vs. Fe/Si are compared between those of Itokawa and meteorite-analogues. It implies that major elemental composition of Itokawa is similar to that of primitive meteorites.

These results imply that the reason of reddened and darkened features of visible and near infrared reflectance spectrum, obtained by ground-based and the NIRS observation, is preferably by space weathering rather than the mixtures of metallic Fe materials on the surface. If so Itokawa is probably a surface altered asteroid by space weathering. Since Itokawa is probably a ubiquitous asteroid, many small bodies also should have altered their surface by space weathering.

Regional distribution of the mass ratio of S/Si on the local areas implies that surface alteration might occur on Itokawa. Energetic erosion on the surface materials due to solar wind sputtering, which is one of phenomena of space weathering, was calculated by the method of Kracher and Sears (2005). This result shows that it is easy to take away sulfur on the surface, and also volatile elements may be evaporated by space weathering on the surface of Itokawa. This result indicates that volatile elements on the surface may be globally depleted. However, the analysis shows that sulfur is not globally depleted and has regional distribution. Resurfacing on Itokawa due to seismic destruction by impacts and/or tidal destruction by planets encounter might cause such surface heterogeneity. If so only the surface material on Itokawa might be altered but the inner materials remain fresh.

Partial melting events on the parent body of Itokawa can not be ruled out. The results of elemental analysis indicate that elemental mass fractions of Al and Ca on the surface appear to be more enriched than those of average composition of ordinary chondrites. These features appear to be the evidence of partial melting on the parent body of Itokawa. Partial melting of rocks causes the fraction of enrichment of Al and Ca. In that case, Itokawa may be composed of the portions that were affected by partial melting in the parent body.

The average density of Itokawa was found very small, measured by the trajectory of Hayabusa. It implies that Itokawa may be a rubble-pile. The results of elemental analysis indicate that mass distribution of major elemental composition on the surface is globally homogeneous, in terms of the elemental mass ratio of Mg/Si. It implies that Itokawa was assembled by compositionally homogeneous rocks. Since accretion of small rocks is difficult in micro gravity, Itokawa may be substantial rubble-piles. The parent body of Itokawa may also be structured from a rubble-pile.

Decades ago, small bodies in the near-Earth were considered as igneous rocks because most found meteorites in Earth were altered, and they were considered as the portions of a differentiated planetesimal. The result of analysis of Itokawa indicates that elemental composition is most consistent with that of ordinary chondrites. If Itokawa is the parent body of ordinary chondrites, major elemental composition of many primitive bodies in S(IV) subtype asteroid are able to be estimated, which is the large progress in asteroid science and be may in science of the solar system.

Acknowledgments

The author gratefully thanks Professor Kato, M. Professor Okada, T., Professor Tanaka, and S. Professor Kato encourages the author everyday. Professor Okada teaches the author about all things for scientist. Professor Tanaka also teaches the author about the way of the scientist. The author gratefully thanks Dr. Yamamoto, Y., Mr. Shirai, K., and Mr. Ogawa, K.. They help the author for the analysis of this paper. The author also thanks all members of solid state planetary science division is ISAS/JAXA. Also, the author thanks project team members of the Hayabusa mission.

References

[1] ASCA Guest Observer Facility, The ASCA Data Reduction Guide (Otherwise known as the ABC Guide) Version 2.0, Laboratory for High Energy Astrophysics, NASA/Goddard Space Flight Center, http://heasarc.gsfc.nasa.gov/docs/asca/abc/abc.html, 2002.

[2] ASCA/SIS Non-X-ray background, Private communication with ASCA team.

[3] Abe, M., Takagi, Y., Kitazato, K., Abe, S., Hiroi, T., Vilas, F., Clark, B. E., Abell, P. A., Lederer, S. M., Jarvis, K. S., Nimura, T., Ueda, Y., Fujiwara, A., Near-Infrared Spectral Results of Asteroid Itokawa from the Hayabusa Spacecraft, *Science*, **312**, 1334–1338, 2006.

[4] Adler, I., Trombka, J., Gerard, J., Lowman, P., Schmadebeck, R., Blodget, H., Eller, E., Yin, L., Lamothe, R., Gorenstein, P., Bjorkholm, P., Apollo 15 Geochemical X-ray Fluorescence Experiment: Preliminary Report, *SCIENCE*, **175**, 436–440, 1972.

[5] Adler, I., Trombka, J. I., Schmadebeck, R., Lowman, P., Blodget, H., Yin, L., Eller, E., Podwysocki, M., Weidner, J. R., Bickel, A. L., Lum, R. K. L., Gerard, J., Gorenstein, P., Bjorkholm, P., and Harris, B., Results of the Apollo 15 and 16 X-ray experiment, *Proc. of Lunar Sci. Conf.*, **4**, 2783–2791, 1973.

[6] Akagawa, K., Master thesis of The University of Tokyo (in Japanese), 2003.

[7] Anders, E., and Grevesse N., Abundances of the elements – Meteoritic and solar, *Geochim. et Cosmochim. Acta*, **53**, 197–214, 1989.

[8] Arai, T., Master thesis of Tokyo Institute of Technology, 2003.

[9] Arai, T., Yamamoto, Y., Okada, T., Shirai, K., and Kato, M., In-flight calibration for XRS onboard MUSES-C, *Proc. of the 35th ISAS Lunar and Planetary symposium*, 88, 2002.

[10] Arnaud, K., Dorman, B., and Gordon, C., Xspec An X-ray Spectral Fitting Package User's Guide for version 12.2, HEASARC, Exploration of the Universe Division, NASA/GSFC, 2005.

[11] Bearden, J. A., X-Ray Wavelengths, *Rev. Mod. Phys.*, **39**, 78–124, 1967.

[12] Bevington, P., and R., Robinson, D. K., Testing The Fit, in *Data Reduction and Error Analysis for the Physical Sciences*, 3rd Ed., 320 pp, McGraw-Hill, New York, 2003.

[13] Binzel, Richard P., Rivkin, Andrew S., Bus, Schelte J., Sunshine, Jessica M., Burbine, Thomas H., MUSES-C target asteroid (25143) 1998 SF36: A reddened ordinary chondrite, *Meteoritics & Planetary Science*, **36**, no. 8, 1167–1172, 2001.

[14] Bus, S. J.; Binzel, R. P., Phase II of the Small Main-Belt Asteroid Spectroscopic Survey A Feature-Based Taxonomy, *Icarus*, **158**, Issue 1, 146–177, 2000.

[15] Chantler, C.T., Olsen, K., Dragoset, R.A., Chang, J., Kishore, A.R., Kotochigova, S.A., and Zucker, D.S., 2005, X-Ray Form Factor, Attenuation and Scattering Tables (version 2.1). [Online] Available: http://physics.nist.gov/ffast [2006, October 25]. National Institute of Standards and Technology, Gaithersburg, MD. Originally published as Chantler, C.T., J. Phys. Chem. Ref. Data **29**(4), 597-1048, 2000; and Chantler, C.T., J. Phys. Chem. Ref. Data **24**, 71-643, 1995.

[16] Chapman, Clark R., S-Type Asteroids, Ordinary Chondrites, and Space Weathering: The Evidence from Galileo's Fly-bys of Gaspra and Ida, *Meteoritics*, **31**, 699–725, 1996.

[17] Clark, P. E. and Trombka, J. I., Remote X-ray spectrometry for NEAR and Future missions: Modeling and analyzing X-ray production from source to surface, *JGR*, **102**, E7, 16361–16384, 1997.

[18] Compton, A. H., and Allison, S. K., X-Rays in Theory and Experiment 2nd ed., 737 pp., D. Van Nostrand, New York, 1935.

[19] Demura, H., Kobayashi, S., Nemoto, E., Matsumoto, N., Furuya, M., Yukishita, A., Muranaka, N., Morita, H., Shirakawa, K., Maruya, M., Ohyama, H., Uo, M., Kubota, T., Hashimoto, T., Kawaguchi, J., Fujiwara, A., Saito, J., Sasaki, S., Miyamoto, H., Hirata, N., Pole and Global Shape of 25143 Itokawa, *Science*, **312**, 1347–1349, 2006.

[20] Feldman, U, Doschek, A. G., Behring, W. E., and Phillips, K. J. H., ELECTRON TEMPERATURE, EMISSION MEASURE, AND X-RAY FLUX IN A2 TO X2 X-RAY CLASS SOLAR FLARES, *APJ*, **460**, 1034-1041, 1996.

[21] Fujiwara, A., Abe, M., Takagi, Y., Kitazato, K., Abe, S., Hiroi, T., Vilas, F., Clark, B. E., Abell, P. A., Lederer, S. M., Jarvis, K. S., Nimura, T., Ueda, Y., and Fujiwara, A., Near-Infrared Spectral Results of Asteroid Itokawa from the Hayabusa Spacecraft, *Science*, **312**, 1334–1338, 2006.

[22] Gaffey, Michael J.; Burbine, Thomas H.; Piatek, Jennifer L.; Reed, Kevin L.; Chaky, Damon A.; Bell, Jeffrey F.; Brown, R. H., Mineralogical variations within the S-type asteroid class, Icarus, vol. 106, p. 573, 1993.

[23] Gaskell, R.; Saito, J.; Ishiguro, M.; Kubota, T.; Hashimoto, T.; Hirata, N.; Abe, S.; Barnouin-Jha, O. S.; Scheeres, D., Global Topography of Asteroid 25143 Itokawa, 37th Annual Lunar and Planetary Science Conference, March 13-17, League City, Texas, abstract no.1876, 2006.

[24] http://www.sec.noaa.gov/.

[25] HEASARC's web page, http://heasarc.gsfc.nasa.gov/docs/asca/gis_night_earth/gis_night_earth.html.

[26] Hapke, B.,Space weathering from Mercury to the asteroid belt, *JGR*, **106**, Issue E5, 10039–10074, 2001.

[27] Hayabusa's web site, http://hayabusa.sci.isas.jaxa.jp/.

[28] Hubbell, J. H., Photon Cross Sections, Attenuation Coefficients, and Energy Absorption Coefficients from 10 keV to 100 GeV, NSRDS-NBS, **29**, Nat. Bur. Stand., Washington D.C., 1969.

[29] Imanishi, K., Awaki, H., Tsuru, T.G., Hamaguchi, K., Murakami, H., Nishiuchi, M., and Koyama, K., High-energy Performance of X-ray Imaging Spectrometers onboard Astro-E, *Proc. SPIE*, **4012**, 137, 2000.

[30] Ishiguro, M. I., Hiroi, T. H., Tholen, D. J. T., Yamamoto, A. Y., Sasaki, S. S., Yoshida, F. Y., Clark, B. E., Nakamura, R. N., Saito, J. S., Detection of a Large Variation in the Degree of Space Weathering on the Surface of Itokawa by Hayabusa/AMICA Observations, *LPI*, **37**, 2006.

[31] Janesick, J., Elliott, T., Collins, S., Daud, T., Campbell, D., Dingizian, A., CCD advances for X-ray scientific measurements in 1985, *Proc. SPIE*, **597**, 364-380, 1985.

[32] Jarosewich, E., Chemical analyses of meteorites at the Smithsonian Institution: An update, *M&PS*, **41**, issue 9, 1271–1419, 2006.

[33] Jenkins, R., Gould, R. W., and Gedcke, D., The interaction of X-rays with Matter, in *Quantitative X-ray Spectrometry 2nd Ed.*, Edited by Brame, E. G, Jr., 504 pp., Marcel Dekker, Inc, New York·Basel·Hong Kong, 1995.

[34] Kaasalainen, T. Kwiatkowski, M. Abe, J. Piironen, T. Nakamura4, Y. Ohba, B. Dermawan, T. Farnham, F. Colas, S. Lowry, P. Weissman, R. J. Whiteley, D. J. Tholen, S. M. Larson, M. Yoshikawa, I. Toth and F. P. Velichko, CCD photometry and model of MUSES-C target (25143) 1998 SF36, A&A, 2003.

[35] Katayama, H. *et al*, X-ray imaging Spectrometers for ASTRO-E: Ground Calibration in soft X-ray range. Proc. SPIE **4012**, 123, 2000.

[36] Killen, R. M., Depletion of sulfur on the surface of asteroids and the moon, *M&PS*, **38**, no. 3, p.383-388, 2003.

[37] Knoll, G. F., Counting Statistics and Error Prediction, in *Radiation detection and measurement 3rd ed.*, 802 pp., Wiley, New York, 2000.

[38] Kracher A., and Sears D.W.G., Space weathering and the low sulfur abundance of Eros, *ICARUS*, **174** no. 1, 36–45, 2005.

[39] Krause, M. O., Atomic radiative and radiationless yields for K and L shells, *J. Phys. Chem. Ref. Data*, **8**, 307–327, 1979.

[40] Lederer, S. M., Domingue, D. L., Vilas, F., Abe, M., Farnham, T. L., Jarvis, K. S., Lowry, S. C., Ohba, Y., Weissman, P. R., French, L. M., Fukai, H., Hasegawa, S., Ishiguro, M., Larson, S. M., and Takagi, Y., Physical characteristics of Hayabusa target Asteroid 25143 Itokawa, *Icarus*, **173**, Issue 1, 153–165, 2005.

[41] Maruyama, Y., Ogawa, K., Okada, T., and Kato, M., Particle Size Effect in X-Ray Fluorescence and Its Implication to Planetary XRF Spectroscopy, *LPI*, **1338**, 2007.

[42] Maslen, E. N., Fox, A. G., and O'Keefe, M. A., X-ray scattering in *International Table for Crystallography, Vol. C 3rd Ed.*, Edited by Prince, E., 1000+xxxii pp., NIST Center for Neutron Research, National Institutes of Standards and Technology, Gaithersburg, USA, 2004.

[43] Masuda, E., Elemental composition analysis of asteroid surface using X-ray spectrometer, Master thesis of Tokyo institute of technology, 2002.

[44] McCoy, T. J., Burbine, T. H., McFadden, L. A., Starr, R. D., Gaffey, M. J., Nittler, L. R., Evans, L. G., Izenberg, N., Lucey, P., Trombka, J. I., Bell, J. F., III, Clark, B. E., Clark, P. E., Squyres, S. W., Chapman, C. R., Boynton, W. V., Veverka, J., The composition of 433 Eros: A mineralogical-chemical synthesis, *M&PS*, **36** no. 12, 1661–1672, 2001.

[45] Mewe, R., Gronenschild, E. H. B. M., van den Oord, G. H. J., Calculated X-radiation from optically thin plasmas. V, *A&AS*, **62**, 197–254, 1985.

[46] Michel, P., and Yoshikawa, M., Earth impact probability of the Asteroid (25143) Itokawa to be sampled by the spacecraft Hayabusa, *Icarus*, **179**, Issue 2, 291–296, 2005.

[47] Miyata, E., Dotani, Ozaki, M., Bautz, M., Doty, J., Kissel, S., Foster, R., Ricker, G., The hard X-ray response of the XIS-CCD for Astro-E: qualification of the X-ray CCD detector, *Nuclear Instruments and Methods in Physics Research A*, **436**, 79-94, 1999.

[48] Morrison, R., and McCammon D., Interstellar Photoelectric Absorption Cross Sections, 0.03-10 keV, *A*PJ, **270**, 119, 1983.

[49] Müller T. G., T. Sekiguchi, M. Kaasalainen, M. Abe, and S. Hasegawa,Thermal infrared observations of the Hayabusa spacecraft target asteroid 25143 Itokawa *A&A*, **443**, 347–355, 2005.

[50] NOAA / National Weather Service web site, http://www.sec.noaa.gov.

[51] Nishiuchi, M. Koyama, K., Awaki, H., Tsuru, T., Sakano, M., Hamaguchi, K., Murakami, H, Tsunemi, H., Hayashida, K., Kitamoto, S., The response function of an X-ray CCD camera onboard the Astro-E satellite, Proc. SPIE, **3445**, 268, 1998.

[52] Nittler, L. R., Starr, R. D., Lim, L., McCoy, T. J., Burbine, T. H., Reedy, R. C., Trombka, J. I., Gorenstein, P., Squyres, S. W., Boynton, W. V., McClanahan, T. P., Bhangoo, J. S., Clark, P. E., Murphy, M. E., Killen, R., X-ray fluorescence measurements of the surface elemental composition of asteroid 433 Eros, *M&PS*, **36** no. 12, 1673-1695, 2001.

[53] Okada, T., Basic study for XRF spectrometry of Planetary Surfaces, Ph. D Thesis, Univ. of Tokyo, 1995

[54] Okada, T., K. Shirai, Y. Yamamoto, T. Arai, K. Ogawa, K. Hosono, and M. Kato, Instrumentation and observations of the X-ray spectrometer onboard Hayabusa. in Advances in Geosciences, **3**: Planetary Science (PS), Edited by A. Bhardwaj, World Scientific, Singapore, 231–240, 2006b.

[55] Okada, T., Kato, M., Fujimura, A., Tsunemi, H., and Kitamoto, S., X-ray fluorescence spectrometer onboard Muses-C, *AdSpR*, **25**, Issue 2, p. 345–348, 2000.

[56] Okada, T., Shirai, K., Yamamoto, Y., Arai, T., Ogawa, K., Hosono, K., and Kato, M., X-ray Fluorescence Spectrometry of Asteroid Itokawa by Hayabusa, *Science*, **312**, 1338–1341, 2006a.

[57] Okada, T., and Kuwada, Y. Proc. Effect of surface roughness on X-ray fluorescence emission from planetary surfaces, *LPI*, **28**, 1997.

[58] Ostro, Steven J., Benner, Lance A. M., Nolan, Michael C., Magri, Christopher; Giorgini, Jon D., Scheeres, Daniel J., Broschart, Stephen B., Kaasalainen, Mikko, Vokrouhlicky, David, Chesley, Steven R., Margot, Jean-Luc, Jurgens, Raymond F., Rose, Randy, Yeomans, Donald K., Suzuku, Shigeru, de Jong, Eric M,Radar observations of asteroid 25143 Itokawa (1998 SF36), *Meteoritics & Planetary Science*, **39**, No. 3, 407–424, 2004.

[59] Press, W. H., Teukolsky, S. A., Vetterling, W. T., and Flannery, B. P., Minimization or Maximization of Functions in *Numerical Recipes in C++ 2nd Ed.*, Edited by Press, W. H., Cambridge University Press, Cambridge, 1002 pp., 2002.

[60] Press, W. H., Teukolsky, S. A., Vetterling, W. T., and Flannery, B. P., Modeling of Data in *Numerical Recipes in C++ 2nd Ed.*, Edited by Press, W. H., Cambridge University Press, Cambridge, 1002 pp., 2002.

[61] ROSAT All Sky Survey, NASA'S HEASARC, http://heasarc.gsfc.nasa.gov/cgi-bin/Tools/xraybg/xraybg.pl.

[62] Raymond, J. C., and Smith, B. W., Soft X-ray Spectrum of A Hot Plasma, *ApJS*, **35**, 419–439, 1977.

[63] Rikanenpyo, National Astronomical Observatory of Japan, 2002.

[64] Saito, J., Miyamoto, H., Nakamura, R., Ishiguro, M., Michikami, T., Nakamura, A. M., Demura, H., Sasaki, S., Hirata, N., Honda, C., Yamamoto, A., Yokota, Y., Fuse, T., Yoshida, F., Tholen, D. J., Gaskell, R. W., Hashimoto, T., Kubota, T., Higuchi, Y., Nakamura, T., Smith, P., Hiraoka, K., Honda, T., Kobayashi, S., Furuya, M., Matsumoto, N., Nemoto, E., Yukishita, A., Kitazato, K., Dermawan, B., Sogame, A., Terazono, J., Shinohara, C., and Akiyama, H., Detailed Images of Asteroid 25143 Itokawa from Hayabusa, *Science*, **312**, 1341–1344, 2006.

[65] Sasaki, S., Saito, J., Ishiguro, M., Hirata, N., Miyamoto, H., Demura, H., Hashimoto, T., Higuchi, Y., Hiraoka, K., Honda, C., Honda, T., Kitazato, K., Kubota, T., Michikami, T., Nakamura, A. M., Nakamura, R., Nakamura, T., Smith, P., Terazono, J., Tholen, D. J., Yamamoto, A., Yokota, Y., Akiyama, H., Dermawan, B., Fuse, T., Shinohara, C., Sogame, A., Yoshida, F., and AMICA Team, Observations of 25143 Itokawa by the Asteroid Multiband Imaging Camera (AMICA) of Hayabusa: Morphology of Brighter and Darker Areas, *LPI*, **37**, 2006.

[66] Scott, E. R. D., Meteoritical and dynamical constraints on the growth mechanisms and formation times of asteroids and Jupiter, *Icarus*, **185**, Issue 1, 72–82, 2006.

[67] Shiraiwa and Fujino, Theoretical Calculation of Fluorescent X-Ray Intensities in Fluorescent X-Ray Spectrochemical Analysis, *Jpn. J. Appl. Phys.*, **5**, 886–899, 1966.

[68] Shu, Frank H., Shang, Hsien, Lee, Typhoon, Toward an Astrophysical Theory of Chondrites, *Science*, **271**, Issue 5255, 1545–1552, 1996.

[69] Sonett, C. P. and Colburn, D. S., Electrical Heating of Meteorite Parent Bodies and Planets by Dynamo Induction from a Pre-main Sequence T Tauri "Solar Wind', *Nature*, **219**, Issue 5157, 924–926, 1968.

[70] The National Institute of Standards and Technology's web site (NIST), http://physics.nist.gov/PhysRefData/FFast/Text/cover.html

[71] Thomson, J.J., *Conduction of Electricity Through Gases*, Cambridge Univ. Press, London, 325 pp., 1906.

[72] Tholen and Barucci (1989).

[73] Tomida, H. et al., Radiation Damage on X-Ray CCDs and Restoration Technique for Space Astronomy PASJ **49**, 405 1997.

[74] Trombka, J. I., Squyres, S. W., Brckner, J., Boynton, W. V., Reedy, R. C., McCoy, T. J., Gorenstein, P., Evans, L. G., Arnold, J. R., Starr, R. D., Nittler, L. R., Murphy, M. E., Mikheeva, I., McNutt, R. L., McClanahan, T. P., McCartney, E., Goldsten, J. O., Gold, R. E., Floyd, S. R., Clark, P. E., Burbine, T. H., Bhangoo, J. S., Bailey, S. H., and Petaev, M., The Elemental Composition of Asteroid 433 Eros: Results of the NEAR-Shoemaker X-ray Spectrometer, *Science*, **289**, 2101–2105, 2000.

[75] Urey, H. C., Origin and Age of Meteorites, *Nature*, **175**, Issue 4451, 321–323, 1955.

[76] Yamamoto, Y., Development of embedded software for X-ray fluorescence spectrometer onboard MUSES-C (in Japanese), Doctor Thesis of the university of Tokyo, 2001.

[77] Yamashita, A., Dotani, T., Bautz, M., Crew, G., Ezuka, H., Gendreau, K., Kotani, T., Mitsuda, K., Otani, C., Rasmussen, A., Ricker, G., Tsunemi, H., Radiation damage to charge coupled devices in the space environment, **44**, Issue 3, Part 1, 847–853, 1997.

[78] Yamashita, A., Study of the origin of the cosmic X-ray background form ASCA deep sky observations, Doctor Thesis of The University of Tokyo, 1999.

[79] Yamashita A.; Dotani T.; Ezuka H.; Kawasaki M.; Takahashi K., Performance of the X-ray CCDs aboard the ASCA satellite after 5-year operation in space, Nuclear Instruments and Methods in Physics Research Section A: Accelerators, Spectrometers, Detectors and Associated Equipment, **436**, Number 1, 21 October 1999 , pp. 68-73(6)

[80] Yanai, K., and Kojima, H., Catalogue of the Antarctic Meteorites, National Institute of Polar Research, 230 pp. Tokyo, 1995.

[81] Yin L. I., Trombka, J. I., Adler, I., and Bielefeld, M., X-ray Remote Sensing Techniques for geochemical Analysis of Planetary Surfaces, REMOTE GEOCHEMICAL ANALYSIS: ELEMENTAL AND MINERALOGICAL COMPOSITION edited by Pieters C. M and Englert P. A., 1993.

[82] Weisberg, M. K.; McCoy, T. J.; Krot, A. N., Systematics and Evaluation of Meteorite Classification, Meteorites and the Early Solar System II, D. S. Lauretta and H. Y. McSween Jr. (eds.), University of Arizona Press, Tucson, 943, 19–52, 2006.

[83] Wilkison, Sarah L.; Robinson, Mark S.; Thomas, Peter C.; Veverka, Joseph; McCoy, Timothy J.; Murchie, Scott L.; Prockter, Louise M.; Yeomans, Donald K., An Estimate of Eros's Porosity and Implications for Internal Structure, *Icarus*, **155**, 94–103, 2002.

[84] http://astrogeology.usgs.gov/Projects/LunarConsortium/

[85] http://heasarc.gsfc.nasa.gov/docs/asca/gis_night_earth/gis_night_earth.html

[86] http://www.lpi.usra.edu/resources/clemen/clemen.html

[87] http://heasarc.gsfc.nasa.gov/docs/corp/tools.html

[88] http://naif.jpl.nasa.gov/naif/

[89] http://neo.jpl.nasa.gov/images/

[90] http://www.lpi.usra.edu/lunar/missions/apollo/apollo_15/experiments/